# Methods for higher order numerical simulations of complex inviscid fluids with immersed boundaries

# Erklärung

Hiermit versichere ich, die vorliegende Dissertation ohne Hilfe Dritter nur mit den angegebenen Quellen und Hilfsmitteln angefertigt zu haben. Alle Stellen, die aus Quellen entnommen wurden, sind als solche kenntlich gemacht. Diese Arbeit hat in gleicher oder ähnlicher Form noch keiner Prüfungsbehörde vorgelegen.

Darmstadt, den 27. Januar 2014

Björn Müller

# Abstract

Within this thesis, we study inviscid compressible flows of fluids modelled by several equations of state. Namely, these are the ideal gas law, the stiffened gas law, Tait's law and the covolume gas law. In their entirety, these equations of state can be used as models for the behaviour of many gases and liquids. After deriving new exact solutions for the corresponding variants of the Euler equations, we use the results as a tool for the verification of a higher-order accurate numerical scheme that has been implemented during the course of this thesis. The scheme is based on a Runge-Kutta Discontinuous Galerkin Method and the presented verification results show that we are able to obtain the expected rates of convergence in both, space and time.

In the main part of this thesis, we consider an important building block for the extension of this conventional discretization by means of a treatment for generic immersed boundaries, namely the numerical integration of general functions over domains that are at least partly defined by the zero iso-contour of a level set function defining the domain boundary. Here, we study two new, generally applicable approaches in terms of their robustness and convergence behaviour. The first approach is based on a classical adaptive strategy, while the second approach is based on a hierarchical moment-fitting strategy with variable Ansatz order $P$. Both methods have been designed such that they are applicable on general element types. Most notably, the results of our numerical experiments suggest that the moment-fitting procedure leads to integration errors that decrease with a rate of $O(h^{P+1})$, thus allowing for a severe increase of integration accuracy at constant computational effort.

# Zusammenfassung

Diese Arbeit beschäftigt sich mit reibungsfreien, kompressiblen Fluiden, welche mit Hilfe unterschiedlicher Zustandsgleichungen modelliert werden. Im einzelnen handelt es sich um das ideale Gasgesetz, das sogenannte stiffened Gasgesetz, das Taitsche Gesetz und das Kovolumen-Gasgesetz. Zusammen genommen eignen sich die genannten Zustandsgleichungen um das Verhalten einer Vielzahl von Gasen und Flüssigkeiten zu modellieren. Zunächst leiten wir neue exakte Lösungen für die zugehörigen Varianten der Euler-Gleichungen her. Im Anschluss verwenden wir die gewonnen Lösung zur Verifikation eines numerischen Verfahrens höherer Ordnung, welches im Rahmen dieser Arbeit implementiert wurde. Dieses Verfahren basiert auf der sogenannten Runge-Kutta Discontinuous Galerkin Methode. Wie wir anhand der präsentierten Verifikationsergebnisse aufzeigen, erreicht unsere Implementierung die für diese Methode zu erwartenden Konvergenzraten in Zeit und Raum.

Im Hauptteil der Arbeit befassen wir uns mit einem wesentlichen Baustein einer Erweiterung dieser konventionellen Diskretisierung um eine Möglichkeit zur Behandlung von eingebetteten Rändern. Bei dem Baustein handelt es sich um die numerische Integration allgemeiner Funktionen über Gebiete, welche zumindest teilweise auf Basis der Null-Niveaumenge einer Level-Set-Funktion definiert sind. In diesem Kontext untersuchen wir zwei neue, allgemein anwendbare Ansätze bezüglich ihrer Robustheit und ihrem Konvergenzverhalten. Das erste Verfahren basiert auf einer klassischen, adaptiven Strategie, während das zweite Verfahren auf einer hierarchischen Variante der sogenannten Moment-Fitting-Strategie mit variabler Ansatzordnung $P$ basiert. Beide Methoden wurden so konzipiert, dass sie auf allgemeinen Element-Typen anwendbar sind. Die Ergebnisse unserer numerischen Experimente deuten darauf hin, dass die Moment-Fitting-Strategie zu einem Integrationsfehler führt, der mit der Rate $O(h^{P+1})$ abnimmt. Dies führt dazu, dass bei gleichbleibendem Rechenaufwand ein sehr viel kleinerer Integrationsfehler erreicht werden kann.

# Acknowledgements

# Contents

# Contents

# List of Figures

# Nomenclature

$\mathcal{A}$      Sub-domain of a polygonal domain $\mathcal{K}$ associated with negative values of $\varphi$; cf. Equation (5.2)

$a$      Speed of sound

$a_0$      Speed of sound at stagnation conditions

$\mathcal{B}$      Sub-domain of a polygonal domain $\mathcal{K}$ associated with positive values of $\varphi$; cf. Equation (5.3)

$b$      Constant modelling the covolume of a gas; cf. Equation (2.31)

$D$      Number of spatial dimensions; $D \in \{1, 2, 3\}$

$\Delta t$      Size of a time-step

$\det(\cdot)$      Determinant of $\cdot$

$e$      Specific inner energy

$\gamma$      Heat capacity ratio

$\boldsymbol{H}(\cdot)$      Hessian matrix of $\cdot$

$h$      Characteristic mesh size

$\bar{h}$      Specific enthalpy

$\bar{h}_0$      Specific enthalpy at stagnation conditions

$\mathcal{I}$      Interface defined by the zero iso-contour of $\varphi$ inside of a polygonal domain $\mathcal{K}$; cf. Equation (5.1)

$J(\cdot)$      Jacobian matrix of $\cdot$

$\mathcal{K}$      A polygonal domain $\mathcal{K} \subset \mathbb{R}^D$

$L$      Reference length; cf. Section 2.3

$\boldsymbol{m}$      Momentum vector; $\boldsymbol{m} = (\rho u, \rho v)^{\mathsf{T}}$

M      Mach number

$\Omega$      Problem domain

$\Omega_h$      Discrete problem domain

$P$      Polynomial degree; $P \in \mathbb{N}_0$

$\mathcal{P}_{\mathcal{K}}(P)$      Space of polynomials of maximum degree $P$ on $\mathcal{K}$

$p$      Pressure

$p_0$      Pressure at stagnation conditions

$\varphi$          Level set function; $\varphi : \mathbb{R}^D \to \mathbb{R}$

$\pi$              Pressure offset of a stiffened gas; cf. Equation (2.21)

$\rho$             Density

$\rho_0$           Density at stagnation conditions

$\rho_\infty$      Reference density; cf. Section 2.3

$\rho E$           Total energy per volume

$s$                Specific entropy

$\mathrm{sgn}(\cdot)$   Sign of $\cdot$; $\mathrm{sgn} : \mathbb{R} \to \{-1, 0, 1\}$

$T$                Temperature

$t$                Time

$\boldsymbol{u}$   Velocity vector; $\boldsymbol{u} = (u, v)^\mathsf{T} \in \mathbb{R}^2$

$V_\infty$         Reference velocity; cf. Section 2.3

$\boldsymbol{x}$   Spatial coordinate vector in the problem domain; $\boldsymbol{x} = (x, y)^\mathsf{T} \in \Omega \subset \mathbb{R}^D$

$x$                One-dimensional spatial coordinate; $x \in \mathbb{R}$

# Abbreviations

| | |
|---|---|
| **BLAS** | Basic Linear Algebra Subprograms |
| **BoSSS** | Bounded Support Spectral Solver |
| **CFL** | Courant-Friedrichs-Levy |
| **DGM** | Discontinuous Galerkin Method |
| **DOF** | degrees of freedom |
| **EOC** | experimental order of convergence |
| **EOS** | equation of state |
| **FCM** | Finite Cell Method |
| **FDM** | Finite Difference Method |
| **FEM** | Finite Element Method |
| **FVM** | Finite Volume Method |
| **GFM** | Ghost Fluid Method |
| **HLLC** | Harten Lax van Leer Contact |
| **HMF** | hierarchical moment-fitting |
| **IBM** | Immersed Boundary Method |
| **LAPACK** | Linear Algebra Package |
| **ODE** | ordinary differential equation |
| **PDE** | partial differential equation |
| **RK** | Runge-Kutta |
| **RKDGM** | Runge-Kutta Discontinuous Galerkin Method |
| **SIMPLE** | Semi-Implicit Method for Pressure-Linked Equations |
| **XFEM** | eXtended Finite Element Method |

# 1 Introduction

Within this thesis, we present methods and tools for the numerical simulation of inviscid compressible flows. The study of such flows has a long tradition in computational aerodynamics, where many important results can be obtained without the consideration of frictional forces. In this context, the well-known ideal gas law provides a reasonably accurate description of relevant thermodynamic processes under a wide range of conditions (Anderson 2004).

However, the situation is more complex in many internal flows that, despite being well described by the inviscid equations of motion, require more sophisticated models for the correct prediction of the thermodynamic behaviour of the fluid. If a given flow comprises weakly compressible fluids such as water, for instance, using the ideal gas law leads to a strong overestimation of the density variations. The assumption of an incompressible flow with constant fluid density, on the other hand, is invalid for flows with locally high Mach numbers. A prominent example of this kind is the implosion of cavitation bubbles where water jets with extremely high velocities occur naturally (Franc & Michel 2010). But also if one is interested in the behaviour of gases only, there is a number of important technical applications where the ideal gas law loses its validity due to the presence of high pressures and temperatures. The thermodynamic behaviour of propellant gases in interior ballistics calculations, for example, requires the consideration of the size of the gas molecules in order to obtain accurate results (e.g., see Johnston (2005), Toro (2009) and Section 2.2) .

Apart from the issues related to the modelling of the thermodynamic properties of a fluid, the spatial discretization of the governing equations for practical problem configurations has been a major area of research for many years. Methods such as the Finite Difference Method (FDM), the Finite Volume Method (FVM), the Finite Element Method (FEM) and, lately, the Discontinuous Galerkin Method (DGM) enjoy great popularity in the context of general-purpose codes for numerical simulations on *boundary-fitted* domains (Wesseling (2000), Ferziger & Peric (2001), Feistauer, Felcman & Straškraba (2003)). That is, the computational grid is typically chosen such that its boundary (approximately) coincides with the boundary of the physical domain of interest. An IBM, on the other hand, *embeds* the domain of interest into a simple background grid, for example in order to simplify the process of grid generation or to facilitate the handling of moving domain boundaries (Mittal & Iaccarino 2005). Moreover, the ability to embed complex, moving boundaries into the discretization of the governing equations may be considered as a key building block for the accurate prediction of multi-phase flows comprising immiscible fluids that are separated by a sharp interface.

## 1.1    Goals and outline of this work

In this work, we aim at improving two important aspects of the numerical simulation of inviscid, compressible flows using a DGM. In unison, these aspects target the enhancement of numerical simulation of complex flows with immersed boundaries or interfaces.

The first aspect is the incorporation of advanced material models in the form of equations of state (EOS) that improve the modelling of real fluids. In Chapter 2, we thus review certain properties of the governing equations and, in particular, of extended material models. These properties are exploited in Chapter 3 in order to arrive at novel exact solutions for the Euler equations with these extended EOS. Finally, the exact solutions serve as a basis for the verification of our implementation of a DGM for the governing equations in Chapter 4.

The second aspect is given by the numerical integration of smooth functions with non-smooth enrichments at the zero iso-contour of a level set function (Osher & Fedkiw 2002). That is, we aim at being able to integrate smooth functions over complicated *sub*-domains of cells of the computational grid with high accuracy and efficiency. In this context, we present two new methods for the numerical approximation of the corresponding integrals in Chapter 5. Due to the significance of this subject for a broad class of numerical methods, the presented methods can be considered as the main contribution of this work.

In the end, we summarize the obtained results and give an outlook concerning links to future applications of the obtained results in Chapter 6. This includes an exemplary application of the presented quadrature techniques within the framework of a prototypic implementation of an IBM that will serve as a starting point for future research efforts in this direction.

## 1.2    Numerical simulations and the BoSSS framework

All numerical results presented in the following have been obtained by means of a solver for compressible, inviscid flows that has been developed by the author (Müller 2011). The implementation is based on the Bounded Support Spectral Solver (BoSSS) software framework (Kummer, Emamy, Mousavi Belfeh Teymouri & Oberlack 2009), which offers a generic tool set for the implementation of numerical methods based on the DGM. An excerpt of the structure of BoSSS is visualized in Figure 1.1. A main advantage of the modular structure is the ability to reuse a great part of the existing source code, especially since the focus of the verification of a new solver can be limited to problem specific issues. The BoSSS framework has successfully been applied, for instance, to the solution of the incompressible Navier-Stokes equations by means of a projection scheme (Kummer (2011), Kummer & Oberlack (2013)) and a generalization of the well-known Semi-Implicit Method for Pressure-Linked Equations (SIMPLE) scheme (Klein, Kummer & Oberlack 2013).
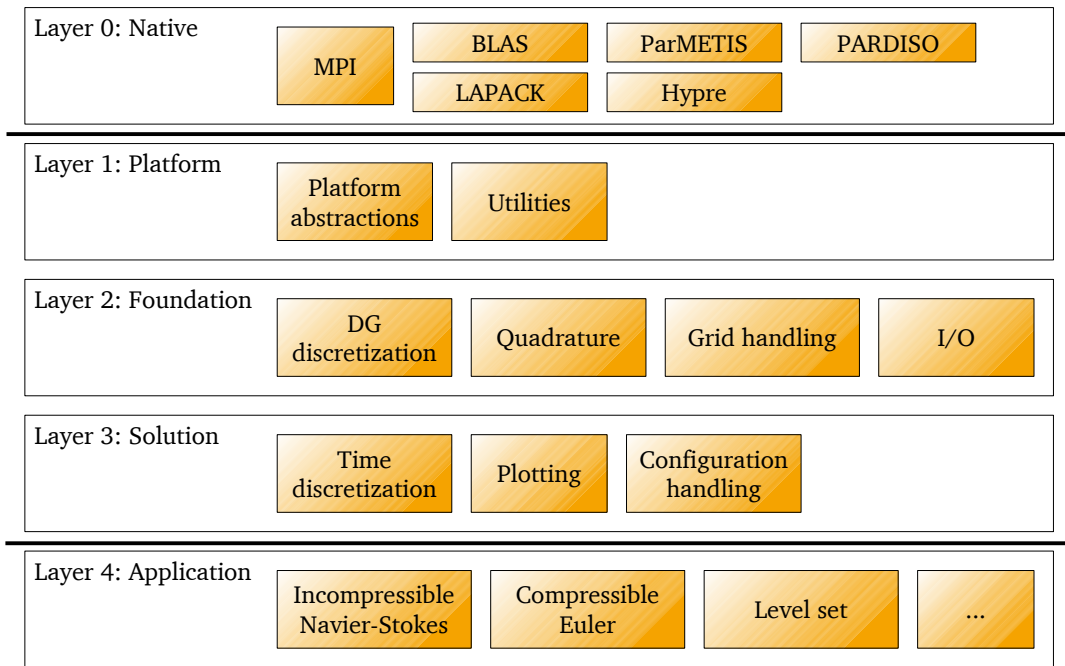
Figure 1.1: Structure of the BoSSS framework

This work is mainly concerned with two of the modules depicted in Figure 1.1: The quadrature and the solver for the compressible Euler equations. The considerations in the following chapters will thus concentrate on aspects that are directly influenced by these packages, and we refer the interested reader to the publications by Kummer et al. (2009) and Kummer (2011) for more detailed information about topics excluded from this work. Furthermore, we emphasize that some technical details concerning the implementation of the presented numerical scheme have already been described by Müller (2011), which is why we limit ourselves to the discussion of the underlying discretization scheme in Chapter 4.

# 2 Governing equations

Subsequently, we will introduce the partial differential equations (PDEs) that form the basis for the analytical and numerical results that will be discussed later in this thesis. After introducing the Euler equations for inviscid compressible flow in the first part of this chapter, we will discuss some possibilities for the choice of the material law that is required for the closure of the system. Such an EOS can have a strong influence on the behaviour of the flow, and we will discuss further implications in the subsequent chapters.

## 2.1   The Euler equations for inviscid compressible flow

The two-dimensional Euler equations for compressible inviscid flow (e.g., see Prandtl (2008)) are given by conservation laws for mass, momentum and energy in differential form. In conservative form, they read

$$\frac{\partial \boldsymbol{U}}{\partial t} + \frac{\partial \boldsymbol{F}_x(\boldsymbol{U})}{\partial x} + \frac{\partial \boldsymbol{F}_y(\boldsymbol{U})}{\partial y} = 0, \tag{2.1}$$

where the vector of *conserved quantities* $\boldsymbol{U} \in \mathbb{R}^4$ and the *convective fluxes* $\boldsymbol{F}_x : \mathbb{R}^4 \to \mathbb{R}^4$ and $\boldsymbol{F}_y : \mathbb{R}^4 \to \mathbb{R}^4$ are given by

$$\boldsymbol{U} = \begin{pmatrix} \rho \\ \rho u \\ \rho v \\ \rho E \end{pmatrix}, \quad \boldsymbol{F}_x(\boldsymbol{U}) = \begin{pmatrix} \rho u \\ \rho u^2 + p \\ \rho u v \\ u(\rho E + p) \end{pmatrix}, \quad \boldsymbol{F}_y(\boldsymbol{U}) = \begin{pmatrix} \rho v \\ \rho v u \\ \rho v^2 + p \\ v(\rho E + p) \end{pmatrix}, \tag{2.2}$$

respectively, where $t$ is the time, $\boldsymbol{x} = (x, y)^\mathsf{T}$ is the spatial coordinate vector, $\rho \in \mathbb{R}^+$ is the fluid density, $\boldsymbol{m} = (\rho u, \rho v)^\mathsf{T} \in \mathbb{R}^2$ is the momentum vector, $\boldsymbol{u} = (u, v)^\mathsf{T} \in \mathbb{R}^2$ is the velocity vector, $\rho E \in \mathbb{R}^+$ is the total energy per volume and $p \in \mathbb{R}^+$ is the pressure. The total energy itself is the aggregation of the inner energy $\rho e \in \mathbb{R}^+$ and the kinetic energy due to the dynamic motion of the fluid, i.e.

$$\rho E = \rho e + \frac{1}{2} \rho \boldsymbol{u} \cdot \boldsymbol{u}. \tag{2.3}$$

In the presented form, the Euler equations are not closed since we have not yet introduced a material law for the pressure $p$. That is, we need an EOS in the form $p = p(\rho, e)$ for which we will discuss some relevant choices in the following section.

## 2.2   Equations of state

We now study some EOS that will be of interest for the types of flows we will study later on. In this analysis, we limit ourselves to *incomplete* EOS of the form $p = p(\rho, e)$ that are *simple* in the sense that all its material parameters are constant (Callen (1985), Menikoff & Plohr (1989)). As a result, we can assume that

$$e = c_v T \tag{2.4}$$

and

$$\bar{h} = c_p T \tag{2.5}$$

hold, where $T$ denotes the local temperature,

$$\bar{h} = e + \frac{p}{\rho} \tag{2.6}$$

denotes the specific enthalpy, and $c_v$ and $c_p$ denote the specific heat capacities at constant volume and pressure, respectively. In this setting, we can define the heat capacity ratio

$$\gamma = \frac{c_p}{c_v} = \frac{\bar{h}}{e}, \tag{2.7}$$

which plays an important role in the description of *isentropic* processes where the *specific entropy* $s = s(\rho, e)$ stays constant along the path of each individual fluid element.

Even though fully isentropic processes are rarely observed in the real world, it is well-known that the assumptions leading to the Euler equations imply isentropy as long as all flows quantities are differentiable (Wesseling 2000, Chapter 10). That is, the entropy of a fluid element is only increased if it crosses a shock. The concept of *homentropic* flows, on the other hand, additionally requires that the entropy is constant throughout the complete domain of interest. While this assumption is even more severe than the assumption of an isentropic flow, it tremendously simplifies the analysis and thus provides the setting for almost all analytical results for the Euler equations and its EOS.

A *complete* EOS is given by a relation $e = e(\rho, s)$ that can be recast into the form $p = p(\rho, s)$ (Menikoff & Plohr 1989). For homentropic flows, this form directly implies the existence of a *barotropic* relationship $p = p(\rho)$, therefore illustrating the fact that the energy equation in (2.1) decouples from the mass and momentum equations in such configurations. While a complete EOS uniquely defines the corresponding incomplete EOS, the opposite is generally not true. Since EOS are still often given in an incomplete form, the fundamental thermodynamic relation (Callen (1985), Poling, Prausnitz & O'Connell (2001)),

$$T\,ds = \ de + p\,d\rho^{-1}, \tag{2.8}$$

is most often used for the derivation of entropy-related equations. We note that it is traditional and convenient to use Leibniz' notation for expressions involving differential quantities for the purpose of exemplifying manipulations that are required

in order to arrive at implications of Equation (2.8). Even though this practice is not mathematically rigorous, it is well suited for illustrative purposes, and the final results can easily be verified by means of elementary calculus.

A thermodynamically valid EOS $p = p(\rho, e)$ can always be cast into the form $e = e(\rho, p)$ (Menikoff & Plohr 1989). Using the corresponding total differential

$$de = \frac{\partial e}{\partial p}\, dp + \frac{\partial e}{\partial \rho}\, d\rho \qquad (2.9)$$

and Equation (2.4), it follows that an infinitesimal change of entropy is given by

$$ds = \frac{c_v}{e} \left( \frac{\partial e}{\partial p}\, dp + \left( \frac{\partial e}{\partial \rho} - \frac{p}{\rho^2} \right) d\rho \right). \qquad (2.10)$$

The postulation $ds = 0$ for an isentropic process finally leads to

$$0 = \frac{1}{e}\frac{\partial e}{\partial p}\, dp + \frac{1}{e} \left( \frac{\partial e}{\partial \rho} - \frac{p}{\rho^2} \right) d\rho, \qquad (2.11)$$

which will serve as an important tool for the discussion of the models stated below.

## 2.2.1   Ideal gas law

The ideal gas law reads
$$p = (\gamma - 1)\rho e \qquad (2.12)$$

and is a common model for simple gases at moderate pressures and temperatures. Its simplicity renders it especially useful for analytical considerations, while its practical applicability is limited. A typical choice for the material parameter is given by $\gamma = 1.4$ for the modelling of standard air.

We now strive to determine the speed of sound and the isentropic relations for an ideal gas. Doing so, we will discuss the required steps in a little more detail in order to facilitate the tangibility in case of the more complicated EOS presented in the subsequent sections.

The speed of sound $a$ of a given fluid is defined in terms of the change of pressure during an infinitesimal, isentropic density oscillation (Anderson 2011). It can hence be expressed as the derivative of pressure with respect to density *at constant entropy*, which is typically written as

$$a = \sqrt{\left. \frac{\partial p}{\partial \rho} \right|_s}. \qquad (2.13)$$

We emphasize that this notation may be considered misleading since it only represents a proper partial derivative in the context of a complete EOS $p = p(\rho, s)$. Nonetheless, we stick with this notation since it has become the quasi-standard in the relevant literature (Callen (1985), Menikoff & Plohr (1989), Poling et al. (2001), Toro (2009),

Anderson (2011)). An expression for this derivative in the context of an incomplete EOS can be obtained by solving Equation (2.11) for $dp/d\rho$.

Rewriting Equation (2.12) in terms of the inner energy gives

$$e = \frac{p}{(\gamma - 1)\rho},\tag{2.14}$$

hence

$$\frac{\partial e}{\partial p} = \frac{1}{(\gamma - 1)\rho} \quad \text{and} \quad \frac{\partial e}{\partial \rho} = -\frac{p}{(\gamma - 1)\rho^2}.\tag{2.15}$$

After inserting this into (2.11), we have

$$0 = \frac{1}{p}\,dp - \underbrace{\frac{1}{e}\left(\frac{p}{(\gamma - 1)\rho^2} + \frac{p}{\rho^2}\right)}_{=\gamma/\rho}\,d\rho,\tag{2.16}$$

from which it directly follows that

$$a^2 = \gamma\frac{p}{\rho}\tag{2.17}$$

for an ideal gas.

Moreover, Equation (2.16) also serves as a starting point for the derivation of the variation of the quantities of interest during an isentropic change of state. Integration yields

$$0 = \int \frac{1}{p}\,dp - \int \frac{\gamma}{\rho}\,d\rho\tag{2.18}$$

$$\Rightarrow \quad 0 = \ln(p) - \gamma\ln(\rho) + \text{const.},\tag{2.19}$$

and it finally follows that

$$\frac{p}{\rho^\gamma} = \text{const.}\tag{2.20}$$

for this type of flows.

## 2.2.2 Stiffened gas law

Stiffened gas models have been used by a number of authors (Cocchi & Saurel (1997), Saurel & Abgrall (1999), Wang, Liu & Khoo (2006), Farhat, Rallu & Shankaran (2008)) for the study of weakly compressible fluids such as water. The most common form of the equation reads

$$p = (\gamma - 1)\rho e - \gamma\pi,\tag{2.21}$$

where $\pi$ is a model constant that determines the *stiffness* of the fluid. Basically, the model describes an ideal gas that has been pre-loaded with the pressure $\gamma\pi$. As a result,

the main appeal of the model is due to its simplicity and its versatility. A typical choice for the material parameters of water is $\gamma = 7$ and $\pi = 6 \times 10^8 \, \mathrm{Pa}$ (Farhat et al. 2008).

Restating (2.21) in terms of the inner energy yields

$$e = \frac{p + \gamma\pi}{(\gamma - 1)\rho}, \tag{2.22}$$

viz.

$$\frac{\partial e}{\partial p} = \frac{1}{(\gamma - 1)\rho} \quad \text{and} \quad \frac{\partial e}{\partial \rho} = -\frac{p + \gamma\pi}{(\gamma - 1)\rho^2}. \tag{2.23}$$

Using Equation (2.11) once again leads to

$$0 = \frac{1}{p + \gamma\pi} \, dp - \frac{1}{e} \underbrace{\left( \frac{p + \gamma\pi}{(\gamma - 1)\rho^2} + \frac{p}{\rho^2} \right)}_{= \frac{\gamma}{\rho} \frac{p+\pi}{p+\gamma\pi}} \, d\rho \tag{2.24}$$

and further

$$0 = \frac{1}{p + \pi} \, dp - \frac{\gamma}{\rho} \, d\rho. \tag{2.25}$$

It follows that the speed of sound of a stiffened gas is given by

$$a^2 = \gamma \frac{p + \pi}{\rho}, \tag{2.26}$$

while we have

$$\frac{p + \pi}{\rho^\gamma} = \text{const.} \tag{2.27}$$

for the isentropic relation.

### 2.2.3 Tait's law

The Tait equation is often considered as an alternative to the stiffened gas equation presented in the previous section (Flores & Holt (1981), Chen & Cooke (1994), Fedkiw, Aslam, Merriman & Osher (1999), Qiu, Liu & Khoo (2007)). It is often presented in the form

$$p = \left( p_{\text{ref}} + \frac{k}{\gamma} \right) \left( \frac{\rho}{\rho_{\text{ref}}} \right)^\gamma - \frac{k}{\gamma}, \tag{2.28}$$

where $k$ is a model constant that has been determined from measurements that were taken from a fluid with reference density $\rho_{\text{ref}}$ at the reference pressure $p_{\text{ref}}$. Following the work by Farhat et al. (2008), we rearrange this equation in order to arrive at

$$p = \alpha\rho^\gamma - \pi, \tag{2.29}$$

where $\pi = k/\gamma$ and $\alpha = (p_{\text{ref}} + \pi)/\rho_{\text{ref}}^{\gamma}$. In the light of the above-stated analysis regarding the stiffened gas equation, this form immediately reveals the fact that the Tait model implies

$$\frac{p + \pi}{\rho^{\gamma}} = \alpha = \text{const.,} \tag{2.30}$$

and can thus be seen as the special case of a *homentropic* stiffened gas model. As we are only concerned with homentropic flows in the following, we do not repeat the corresponding analysis and disregard the Tait equation in the remainder of this work.

It should be noted, however, that some authors have argued that the Tait model performs better than the stiffened gas model in certain situations (e.g., see Ivings, Causon & Toro (1998) and the references therein). This ambiguity also manifests itself in the fact that the material parameters for the Tait law are typically chosen differently than in the case of a stiffened gas law (Farhat et al. 2008). These differences are however beyond the scope of this work and will not be discussed any further.

## 2.2.4   Covolume gas law

The incomplete EOS for a covolume (or Noble–Abel) gas,

$$p = (\gamma - 1)\frac{\rho}{1 - b\rho}e, \tag{2.31}$$

introduces a correction to the ideal gas EOS by enforcing a maximal density $1/b$ that models the effect of the volume of individual gas molecules at high pressures (e.g., see Johnston (2005) and Toro (2009)). It can be obtained from the well-known van der Waal's equation,

$$p = (\gamma - 1)\frac{\rho}{1 - b\rho}e - \bar{a}\rho^2, \tag{2.32}$$

by setting the model constant $\bar{a}$ to zero. In other words, we neglect the attraction between individual gas molecules that is modelled by the last term in Equation (2.32). A major reason for this simplification is the fact that the van der Waal's EOS entails a contradiction to the assumption of a *simple* EOS through a violation of Equation (2.4) (Callen 1985).

Solving (2.31) for the inner energy results in

$$e = \frac{(1 - b\rho)p}{(\gamma - 1)\rho} = \frac{p}{(\gamma - 1)\rho} - \frac{bp}{\gamma - 1}, \tag{2.33}$$

from which we obtain the partial derivatives

$$\frac{\partial e}{\partial p} = \frac{1}{(\gamma - 1)\rho} - \frac{b}{\gamma - 1} = \frac{1 - b\rho}{(\gamma - 1)\rho} \quad \text{and} \quad \frac{\partial e}{\partial \rho} = -\frac{p}{(\gamma - 1)\rho^2}. \tag{2.34}$$

After insertion into (2.11), we have

$$0 = \frac{1}{p}\,dp - \underbrace{\frac{1}{e}\left(\frac{p}{(\gamma-1)\rho^2} + \frac{p}{\rho^2}\right)}_{=\frac{\gamma}{(1-b\rho)\rho}}\,d\rho. \tag{2.35}$$

It directly follows that the speed of sound of a covolume gas can be computed from

$$a^2 = \gamma\frac{p}{(1-b\rho)\rho}. \tag{2.36}$$

Furthermore, Equation (2.35) can be integrated by expanding the second term into partial fractions. The final form of the isentropic relation is given by

$$\frac{p}{\rho^\gamma}(1-b\rho)^\gamma = \text{const.}, \tag{2.37}$$

which, as expected, simplifies to Equation (2.20) if we set $b$ to zero.

## 2.3 Units of measure

We can obtain a non-dimensional form of the Euler equations by introducing a reference length $L$, a reference density $\rho_\infty$ and a reference velocity $V_\infty$. This allows for the introduction of the non-dimensional independent variables

$$\boldsymbol{x}' = \frac{\boldsymbol{x}}{L} \quad \text{and} \quad t' = \frac{V_\infty t}{L}, \tag{2.38}$$

the non-dimensional dependent variables

$$\rho' = \frac{\rho}{\rho_\infty}, \quad \boldsymbol{m}' = \frac{\boldsymbol{m}}{\rho_\infty V_\infty}, \quad \rho E' = \frac{\rho E}{\rho_\infty V_\infty^2}, \quad p' = \frac{p}{\rho_\infty V_\infty^2} \quad \text{and} \quad e' = \frac{e}{V_\infty^2}, \tag{2.39}$$

and, where applicable, the additional non-dimensional constants

$$\pi' = \frac{\pi}{\rho_\infty V_\infty^2} \quad \text{and} \quad b' = \rho_\infty b, \tag{2.40}$$

which we can insert into Equation (2.1) and the chosen EOS. It is easy to verify that this change of variables leaves the Euler equations *completely unchanged* (e.g., see Feistauer et al. (2003)). As a result, we can set $L = 1\,\text{m}$, $\rho_\infty = 1\,\text{kg/m}^3$ and $V_\infty = 1\,\text{m/s}$ without loss of generality. Hereafter, we will refer to the non-dimensional quantities only, while omitting the prime in the definition for simplicity.

# 3 Analytical results for the Euler equations

In this chapter, we will discuss some extensions of well-known analytical solutions for the Euler equations originally based on the assumption of an ideal gas. In particular, we will consider the EOS presented in Section 2.2: The stiffened gas EOS and the covolume gas EOS. To the best of our knowledge, the presented extensions have not been discussed in literature. We are in fact not aware of any non-trivial but smooth analytical solution for the compressible Euler equations with another EOS than the ideal gas law. Consequently, we will make use of some of the following results as a tool for the verification of our numerical scheme in Chapter 4.

During the analysis of the proposed solutions, we will often make use of *stagnation* (or *total*) quantities, which are defined as the virtual value of a specific quantity after a fluid element has been brought to rest *isentropically* (Anderson 2011, Chapter 7). For a given quantity, we will indicate the corresponding stagnation quantity by a lower subscript $0$ (e.g., $\rho_0$ in case of the stagnation density). It should be noted that the flows we will be considering in this chapter are assumed to be homentropic, which is why the stagnation quantities associated are *constant* by definition.

## 3.1 An extension of the isentropic vortex solution

An isentropic vortex is a simple solution for the generic Euler equations that has first been proposed by Lamb (1916) and has later been popularized as a test case for numerical schemes by Davoudzadeh, McDonald & Thompson (1995) and others. Here, we focus on the form used by Hu & Shu (1998), which is laid out in a little more detail by Hu (2006). Hu (2006) starts with the observation that the two-dimensional Euler equations in an infinite domain admit generic solutions of the type

$$\begin{pmatrix} \rho \\ u \\ v \\ p \end{pmatrix} = \begin{pmatrix} 0 \\ u' \\ v' \\ 0 \end{pmatrix} + \begin{pmatrix} \rho_r \\ -u_r \sin(\theta) \\ u_r \cos(\theta) \\ p_r \end{pmatrix} \tag{3.1}$$

where the functions $\rho_r = \rho_r(r)$, $u_r = u_r(r)$ and $p_r = p_r(r)$ satisfy

$$\frac{dp_r}{dr} = \rho_r \frac{u_r^2}{r} \tag{3.2}$$

and $r$ and $\theta$ are the polar coordinates centred around $(u't, v't)$, i.e.

$$x = r\cos(\theta) + u't \tag{3.3}$$
$$y = r\sin(\theta) + v't. \tag{3.4}$$

In this setting, $\boldsymbol{u}' = (u', v')^\mathsf{T}$ is a constant background velocity that advects the self-contained vortex through a domain of interest.

In a next step, a smooth velocity profile $u_r$ has to be presumed. A common choice is

$$u_r = r\exp\left(\frac{1 - r^2}{2}\right), \tag{3.5}$$

where we have set all free scaling parameters to unity for the sake of brevity. The classical solution may be obtained by assuming a homentropic ideal gas, where Equation (2.20) allows for the stipulation $p_r = \rho_r^\gamma$. After inserting this into Equation (3.2) and integrating, we have

$$\rho_r = \left(c_1 - \frac{\gamma - 1}{2\gamma}\exp(1 - r^2)\right)^{\frac{1}{\gamma - 1}} \tag{3.6}$$

and

$$p_r = \left(c_1 - \frac{\gamma - 1}{2\gamma}\exp(1 - r^2)\right)^{\frac{\gamma}{\gamma - 1}} \tag{3.7}$$

with a constant $c_1$ that can be found by some auxiliary condition. By enforcing a pressure of one in the free-stream, for example, one has $p(r \to \infty) = 1$, viz. $c_1 = 1$.

### 3.1.1 Variation of the equation of state

In the following, we will make use of the isentropic relations derived in Section 2.2 in order to arrive at variations of Equation (3.6) and Equation (3.7). In Section 3.1.2, we will show how the respective results can be combined for the purpose of creating a reference solution for multi-phase flow calculations.

#### 3.1.1.1 Stiffened gas

Since the extension of the above-stated results for a stiffened gas is straightforward, we only state the most important results required in Section 3.1.2. The isentropic relation for a stiffened gas (Equation (2.27)) at homentropic conditions admits the setting $p = \rho^\gamma - \pi$, which is why the solution of the ordinary differential equation (ODE) (3.2) does not change. It directly follows that the relations

$$\rho_r = \left(c_1 - \frac{\gamma - 1}{2\gamma}\exp(1 - r^2)\right)^{\frac{1}{\gamma - 1}} \tag{3.8}$$

and

$$p_r = \left( c_1 - \frac{\gamma - 1}{2\gamma} \exp(1 - r^2) \right)^{\frac{\gamma}{\gamma - 1}} - \pi. \tag{3.9}$$

form a valid solution of the Euler equations.

### 3.1.1.2 Covolume gas

In the light of the isentropic relation (2.37), we now set

$$p_r = \left( \frac{\rho_r}{1 - b\rho_r} \right)^{\gamma} \tag{3.10}$$

and insert this expression into Equation (3.2). After integration, we arrive at

$$\frac{\gamma - b\rho_r}{(\gamma - 1)\rho_r} \left( \frac{\rho_r}{1 - b\rho_r} \right)^{\gamma} = c_1 - \exp(1 - r^2), \tag{3.11}$$

which is an *implicit* solution that cannot be solved for $\rho_r$ explicitly. For given values of $r$, $\gamma$, $b$ and the constant of integration, however, the equation can easily be solved numerically. The pressure may finally be obtained via Equation (3.10).

In Figure 3.1 and Figure 3.2, an exemplary solution for two gases with $\gamma = 1.4$ and $p_r(r \to \infty) = 1$ has been visualized. The covolume in the modified solution has been set to $b = 0.1$, a value which is around two orders of magnitude higher than empirical values for real gases (Toro 2009). Yet, this exaggerated choice simplifies the visualization of the differences between a covolume gas and an ideal gas, which most notably manifest themselves in the smaller variations in the density profile depicted in Figure 3.1.

### 3.1.2 Extension to a multi-phase vortex

Within this section, we assume an inviscid flow comprising two immiscible fluids with distinct EOS that are separated by a circular interface with fixed radius $R \in \mathbb{R}^+$. That is, we introduce the generally time-dependent domains $\mathcal{A} = \{(r, \theta) \in \mathbb{R}^2 : r < R\}$, $\mathcal{B} = \{(r, \theta) \in \mathbb{R}^2 : r > R\}$ and $\mathcal{I} = \{(r, \theta) \in \mathbb{R}^2 : r = R\}$ and assign dissimilar fluids to the domains $\mathcal{A}$ and $\mathcal{B}$. The resulting configuration with the interface normal vector $\boldsymbol{n}_\mathcal{I} = (\cos(\theta), \sin(\theta))^\mathsf{T}$ is displayed in Figure 3.3.

While the flow in the sub-domains $\mathcal{A}$ and $\mathcal{B}$ is governed by the standard Euler equations, we have to satisfy jump conditions at the interface $\mathcal{I}$ between the fluids (e.g., see Wang & Oberlack (2011)). In the absence of excess surface quantities, these conditions simplify to

$$[\![\boldsymbol{u}]\!] \cdot \boldsymbol{n}_\mathcal{I} = 0 \tag{3.12}$$

and

$$[\![p]\!] = \mathrm{We}^{-1}, \tag{3.13}$$
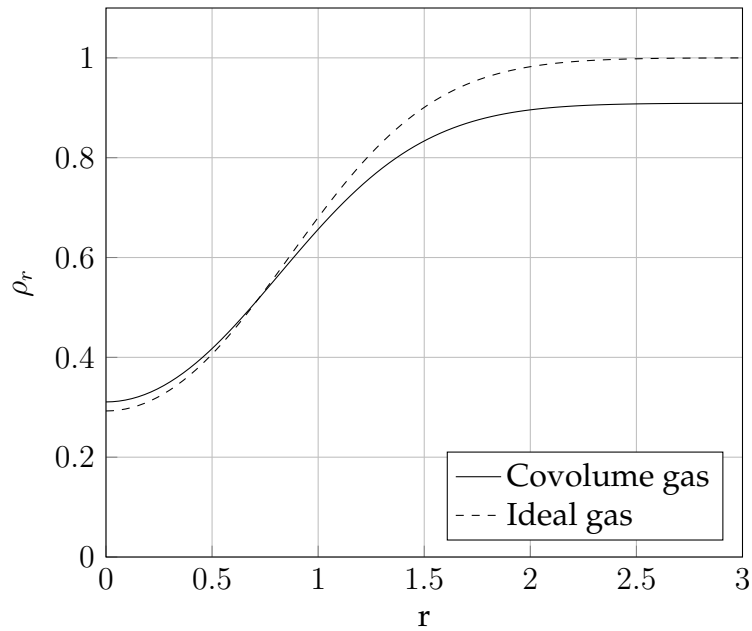
Figure 3.1: Comparison of the density profiles of the isentropic vortex solution for an ideal gas ($\gamma = 1.4$) and a covolume gas ($\gamma = 1.4$, $b = 0.1$)
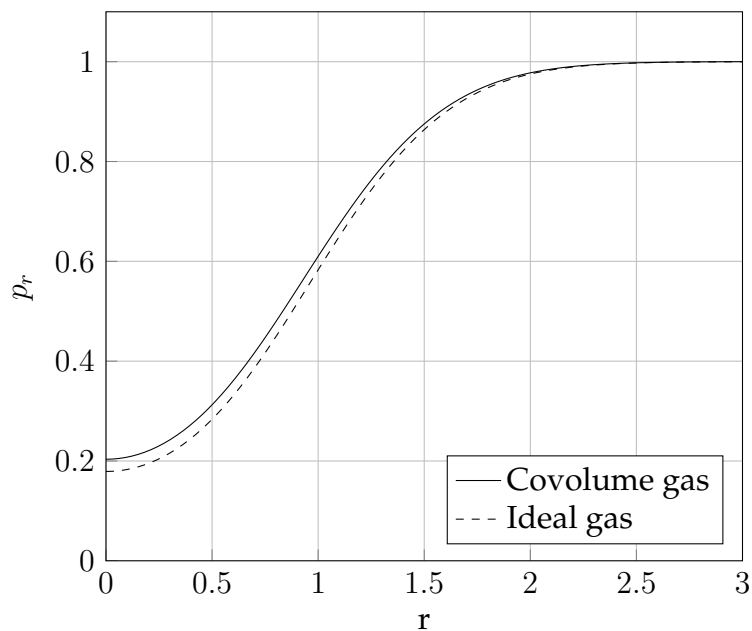


Figure 3.2: Comparison of the pressure profiles of the isentropic vortex solution for an ideal gas ($\gamma = 1.4$) and a covolume gas ($\gamma = 1.4$, $b = 0.1$)
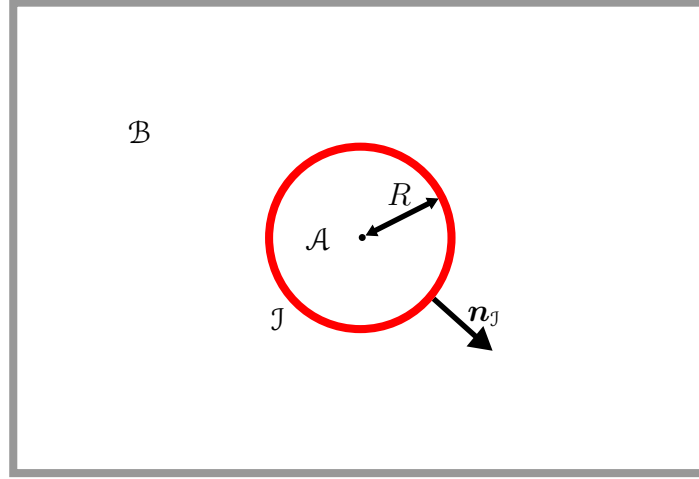
Figure 3.3: Schematic representation of the multi-phase vortex set-up. Note that the sub-domain $\mathcal{A}$ extends to infinity in horizontal and vertical direction

where

$$\text{We} = \frac{\rho_\infty V_\infty^2 L}{\sigma} \tag{3.14}$$

is the Weber number and $\sigma$ is the surface tension ($[\sigma] = \text{N/m}$) that is assumed to be constant. Here and in the following, the jump operator $[\![\cdot]\!]$ at an interface with the normal vector $\boldsymbol{n}$ is defined as the difference between the one-sided limits of a generic quantity $q$ from the left and the right, viz.

$$[\![q]\!] = \lim_{\varepsilon \to 0} \left( q(\boldsymbol{x} - \varepsilon\boldsymbol{n}) - q(\boldsymbol{x} + \varepsilon\boldsymbol{n}) \right) \tag{3.15}$$

for $\varepsilon \in \mathbb{R}_0^+$.

Note that we have included the surface tension in Equation (3.13), even though we consider gas-gas interfaces in some configurations. The practical relevance of this setting can obviously be disputed. Nonetheless, it is appealing to be able to define a transient test case with an analytical solution for $\text{We} < \infty$, in particular for the verification of numerical schemes for multi-phase flow calculations.

It is easy to see that the velocity profile defined in Equation (3.1) is always tangential to $\mathcal{J}$ and thus automatically satisfies the first jump condition. A valid solution for the above-stated multi-phase problem can hence be obtained by choosing the free constants in the respective solutions for the pressure $p_r$ such that condition (3.13) is fulfilled. The exact solution is then given in the form

$$\rho_r(r) = \begin{cases} \rho_r^{\mathcal{A}}(r) & \text{if } r < R \\ \rho_r^{\mathcal{B}}(r) & \text{if } r > R \end{cases} \tag{3.16}$$

and

$$p_r(r) = \begin{cases} p_r^{\mathcal{A}}(r) & \text{if } r < R \\ p_r^{\mathcal{B}}(r) & \text{if } r > R \end{cases}, \tag{3.17}$$

where $\left(\rho_r^{\mathcal{A}}(r), p_r^{\mathcal{A}}(r)\right)$ and $\left(\rho_r^{\mathcal{B}}(r), p_r^{\mathcal{B}}(r)\right)$ are isentropic vortex solutions in the respective sub-domains with constants $c_1^{\mathcal{A}}$ and $c_1^{\mathcal{B}}$, respectively, that ensure that $p_r^{\mathcal{A}}(R) = p_r^{\mathcal{B}}(R) + \mathrm{We}^{-1}$ is satisfied.

For the sake of simplicity, we will hereafter assume that $R = L = 1\,\mathrm{m}$ and that the constitutive equation for the fluid in $\mathcal{A}$ is the ideal gas law. As a result, $\rho_r^{\mathcal{A}}(r)$ and $p_r^{\mathcal{A}}(r)$ are given by Equation (3.6) and Equation (3.7), respectively. This setting permits the use of any of the above-mentioned EOS in $\mathcal{B}$ and the prescription of the pressure in the free-stream according to $p(r \to \infty) = 1$ by choosing the constant $c_1^{\mathcal{B}}$ accordingly. Finally, we arrive at a valid solution in the full domain by solving

$$p_r^{\mathcal{B}}(R) + \mathrm{We}^{-1} \overset{!}{=} p_r^{\mathcal{A}}(R) = \left( c_1^{\mathcal{A}} - \frac{\gamma - 1}{2\gamma} \exp(1 - R^2) \right)^{\frac{\gamma}{\gamma-1}} \tag{3.18}$$

for $c_1^{\mathcal{A}}$.

In the following, we discuss some exemplary results for cases where the sub-domain $\mathcal{B}$ is governed by either a stiffened gas or a covolume gas. We emphasize that the applied material parameters have been chosen for illustrative purposes only, i.e. they are largely non-physical (cf. Section 2.2).

A first example without surface tension is displayed in Figure 3.4 and Figure 3.5. Here, an ideal gas with the material properties of air has been combined with a stiffened gas with the same heat capacity ratio and a small pressure offset of $\pi = 9$. Due to the absence of surface tension, the pressure (Figure 3.5) is continuous, even though the density jump in Figure 3.6 is significant.

In the second example, on the other hand, we have set $\mathrm{We} = 10$ which leads to a pressure jump of $\Delta p_r = 0.1$ (see Figure 3.7). Another difference in comparison to the first is case the setting $\gamma = 7$ in the stiffened phase. As it has been mentioned in Section 3.2.1, this value is often used for the modelling of water. Here and in the following, we abstain from using a realistic value for $\pi$ in order to keep the tests presented in Chapter 4 comparable for all applied EOS. While the pressure profile Figure 3.7 is only mildly affected by this change, Figure 3.6 clearly shows that the density variations are strongly reduced in compared to the first example.

In the final example, we replace the stiffened gas by a covolume gas with $\gamma = 1.4$ and $b = 0.1$ (see Figure 3.8 and Figure 3.9). The differences in the pressure distribution in comparison to the respective single-phase case (cf. Figure 3.1 and Figure 3.2) are, as it can be expected, relatively small. This finding does however not hold for the density distribution (see Figure 3.8) which exhibits a clearly visible jump.

## 3.2   An extension of the Ringleb solution

The Ringleb solution (Ringleb 1940) is a smooth analytic solution of the Euler equations for a potentially transonic flow around a two-dimensional, streamlined obstacle. Very few smooth analytical solutions for the compressible Euler equations with non-trivial
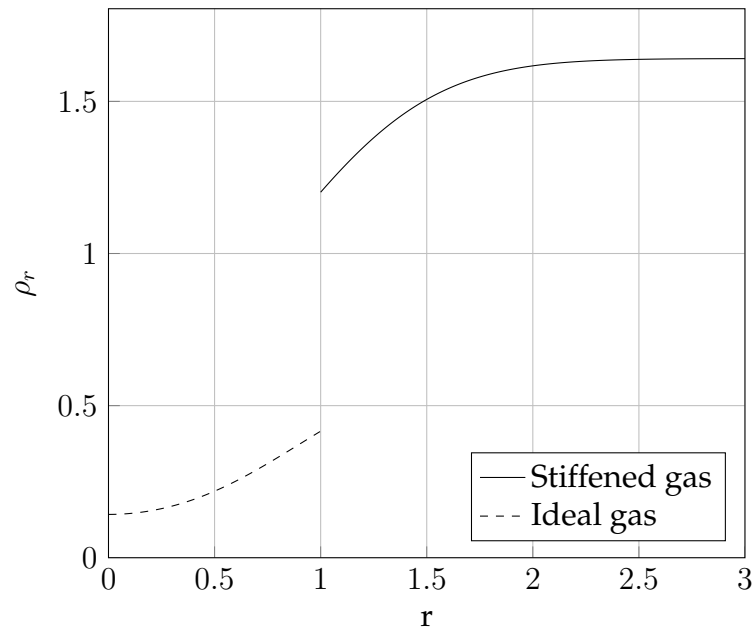
Figure 3.4: Density profile of the multi-phase vortex solution for an ideal gas ($\gamma = 1.4$) surrounded by a stiffened gas ($\gamma = 1.4$, $\pi = 9$) in the absence of surface tension (We $\rightarrow \infty$)
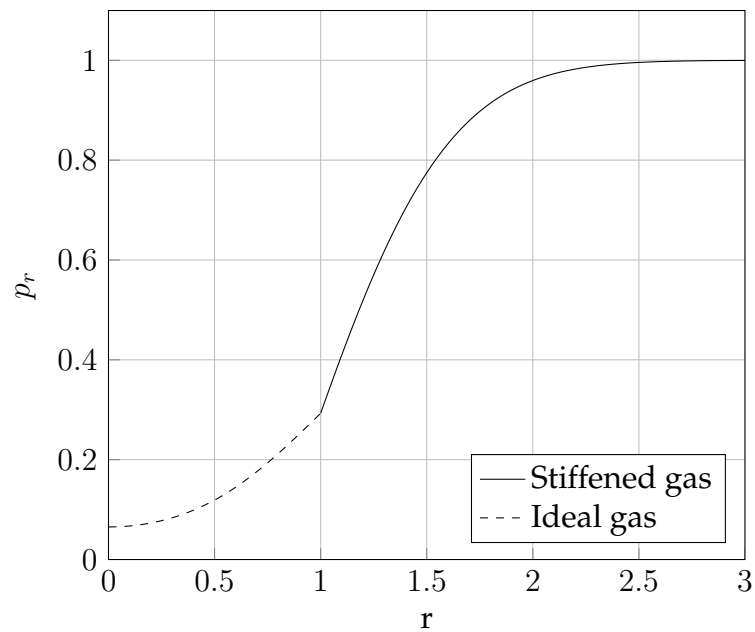


Figure 3.5: Pressure profile of the multi-phase vortex solution for an ideal gas ($\gamma = 1.4$) surrounded by a stiffened gas ($\gamma = 1.4$, $\pi = 9$) in the absence of surface tension (We $\rightarrow \infty$)
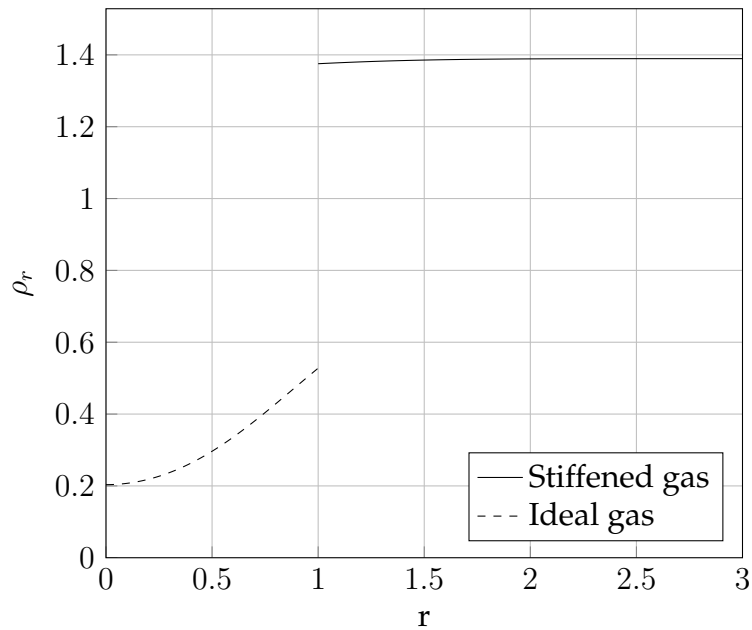
Figure 3.6: Density profile of the multi-phase vortex solution for an ideal gas ($\gamma = 1.4$) surrounded by a stiffened gas ($\pi = 9$) with the heat capacity ratio of water ($\gamma = 7$) in the presence of surface tension (We $= 10$)
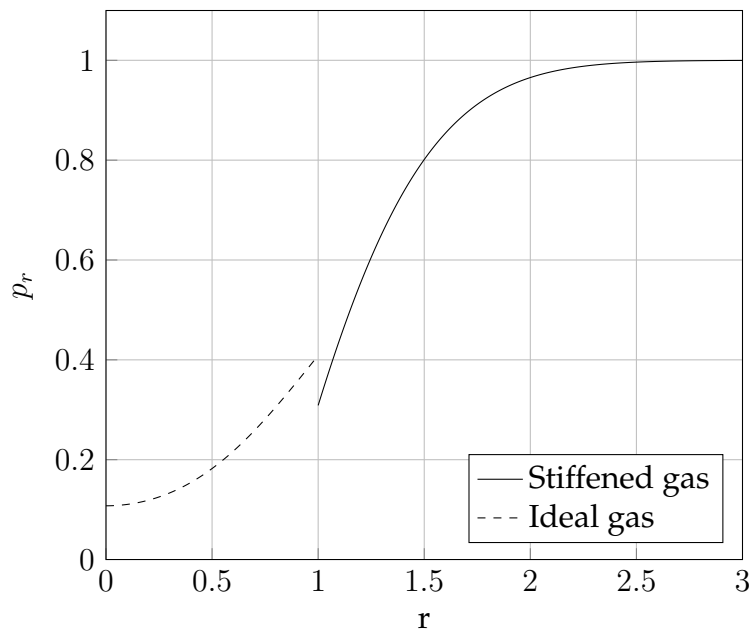


Figure 3.7: Pressure profile of the multi-phase vortex solution for an ideal gas ($\gamma = 1.4$) surrounded by a stiffened gas ($\pi = 9$) with the heat capacity ratio of water ($\gamma = 7$) in the presence of surface tension (We $= 10$)
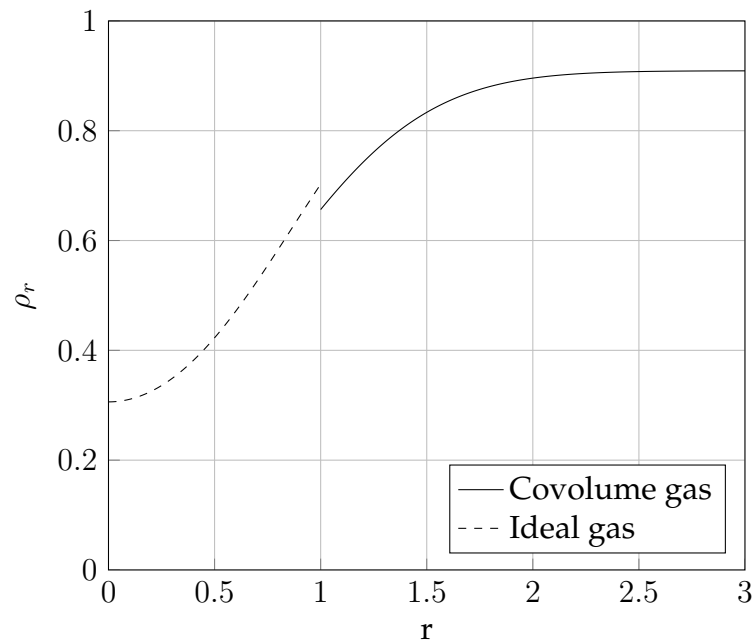
Figure 3.8: Density profile of the multi-phase vortex solution for an ideal gas ($\gamma = 1.4$) surrounded by a covolume gas ($\gamma = 1.4$, $b = 0.1$) in the absence of surface tension (We $\to \infty$)
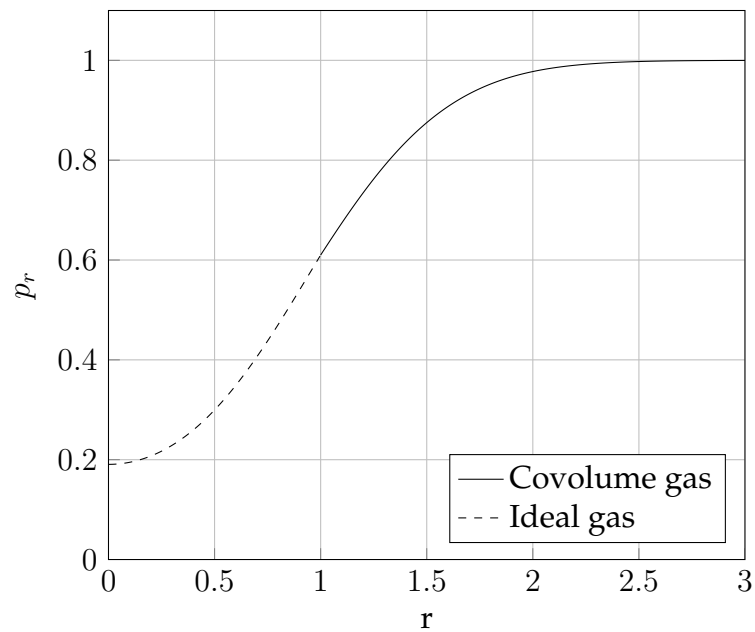


Figure 3.9: Pressure profile of the multi-phase vortex solution for an ideal gas ($\gamma = 1.4$) surrounded by a covolume gas ($\gamma = 1.4$, $b = 0.1$) in the absence of surface tension (We $\to \infty$)

boundary conditions exist, which is why several authors have proposed it as a test case for their numerical schemes (Chiocchia (1985), Halt & Agarwal (1992), Bassi & Rebay (1997), Hartmann (2002), Dolejší, Feistauer & Schwab (2003)). The solution is based on the *hodograph* transformation which has been studied in detail by Chang (1952) and Geiringer (1955). Hereafter, we will however heavily rely on the textbook by Emanuel (2010), who probably gives the most comprehensive review of the subject matter. Since the full derivation of the below-stated results is quite extensive, we will not restate them in their entirety but refer the interested reader to the said resource.

The main idea of the hodograph transformation is the exchange of dependent and independent variables for the purpose of arriving at a simpler form of the differential equations. This obviously implies that the problem domain is given as part of the solution to the resulting equations. Indeed, we will later see that the main challenge lies in the transformation of solutions from the so-called hodograph plane into the physical plane. For a steady, homentropic and irrotational flow, the hodograph equations corresponding to Equation (2.1) read

$$\left(\mathrm{M}(V)^2 - 1\right)\frac{\partial^2 \Psi}{\partial \theta^2} = \left(\mathrm{M}(V)^2 + 1\right)V\frac{\partial \Psi}{\partial V} + V^2\frac{\partial^2 \Psi}{\partial V^2}, \tag{3.19}$$

where $\mathrm{M}(V)$ is the Mach number and $\Psi$ is a stream-function that satisfies the continuity equation, i.e.

$$u = \frac{\rho_0}{\rho}\frac{\partial \Psi}{\partial y} \quad \text{and} \quad v = \frac{\rho_0}{\rho}\frac{\partial \Psi}{\partial x} \tag{3.20}$$

with the is the stagnation density $\rho_0$. Furthermore, $V\mathbb{R}_0^+$ and $\theta \in [0, 2\pi]$ are the hodograph coordinates that represent the velocity magnitude and the flow angle, respectively, viz.

$$u = V\cos(\theta) \quad \text{and} \quad v = V\sin(\theta). \tag{3.21}$$

The hodograph transformation is consequently given by a bijective mapping between $(x, y)$ and $(V, \theta)$.

Equation (3.19) is considerably simpler than the full set of Euler equations, but it is still necessary to make further assumptions in order to facilitate the analysis. In his original study, Ringleb (1940) makes use of the energy equation

$$\bar{h} + \frac{V^2}{2} = \bar{h}_0, \tag{3.22}$$

which has simplified significantly in the light of the above-mentioned assumptions (e.g., see Anderson (2011, p. 533ff)). Here, $\bar{h}_0$ denotes the constant stagnation enthalpy of the flow. By virtue of the relation for the speed of sound of an ideal gas (Equation (2.17)) and the definition of the specific enthalpy (Equation (2.6)), the energy equation can be written as

$$\frac{a^2}{\gamma - 1} + \frac{V^2}{2} = \frac{a_0^2}{\gamma - 1} \tag{3.23}$$

and further

$$a^2 = a_0^2 - \frac{\gamma - 1}{2} V^2. \tag{3.24}$$

In turn, this implies

$$\mathrm{M}^2 = \frac{V^2}{a_0^2 - \frac{\gamma-1}{2} V^2}, \tag{3.25}$$

which reveals that the Mach number is given as a function of the velocity magnitude only. Inserting this into Equation (3.19) finally shows that the Ringleb solution

$$\Psi = \frac{\cos(\theta)}{\sqrt{\frac{\gamma-1}{2} \frac{V}{a_0}}} = \frac{\cos(\theta)}{\sqrt{\tau}}, \tag{3.26}$$

with

$$\tau = \frac{\gamma - 1}{2} \frac{V^2}{a_0^2} \tag{3.27}$$

indeed satisfies the hodograph equations.

Emanuel (2010) proceeds by discussing the solution and the uniqueness of the mapping between $(x, y)$ and $(V, \theta)$ for an ideal gas, where it is possible to derive

$$\rho = \left( \rho_0^{\gamma-1} - \frac{\gamma - 1}{2\gamma c_2} V^2 \right)^{\frac{1}{\gamma-1}} \tag{3.28}$$

and

$$p = \left( p_0^{\frac{\gamma-1}{\gamma}} - \frac{\gamma - 1}{2\gamma c_2} V^2 \right)^{\frac{\gamma}{\gamma-1}} \tag{3.29}$$

from Equation (2.20) in combination with the energy equation. Here, $c_2 \in \mathbb{R}^+$ is a free constant that has traditionally been chosen such that the stagnation speed of sound $a_0$ equals one. This allows for the derivation of an implicit representation of the exact solution, which Emanuel (2010) casts in the form

$$x^2 + (y - g(\tau))^2 = \frac{\gamma - 1}{8} \frac{1}{\tau^2 (1 - \tau)^{\frac{2}{\gamma-1}}}, \tag{3.30}$$

where

$$g(\tau) = -\frac{1}{\sqrt{8(\gamma - 1)}} \int \frac{1}{\tau(1 - \tau)^{\frac{\gamma}{\gamma-1}}} \, d\tau. \tag{3.31}$$

The solution in a given point $(x_0, y_0)$ can hence be obtained by solving (3.30) for $\tau$ numerically. Then, $V$ follows from Equation (3.27) and either

$$x(\tau) = -\frac{1}{2} \sqrt{\frac{\gamma - 1}{2}} \sin(2\theta) \frac{1}{\tau(1 - \tau)^{\frac{1}{\gamma-1}}} \tag{3.32}$$

or

$$y(\tau) = -\frac{1}{2} \sqrt{\frac{\gamma - 1}{2}} \cos(2\theta) \frac{1 - \frac{\gamma}{\gamma-1}\tau}{\tau^2 (1 - \tau)^{\frac{\gamma}{\gamma-1}}} + g(\tau) \tag{3.33}$$

can be used to obtain $\theta$. Finally, all other relevant flow quantities can be evaluated by means of Equation (3.21), Equation (3.24), Equation (3.28) and Equation (3.29).

## 3.2.1 Variation of the equation of state

In the derivation of the Ringleb solution, a key ingredient was the assumption of an ideal gas which enables the application of the simplified energy equation

$$a^2 = a_0^2 - \frac{\gamma - 1}{2}V^2. \qquad \text{(3.24, repeated)}$$

While it is generally infeasible to generate such an expression for a covolume gas (cf. Section 3.1.1), it is interesting to note that the stiffened gas law (2.21) *does* imply such a relation. This can easily be shown by means of the energy equation in combination with the corresponding relation for the speed of sound (Equation (2.26)) and the definition of the specific enthalpy (Equation (2.6)). Combining these equations gives

$$\bar{h} = e + \frac{p}{\rho} \qquad \text{(3.34)}$$

$$= \frac{p + \gamma\pi + (\gamma - 1)p}{(\gamma - 1)\rho} \qquad \text{(3.35)}$$

$$= \frac{\gamma}{\gamma - 1}\frac{p + \pi}{\rho} \qquad \text{(3.36)}$$

$$= \frac{a^2}{\gamma - 1}, \qquad \text{(3.37)}$$

which means that Equation (3.24) is also valid for the stiffened gas EOS (and thus Tait's EOS). A closer inspection reveals that this result also holds for the backward transformation, and we finally obtain a *generalized* exact solution

$$\rho = \left( \rho_0^{\gamma - 1} - \frac{\gamma - 1}{2\gamma c_2}V^2 \right)^{\frac{1}{\gamma - 1}} \qquad \text{(3.38)}$$

for the density and

$$p = \left( p_0^{\frac{\gamma - 1}{\gamma}} - \frac{\gamma - 1}{2\gamma c_2}V^2 \right)^{\frac{\gamma}{\gamma - 1}} - \pi \qquad \text{(3.39)}$$

for the pressure. It is interesting to note that we see from Equation (3.27) that, as long as we maintain the same value for $a_0$, the pressure offset $\pi$ does not influence the solution $(V, \theta)$ and thus the shape of the problem domain.

### 3.2.2 A note on the numerical evaluation of the solution

It depends on the actual value of $\gamma$ whether $g(\tau)$ can be expressed in terms of elementary functions or not. Emanuel (2010), for example, proposes

$$g(\tau) = -\frac{1}{\sqrt{2(\gamma-1)}} \left( \tanh^{-1}\left(\sqrt{1-\tau}\right) - \frac{1}{5(1-\tau)^{\frac{5}{2}}} - \frac{1}{2(1-\tau)^{\frac{3}{2}}} - \frac{1}{(1-\tau)^{\frac{1}{2}}} \right) \quad (3.40)$$

if $\gamma = 1.4$. A similar form has already been used in the original publication by Ringleb (1940), but we do not know of any *simple* generalization for arbitrary values of $\gamma$. While the integral can be expressed in terms of the hypergeometric function $_2F_1$ (Olver, Lozier, Boisvert & Clark 2010, Chapter 8.17) via

$$g(\tau) = -\frac{\sqrt{\gamma-1}}{2\sqrt{2\gamma}} \text{Re}\left[ \left(1 - \frac{1}{\tau}\right)^{c_\gamma} (1-\tau)^{-c_\gamma} {}_2F_1\left(c_\gamma, c_\gamma, 1+c_\gamma, \frac{1}{\tau}\right) \right], \quad (3.41)$$

where $c_\gamma = \gamma/(\gamma-1)$ and $\text{Re}: \mathbb{C} \to \mathbb{R}$ denotes the real part of a complex value, the evaluation of $_2F_1$ at the required points is problematic. This is due to the fact that the definition of $_2F_1$ is based on the *hypergeometric series* which is not defined for $\tau \in [0,1]$. Consequently, it is often more sensible to perform the integration for particular values of $\gamma$. For the case of $\gamma = 7$, for instance, $g(\tau)$ can be evaluated from

$$\begin{aligned}
g(\tau) = \frac{1}{24} \Bigg[ &6\tan^{-1}\left(\frac{2c_\tau - 1}{\sqrt{3}}\right) + 6\tan^{-1}\left(\frac{2c_\tau + 1}{\sqrt{3}}\right) \\
&+ \sqrt{3}\left(\frac{12}{c_\tau} + 2\ln\left(\frac{c_\tau - 1}{c_\tau + 1}\right) + \ln\left(\frac{1 - c_\tau + c_\tau^2}{1 + c_\tau + c_\tau^2}\right)\right) \Bigg],
\end{aligned} \quad (3.42)$$

where we have used the abbreviation

$$c_\tau = (1-\tau)^{1/6}. \quad (3.43)$$

### 3.2.3 Brief discussion of exemplary configurations

So far, we have only discussed how the exact solution for the Ringleb flow can be evaluated in a particular point $(x_0, y_0)$ in the infinite plane, given that the corresponding coordinate in the hodograph plane, $(V_0, \theta_0)$, is uniquely defined. It is hence customary to define the actual problem domain as a duct with adiabatic slip walls by choosing a velocity $V_{\min}$ and two streamlines $\Psi = \Psi_{\min}$ and $\Psi = \Psi_{\max}$ in order to define a bounded sub-domain of $\mathbb{R}_0^- \times \mathbb{R}$ such that it is guaranteed that the above-mentioned uniqueness condition is fulfilled. The domain boundary may then be constructed by choosing a streamline $\Psi_0$ and evaluating the exact solution for discrete velocities $V_0 \in [V_{\min}, V_{\max}(\Psi_0)]$, where

$$V_{\max}(\Psi_0) = \max_\theta \left( \frac{\cos(\theta)}{\Psi_0} \sqrt{\frac{2a_0^2}{\gamma-1}} \right) = \frac{1}{\Psi_0} \sqrt{\frac{2a_0^2}{\gamma-1}} \quad (3.44)$$

follows from Equation (3.26).

Subsequently, we will contrast an exemplary solution for an ideal gas with the proper-
ties of standard air ($\gamma = 1.4$) to an artificial stiffened gas that can be interpreted as water
with an increased compressibility ($\gamma = 7$, $\pi = 10$). All further parameters have been
chosen such that the flow is completely subsonic and such that the resulting domains
roughly resemble in shape (though, not in size). The complete set of parameters as
well as a visualization of the flow fields for an ideal gas and a stiffened gas is shown in
Figure 3.10 and Figure 3.11, respectively. The lower compressibility of the stiffened
fluid manifests itself in the smaller variation in the width of the duct, despite the
higher values of the velocity magnitude in Figure 3.11. The higher velocities are also
the cause for the stronger pressure variations in the second case, while all general flow
characteristics are qualitatively similar to the original Ringleb solution.

(a) Velocity vectors

(b) Pressure distribution with Mach iso-lines denoted by thick black lines
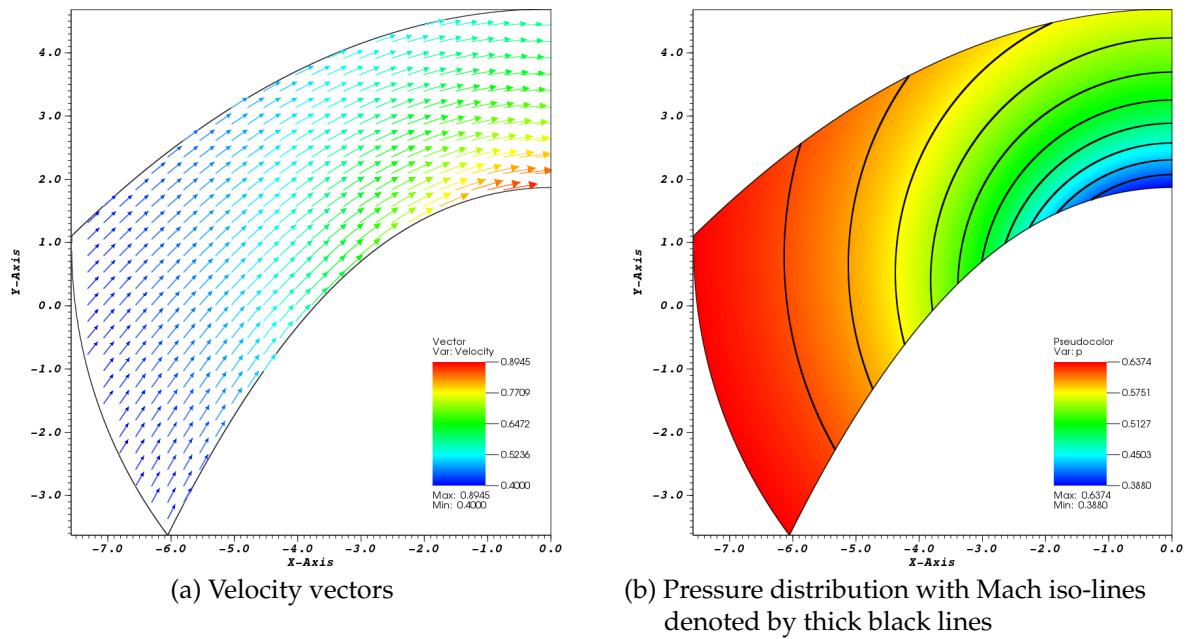
Figure 3.10: Exact solution for the Ringleb flow of an ideal gas where $\gamma = 1.4$, $\rho_0 = 1$, $a_0 = 1$, $\Psi_{\min} = 2.5$, $\Psi_{\max} = 4$ and $V_{\min} = 0.4$



(a) Velocity vectors

(b) Pressure distribution with Mach iso-lines denoted by thick black lines
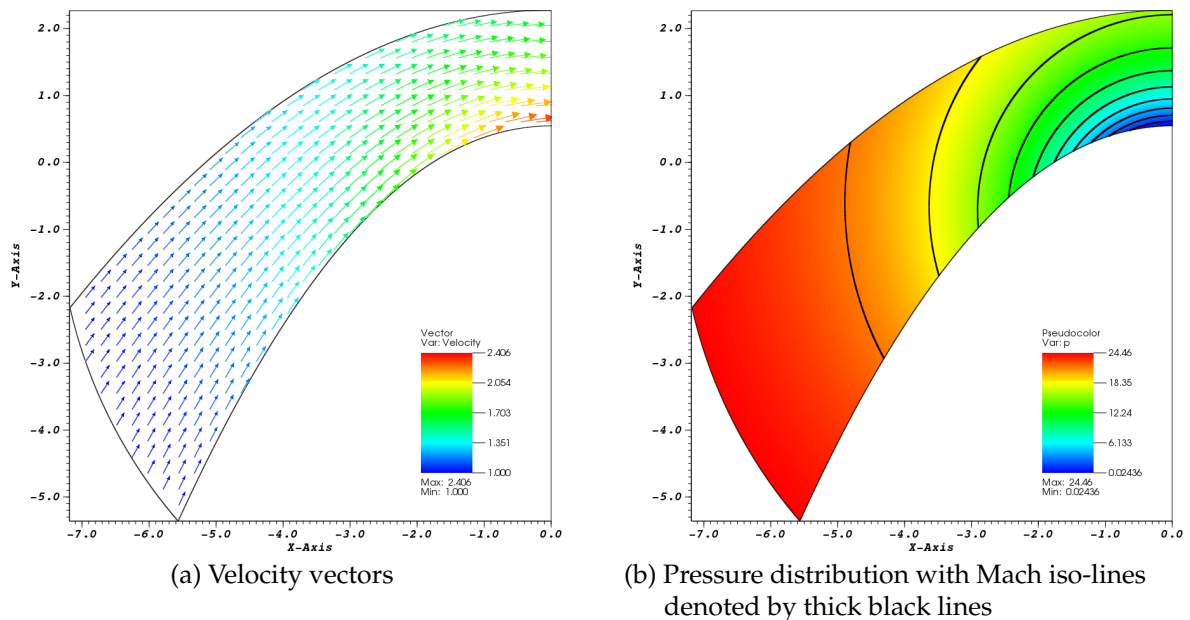
Figure 3.11: Exact solution for the Ringleb flow of a stiffened gas where $\gamma = 7$, $\pi = 10$, $\rho_0 = 11.2$, $a_0 = 5$, $\Psi_{\min} = 1.2$, $\Psi_{\max} = 1.8$ and $V_{\min} = 1$

# 4 Numerical simulations using a Discontinuous Galerkin Method

During the course of this chapter, we will study the numerical simulation of test cases with the analytical solutions presented in Chapter 3 using a RKDGM on quadrilateral and triangular grids. We will thus briefly summarize the state of the art (Section 4.1) as well as the applied discretization strategy (Section 4.2), before we assess the spatial and the temporal convergence of the implemented scheme for different EOS using the example of the isentropic vortex flow (cf. Section 3.1) and the Ringleb flow (cf. Section 3.2) in Section 4.3.

## 4.1 State of the art

The DGM is a comparatively young approach to the discretization of PDEs. Its development starting from first numerical experiments by Reed & Hill (1973) and the corresponding analysis by LeSaint & Raviart (1974) has been retraced in detail by Cockburn, Karniadakis & Shu (2000b). Consequently, we focus on the relevant developments in the context of hyperbolic conservation laws, where the introduction of the higher-order RKDGM by Cockburn & Shu (1989) was a major breakthrough.

Several extensions of this work (Cockburn, Lin & Shu (1989), Cockburn, Hou & Shu (1990), Cockburn & Shu (1991), Cockburn & Shu (1998b)) have received great attention and strongly pushed the general awareness of the DGM. In the sequel, many authors have considered the application of the RKDGM (Cockburn et al. (1989), Cockburn & Shu (1998a)) and related methods (Halt & Agarwal (1992), Atkins & Shu (1996)) to the Euler equations. Due to the fact that modern formulations of a DGM can be interpreted as the natural unification of a basic FEM and a basic FVM, many concepts originally developed in context of these discretization techniques have been extended to the DGM. Examples include numerical fluxes based on Riemann solvers (Feistauer et al. (2003), Qiu, Khoo & Shu (2006)), limiting procedures (Persson & Peraire (2006), Qiu et al. (2007)), space-time formulations (van der Vegt & van der Ven (1998), van der Vegt & van der Ven (2002), Lörcher, Gassner & Munz (2007)) and local time-stepping algorithms (Lörcher et al. (2007), Dumbser, Balsara, Toro & Munz (2008), Lörcher, Gassner & Munz (2008), Hindenlang, Gassner, Altmann, Beck, Staudenmaier & Munz (2012)).

As already indicated by the above examples, a major appeal of the DGM is due to its versatility, including the local choice of the approximation order $P$ and the grid topology. In this context, Johnson & Pitkäranta (1986) have proven that the spatial error for the discretization of a scalar transport equation based on the DGM converges at

least with a rate of $O(h^{P+0.5})$ if the solution is sufficiently smooth. Peterson (1991) has later shown that this is an optimal estimate because it is indeed possible to construct grids where the convergence rate is limited by $O(h^{P+0.5})$. Still, an overwhelming number of numerical studies have shown that a convergence rate of $O(h^{P+1})$ can be observed in practical computations, even in the case of non-linear systems of hyperbolic conservation laws where hardly an analytical result exists (Cockburn, Karniadakis & Shu 2000a). We will thus use the term *optimal* order of convergence when referring to an experimental order of convergence (EOC) of $O(h^{P+1})$.

On the other hand, the computational efficiency of the DGM has been the subject of many discussions in the past. The extensive topic of performance analysis is far beyond the scope of this thesis and shall not be further addressed here. In fact, the main design goals in the implementation of the numerical scheme presented in the following section where flexibility and usability, which is why we do not present any performance characteristics in this chapter. We still wish to emphasize that the excellent parallelizability of the DGM renders it competitive with traditional approaches like the FVM and the FEM, even in the context of challenging industrial applications (e.g., see Wang, Fidkowski, Abgrall, Bassi, Caraeni, Cary, Deconinck, Hartmann, Hillewaert, Huynh, Kroll, May, Persson, van Leer & Visbal (2013) and the references therein).

## 4.2 Generic Discontinuous Galerkin discretization

We will introduce the basic form of the DGM using the example of the scalar conservation law

$$\frac{\partial c}{\partial t} + \nabla \cdot \boldsymbol{f}(c) = 0 \tag{4.1}$$

for a concentration $c = c(\boldsymbol{x}, t)$ with $\boldsymbol{x} \in \Omega \subset \mathbb{R}^D$, $t \in \mathbb{R}_0^+$ and a smooth function $\boldsymbol{f} : \mathbb{R} \to \mathbb{R}^D$, supplemented with suitable initial and boundary conditions. For more detailed information about the topic, we refer the interested reader to the well-known textbooks by Li (2006), Hesthaven & Warburton (2007) and Di Pietro & Ern (2012), as well as the excellent overview by Cockburn (2003).

Let $\Omega_h$ be a discretization of $\Omega$ with a characteristic mesh parameter $h$ that represents a measure for the size of the cells $\{\mathcal{K}_i\}_{i=1,\dots,N}$ forming a *tesselation* of $\Omega_h$. Here, each $\mathcal{K}_i$ is a $D$-dimensional, non-degenerate polytope with outward unit normal vector $\boldsymbol{n}$. Within this setting, consider a set of cell-local test functions $\{\Phi_{i,j}\}_{j=1,\dots,M}$ with $\Phi_{i,j} = \Phi_{i,j}(\boldsymbol{x}) : \mathbb{R}^D \to \mathbb{R}$ that we can use to build the *discrete weak formulation* of (4.1) in cell $\mathcal{K}_i$. To this end, we multiply Equation (4.1) by $\Phi_{i,j}$, integrate over the cell $\mathcal{K}_i$ and perform an integration by parts in order to obtain

$$\int_{\mathcal{K}_i} \frac{\partial c}{\partial t} \Phi_{i,j} \, dV + \int_{\partial \mathcal{K}_i} \left( \boldsymbol{f}(c) \cdot \boldsymbol{n} \right) \Phi_{i,j} \, dA - \int_{\mathcal{K}_i} \boldsymbol{f}(c) \cdot \nabla \Phi_{i,j} \, dV = 0. \tag{4.2}$$

For the purposes of this work, it suffices to assume that the set $\{\Phi_{i,j}\}$ forms a basis of the space of polynomials $\mathcal{P}_{\mathcal{K}_i}(P)$ of maximum degree $P$. Examples include a monomial

basis, an orthonormalized monomial basis and tensor-products of univariate polynomials such as Legendre polynomials (Hesthaven & Warburton 2007). We note that the implementation used in the numerical examples presented in this thesis is based on the second option for the sake of generality (e.g., see Gassner, Lörcher, Munz & Hesthaven (2008) and the references therein).

The surface $\partial \mathcal{K}_i$ is composed of a set of edges $\{\mathcal{E}_{i,e}\}_{e=1,\ldots,E_i}$. We call $\mathcal{E}_{i,e}$ an *internal edge*, if there exists a cell $\mathcal{K}_n \neq \mathcal{K}_i$ $(n = 1, \ldots, N)$ such that $\mathcal{E}_{i,e} = \overline{\mathcal{K}}_i \cap \overline{\mathcal{K}}_n$. In such a situation, $\mathcal{K}_n$ is a *neigbhour* of $\mathcal{K}_i$ and we introduce the notation

$$n(i,e) = \begin{cases} n & \text{if } \mathcal{E}_{i,e} = \mathcal{K}_i \cap \mathcal{K}_n \\ 0 & \text{otherwise} \end{cases} \tag{4.3}$$

in order to be able to identify the $e$-th neighbour of $\mathcal{K}_i$. If $n(i,e) = 0$, $\mathcal{E}_{i,e}$ is a *boundary edge* (i.e., $\mathcal{E}_{i,e} \in \partial \Omega_h$) for which we have to specify boundary conditions. We note that we will briefly discuss this issue in the presentation of the numerical examples in Section 4.3. Using these definitions, Equation (4.2) can be rewritten as

$$\int\limits_{\mathcal{K}_i} \frac{\partial c}{\partial t} \Phi_{i,j} \, dV + \sum_{e=1}^{E_i} \int\limits_{\mathcal{E}_{i,e}} (\boldsymbol{f}(c) \cdot \boldsymbol{n}) \, \Phi_{i,j} \, dA - \int\limits_{\mathcal{K}_i} \boldsymbol{f}(c) \cdot \nabla \Phi_{i,j} \, dV = 0, \tag{4.4}$$

where the edge integrals account for the coupling between adjacent cells.

We still have to introduce an approximation for the unknown concentration $c$ in order to be able to assemble a fully discrete system of equations from (4.4). For the purposes of this work, we choose the modal approximation

$$c(\boldsymbol{x}, t)|_{\mathcal{K}_i} \approx \tilde{c}(\boldsymbol{x}, t)|_{\mathcal{K}_i} = c_i(\boldsymbol{x}, t) = \sum_{k=0}^{M} c_{i,k}(t) \, \Phi_{i,k}(\boldsymbol{x}) \tag{4.5}$$

in accordance with the Galerkin approach which implies that Ansatz and test functions are identical. The vectors of coefficients $\boldsymbol{c}_i = \boldsymbol{c}_i(t) = (c_{i,1}(t), \ldots, c_{i,M}(t))^{\mathsf{T}}$ hence completely define the local approximate solutions $c_i(\boldsymbol{x}, t)$, which in sum define the global solution $\tilde{c} = \tilde{c}(\boldsymbol{x}, t)$. In the following, we will omit the arguments $\boldsymbol{x}$ and $t$ wherever this causes no ambiguity.

However, inserting this approximation into Equation (4.4) directly is problematic. This can be seen from the fact that we do not enforce any continuity restrictions on $\mathcal{E}_{i,e}$, i.e. in general

$$c_i|_{\mathcal{E}_{i,e}} =: c^- \neq c^+ := c_{n(i,e)}\big|_{\mathcal{E}_{i,e}}, \tag{4.6}$$

which is why the integrand of the edge integrals in Equation (4.4) would be undefined. This also holds for boundary edges where $c^+$ follows from the implementation of the boundary conditions of the problem of interest. As a result, we introduce a monotone,

Lipschitz continuous *numerical flux function* $f = f(c^-, c^+, \boldsymbol{n}) : \mathbb{R}^{D+2} \to \mathbb{R}$ that satisfies the consistency property

$$f(c^-, c^+, \boldsymbol{n}) = -f(c^+, c^-, -\boldsymbol{n}). \tag{4.7}$$

Incorporating these definitions into (4.4) leads to the local form

$$\int\limits_{\mathcal{K}_i} \frac{\partial c_i}{\partial t} \Phi_{i,j} \, dV + \underbrace{\sum_{e=1}^{E_i} \int\limits_{\mathcal{E}_{i,e}} f(c^-, c^+, \boldsymbol{n}) \, \Phi_{i,j} \, dA - \int\limits_{\mathcal{K}_i} \boldsymbol{f}(c_i) \cdot \nabla \Phi_{i,j} \, dV}_{=: (\boldsymbol{f}_i)_j} = 0 \tag{4.8}$$

of a semi-discrete set of equations based on the DGM. For the numerical evaluation of the discrete operator $\boldsymbol{f}_i = \boldsymbol{f}_i(t, \boldsymbol{c}_i) \in \mathbb{R}^M$, we use (tensor-product) Gauss-Legendre quadrature rules of appropriate order (also, see Section 5.1). It can be shown that the resulting scheme, owing to the requirements on $f$, is consistent and locally conservative by construction (e.g., see Cockburn (2003)). Still, the actual choice of $f$ does have important implications for the stability and the accuracy for the scheme, which is why a sensible choice depends on the actual application.

### 4.2.1   Numerical flux for the Euler equations

Adequate choices concerning the numerical flux function for a specific hyperbolic conservation law such as the Euler equations have been discussed in great detail by many authors (e.g., see Toro (2009) and LeVeque (2010) and the references therein). Highly specialized and efficient fluxes such as the well-known Harten Lax van Leer Contact (HLLC) flux enjoy great popularity in the community (Toro, Spruce & Speares (1994), Batten, Clarke, Lambert & Causon (1997), Qiu et al. (2006)). However, this type of fluxes is typically tailored to ideal gases, whereas a significant part of this work will be devoted to the study of the EOS presented in Section 2.2.

As a consequence, we resort to one of the simplest numerical flux functions available, namely the Rusanov (or *local* Lax-Friedrichs) flux,

$$f(c^-, c^+, \boldsymbol{n}) = \frac{\boldsymbol{f}(c^-) + \boldsymbol{f}(c^+)}{2} \cdot \boldsymbol{n} - \frac{C_R}{2}(c^+ - c^-), \tag{4.9}$$

where the coefficient $C_R \in \mathbb{R}^+$ is chosen according to a *local* stability criterion (Toro 2009, Chapter 10). Here, we follow the suggestion by Toro (2009) who applies an estimate based on the maximum local wave-speeds, viz.

$$C_R = \max\left(|\boldsymbol{u}^- \cdot \boldsymbol{n}| + a^-, |\boldsymbol{u}^+ \cdot \boldsymbol{n}| + a^+\right), \tag{4.10}$$

where $\boldsymbol{u}^\pm$ and $a^\pm$ denote the one-sided limits of the normal velocity and the local speed of sound, respectively. It is well-known that the Rusanov flux has favourable stability properties, but is also prone to numerical diffusion (LeVeque 2010). We still stick

with this choice because the flux can be evaluated easily irrespective of the applied EOS, while it has been argued that the impact of the selected flux function on the global accuracy tends to decrease with increasing approximation order $P$ (Feistauer et al. 2003). In Section 4.3.1, we will verify this claim using the example of an isentropic vortex in an ideal gas.

## 4.2.2 Time discretization

All numerical experiments in subsequent sections have been performed with classical explicit Runge-Kutta (RK) schemes with orders from ranging from 1 to 4. That is, we apply a standard RKDGM analogous to the scheme originally introduced by Cockburn et al. (1989) without any limiters. This also holds for the calculations of the Ringleb flow 4.3.2 where we use a 4th order RK pseudo time-stepping procedure for the full unsteady equations in order to arrive at the steady-state. Even though being far from optimal in terms of computational efficiency, we still use this approach because we are mainly interested in unsteady problems such as the isentropic vortex examples presented in Section 4.3.1.

We now aim at rewriting Equation (4.8) as a system of coupled ODEs. To that end, we reformulate the temporal term as

$$\int_{\mathcal{K}_i} \frac{\partial c_i}{\partial t} \Phi_{i,j} \, dV = \int_{\mathcal{K}_i} \frac{\partial}{\partial t} \left( \sum_{k=0}^{M} c_{i,k}(t) \, \Phi_{i,k}(\boldsymbol{x}) \right) \Phi_{i,j} \, dV \tag{4.11}$$

$$= \sum_{k=0}^{M} \frac{\partial c_{i,k}}{\partial t} \underbrace{\int_{\mathcal{K}_i} \Phi_{i,k} \Phi_{i,j} \, dV}_{=:(\boldsymbol{M}_i)_{k,j}} \tag{4.12}$$

$$= \boldsymbol{M}_i \frac{\partial \boldsymbol{c}_i}{\partial t}, \tag{4.13}$$

where $\boldsymbol{M}_i \in \mathbb{R}^{M,M}$ denotes the cell-local, symmetric mass matrix associated with $\mathcal{K}_i$. It directly follows that the system of evolution equations for the numerical solution can be summarized as

$$\frac{\partial \boldsymbol{c}_i}{\partial t} + \boldsymbol{M}_i^{-1} \boldsymbol{f}_i = \boldsymbol{0}, \tag{4.14}$$

which further simplifies to

$$\frac{\partial \boldsymbol{c}_i}{\partial t} + \boldsymbol{f}_i = \boldsymbol{0} \tag{4.15}$$

since we have assumed an orthonormal basis $\{\Phi_{i,j}\}_{j=1,...,M}$.

$$
\begin{array}{c|c}
\boldsymbol{\beta} & \boldsymbol{\Gamma} \\
\hline
 & \boldsymbol{\alpha}^{\mathsf{T}}
\end{array}
\qquad
\begin{array}{c|c}
0 & \\
\hline
 & 1
\end{array}
\qquad
\begin{array}{c|cc}
0 & \\
1 & 1 \\
\hline
 & \frac{1}{2} & \frac{1}{2}
\end{array}
\qquad
\begin{array}{c|ccc}
0 & \\
\frac{1}{3} & \frac{1}{3} \\
\frac{2}{3} & 0 & \frac{2}{3} \\
\hline
 & \frac{1}{4} & 0 & \frac{3}{4}
\end{array}
\qquad
\begin{array}{c|cccc}
0 & \\
\frac{1}{2} & \frac{1}{2} \\
\frac{1}{2} & 0 & \frac{1}{2} \\
1 & 0 & 0 & 1 \\
\hline
 & \frac{1}{6} & \frac{2}{6} & \frac{2}{6} & \frac{2}{6}
\end{array}
$$

(a) General    (b) Explicit Euler    (c) Trapezoidal rule    (d) 3rd order TVD    (e) Classical RK (4th
               (1st order)        (2nd order)         (3rd order)          order)
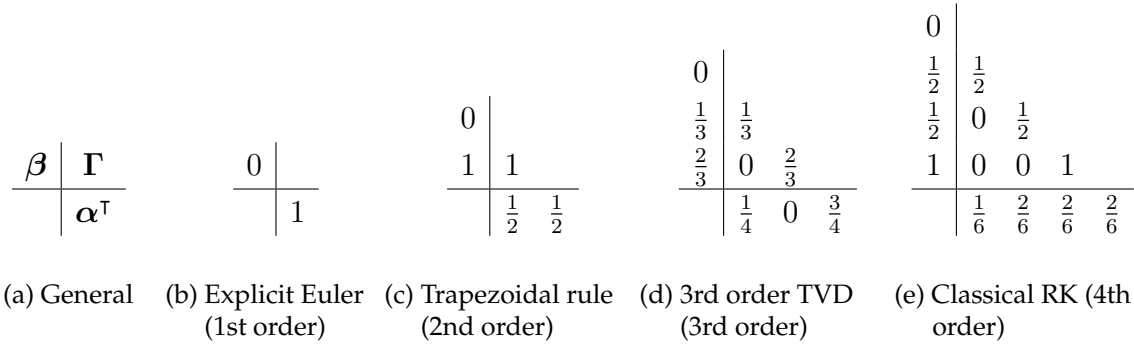
Figure 4.1: Butcher tableaus for the applied explicit Runge-Kutta methods

This system of ODEs can be advanced from an instant $t_0$ with a known solution to a new instant $t_1$ by virtue of an explicit RK scheme with $S$ stages. To that end, the new coefficients are calculated from

$$
\boldsymbol{c}_i(t_1) = \boldsymbol{c}_i(t_0) - \Delta t \sum_{s=1}^{S} (\boldsymbol{\alpha})_s \boldsymbol{k}_s,
\tag{4.16}
$$

where

$$
\boldsymbol{k}_s = \boldsymbol{f}_i \left( t_0 + (\boldsymbol{\beta})_s \, \Delta t, \, \boldsymbol{c}_i(t_0) + \Delta t \sum_{t=1}^{S} (\boldsymbol{\Gamma})_{s,t} \, \boldsymbol{k}_t \right)
\tag{4.17}
$$

and $\Delta t = t_1 - t_0$. The coefficients $\boldsymbol{\alpha} \in \mathbb{R}^S$, $\boldsymbol{\beta} \in \mathbb{R}^S$ and $\boldsymbol{\Gamma} \in \mathbb{R}^{S,S}$ are specific for a particular RK variant and determine the properties of the time integration scheme in terms of accuracy and stability. Several names for the different variants of the RK schemes have been introduced in literature. As a consequence, the values for the coefficients of the respective RK methods used in this work are summarized in the *butcher tableaus* (Butcher (1987), Gottlieb & Shu (1998)) in Figure 4.1 for the sake of clarity. More details regarding this topic can be found in any related textbook, for example in the work by Press (2007) and the references therein.

It is well-known that the Courant-Friedrichs-Levy (CFL) criterion denotes a necessary condition for the stability of an explicit Euler time discretization for a class of spatial discretizations of linear, hyperbolic PDEs (LeVeque 2010). In short, the criterion states that the temporal step-size $\Delta t$ must not be larger than the largest propagation velocity $\underline{u} \in \mathbb{R}^+$ divided by a suitable measure for the spatial resolution of a scheme, which is why it is often written as

$$
\Delta t \le c_{\mathrm{CFL}} \frac{h}{\underline{u}}
\tag{4.18}
$$

with a positive constant $c_{\mathrm{CFL}} \le 1$ that depends on the applied spatial discretization procedure.

While the largest propagation velocity in the context of the Euler equations is obviously given by $\underline{u} = \|\boldsymbol{u}\| + a$, a generalization of Equation (4.18) for the DGM has to account

for the influence of the approximation order $P$ (Cockburn & Shu 1991). Cockburn & Shu (2001) have argued that

$$\Delta t \leq \frac{c_{\text{CFL}}}{2P+1} \frac{h}{\|\boldsymbol{u}\| + a} \tag{4.19}$$

can be used as a sufficiently accurate estimate for the true stability limit of a DGM in practical applications. As a consequence, we have used Equation (4.19) in the remainder of this work.

## 4.3  Numerical results

In the evaluation of our implementation of the DGM stated above, it is convenient to make use of the fact that the analytical solutions for all considered test cases are homentropic. Most notably, this implies that the constants in the isentropic relations (2.20), (2.27) and (2.37) are invariable throughout the computational domain and for all times, which is why a measure for the entropy error is given by the deviation of the computed constant from the value following from the initial solution. We hence verify our implementation by computing the entropy error from the $L^2$ norm of this quantity. In case of an ideal gas, for example, we evaluate the entropy error at time $t$ according to

$$\left\| \frac{p(\boldsymbol{x}, t)}{\rho(\boldsymbol{x}, t)^{\gamma}} - \frac{p(\boldsymbol{x}, 0)}{\rho(\boldsymbol{x}, 0)^{\gamma}} \right\|_2. \tag{4.20}$$

It should be noted, however, that the absolute value of the entropy error is only comparable for flows comprising identical fluids.

### 4.3.1  Isentropic vortex

As a first test case, we study the moving isentropic vortices introduced in Section 3.1. The transient nature of the problem and the knowledge about smooth, analytic solutions at all times enable us to verify both, the temporal and the spatial convergence of our implementation. To this end, we study the time evolution in the periodic computational domain $[-10, 10] \times [-10, 10]$ on equidistant, rectangular grids with the settings $(u', v')^{\mathsf{T}} = (1, 0)^{\mathsf{T}}$ and $(u', v')^{\mathsf{T}} = (20, 0)^{\mathsf{T}}$ for the temporal and the spatial convergence studies, respectively.

Spatial convergence studies have been performed on successively refined grids with $40 \times 40$, $80 \times 80$, $160 \times 160$, $320 \times 320$ and $640 \times 640$ cells. For the time integration, we have applied the 4th order Runge-Kutta method (cf. Figure 4.1e) with $c_{\text{CFL}} = 0.05$ such that the global errors evaluated at $t = 0.1$ are dominated by spatial effects.

Temporal convergence studies have been performed with fixed time-step sizes $\Delta t \in \{$ 0.0004, 0.0002, 0.0001, 0.00005, 0.000025 $\}$ using $P = 13$ on a coarse grid with $20 \times 20$ cells. Errors have been measured at $t = 0.256$, that is after the vortex has crossed approximately a quarter of the computational domain. The spatial resolution for this

test case has to be extremely high in order to ensure that the global error is dominated by the temporal error. Despite the fact that we have applied a 13th order modal basis, we still observe a lower bound for the global error in the order of $10^{-11}$. Using even finer spatial resolutions would entail an even stricter CFL constraint, thus enforcing time-step sizes with associated temporal errors in the order of the machine accuracy. As a result, we abstain from further increasing the spatial resolution and omit values clearly deteriorated by the spatial error in the evaluation of the EOC (i.e., $\Delta t = 0.00005$ and $\Delta t = 0.000025$ for the 4th order Runge-Kutta scheme). Affected convergences rates are marked with an asterisk.

### 4.3.1.1 Ideal gas

In the first configuration, we study a vortex in an ideal gas ($\gamma = 1.4$) with initial conditions (3.5), (3.6) and (3.7). The integration constant $c_1$ is set to unity in order to fix the density and the pressure in the far-field to unity, which is consistent with

$$\frac{p}{\rho^\gamma} = 1 \qquad (4.21)$$

throughout the domain.

Results for the spatial convergence study based on the Rusanov flux and the HLLC flux are shown in Figure 4.2. The HLLC flux has been implemented in the variant proposed by Toro (2009, Chapter 10) that has already been used by Müller (2011). In all cases, the measured EOC using the Rusanov flux is reasonably close the expected rate of $O(h^{P+1})$, except for $P = 2$ and $P = 4$ where we observe a slightly reduced EOC. The HLLC scheme, on other hand, does not exhibit such a behaviour, even though the error is not in all configurations lower than for the Rusanov flux, as it would be expected. This finding can be attributed to the flow regime covered by the test case. That is, the considered flow is smooth, while the HLLC flux has been tailored towards an improved resolution of shocks and contact discontinuities. At the same time, the temporal convergence study using the Rusanov flux (see Figure 4.3) reveals that the EOC matches the expected rate of the selected Runge-Kutta scheme in all cases. In the light of this result in combination with the observation that the difference in the errors in Figure 4.2 decrease as the Ansatz order $P$ is increased, we conclude that the Rusanov flux is a sensible choice for the flow regimes covered in this work.

### 4.3.1.2 Stiffened gas

We now repeat the above test case with a slightly stiffened gas ($\gamma = 1.4$, $\pi = 15$). For the specification of the initial conditions, we use Equation (3.5), Equation (3.8) and Equation (3.9). The integration constant $c_1$ has to be chosen such that the pressure
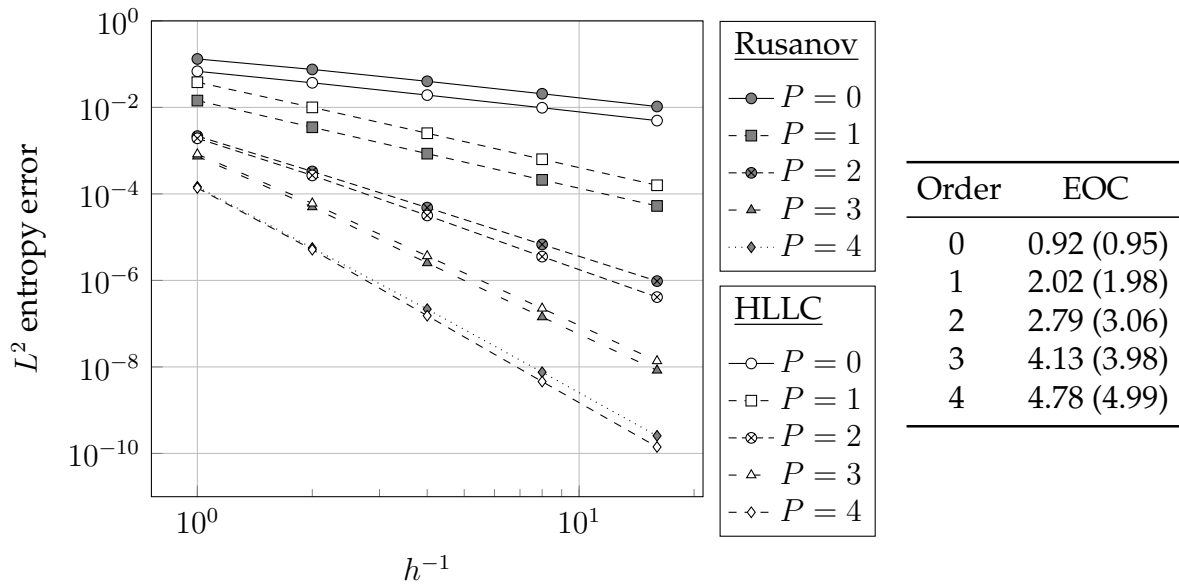
Figure 4.2: Results of the $h$-convergence study for an isentropic vortex in an ideal gas ($\gamma = 1.4$) using the Rusanov flux and the HLLC flux. Convergence rates for the HLLC flux are given in parentheses
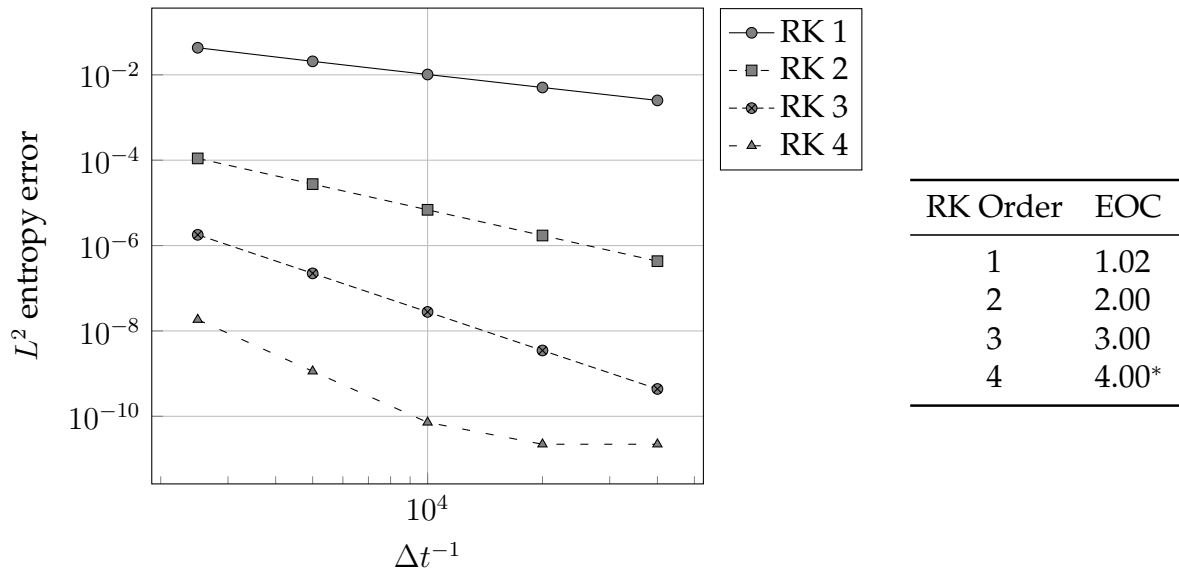


Figure 4.3: Results of the temporal convergence study for an isentropic vortex in an ideal gas ($\gamma = 1.4$)

| Order | EOC |
|-------|------|
| 0 | 0.89 |
| 1 | 2.10 |
| 2 | 2.75 |
| 3 | 3.98 |
| 4 | 4.67 |
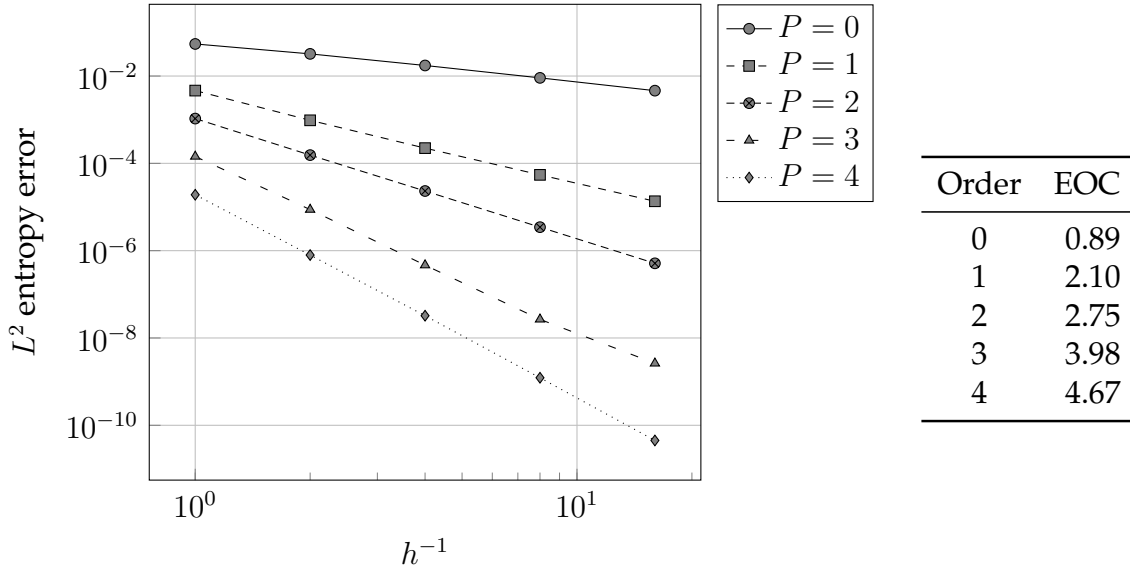
Figure 4.4: Results of the $h$-convergence study for an isentropic vortex in a stiffened gas ($\gamma = 1.4$, $\pi = 10$)

field is positive throughout the entire domain. Here, we set $p(r \to \infty) = 10$ which corresponds to $c_1 \approx 2.35$. Finally, the density in the far-field follows from

$$\frac{p + \pi}{\rho^\gamma} = 1 \qquad (4.22)$$

and evaluates to $\rho(r \to \infty) \approx 8.50$.

Figure 4.4 illustrates the results for the $h$-convergence study for this case. The general trend is very similar to the case of an ideal gas, including the fact that the convergence rate for the 2nd and 4th order simulations are slightly lower than expected. In agreement with the previous test case, the results for the temporal convergence study (Figure 4.5) exhibit the expected behaviour.

### 4.3.1.3 Covolume gas

In the final configuration, we simulate the evolution of an isentropic vortex in a covolume gas ($\gamma = 1.4$, $b = 0.1$; cf. Figure 3.1 and Figure 3.2). We set the initial conditions according to Equation (3.5), Equation (3.10) and Equation (3.11), where $c_1 = 3.6$ such that $p(r \to \infty) = 1$. Enforcing

$$\frac{p}{\rho^\gamma}(1 - b\rho)^\gamma = 1 \qquad (4.23)$$

in the initial flow field leads to $\rho(r \to \infty) \approx 0.91$. Equation (3.11) is solved for $\rho$ numerically using a standard bisection strategy (Press 2007, Chapter 9.1.1) with an absolute error tolerance of $10^{-13}$ in order to evaluate the exact solution for this problem.
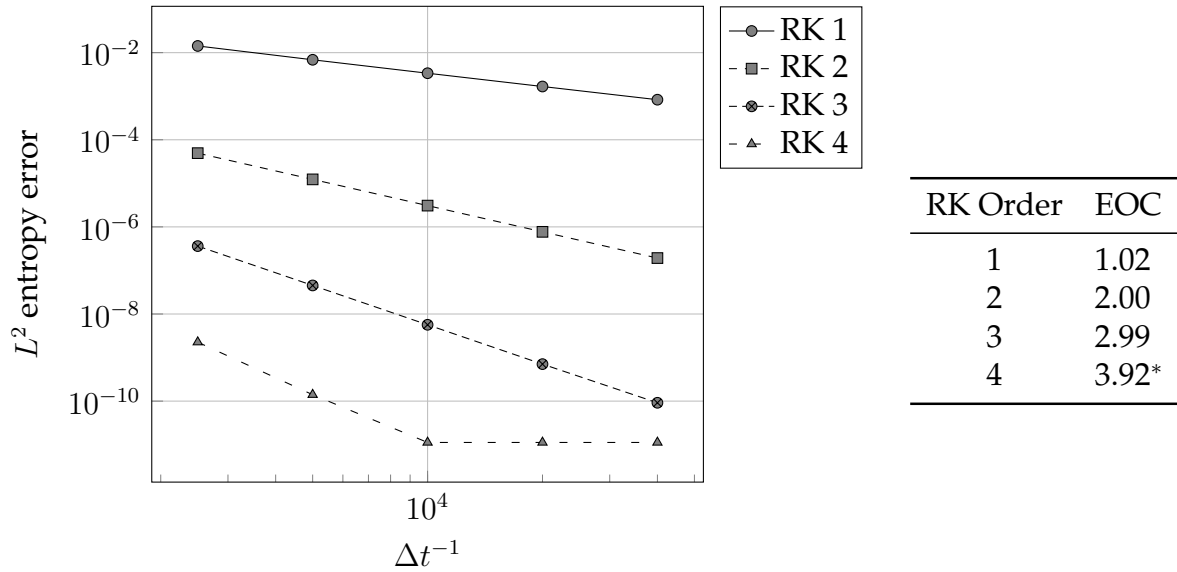
Figure 4.5: Results of the temporal convergence study for an isentropic vortex in a stiffened gas ($\gamma = 1.4$, $\pi = 10$)

In Figure 4.6, the results for the corresponding $h$-convergence study are shown. The observed EOC is in all cases very close to the rate observed for an ideal gas (cf. Figure 4.2). Similar findings also hold for the results of the temporal convergence study depicted in Figure 4.7.

## 4.3.2 Ringleb flow

In what follows, we aim at testing our implementation of the above-noted discretization of the Euler equations for an ideal gas and a stiffened gas using the example of a Ringleb flow in the specific configurations described in Section 3.2.3. To that end, we study the $h$-convergence of the discretization error on a series of successively refined, quasi-structured triangular grids. As indicated above, we solve the non-linear Euler equations to the steady state using a 4th order Runge-Kutta method.

The grids for the ideal gas case are depicted in Figure 4.8. Note that the corresponding grids for the case of the stiffened gas use the same number of cells and are of the same type, which is why we abstain from repeating them here. Figure 4.8 illustrates that we apply a piecewise linear approximation of the domain boundary. It is well-known that using a first order approximation of the problem geometry limits the attainable convergence rate of a DGM to 2nd order when standard boundary conditions are applied (Bassi & Rebay 1997). As a countermeasure, we follow the work by Halt & Agarwal (1992) by prescribing the exact solution at all boundaries of the domain.

Results for the convergence of the entropy error for the case of an ideal gas are summarized in Figure 4.9. For all approximation orders above $P = 0$, we see that the EOC is close to the optimal rate $O(h^{P+1})$. Further tests for this case (not shown) have revealed that the observed underperformance is caused by the low number of degrees

| Order | EOC |
|-------|------|
| 0 | 0.91 |
| 1 | 2.02 |
| 2 | 2.88 |
| 3 | 4.05 |
| 4 | 4.78 |
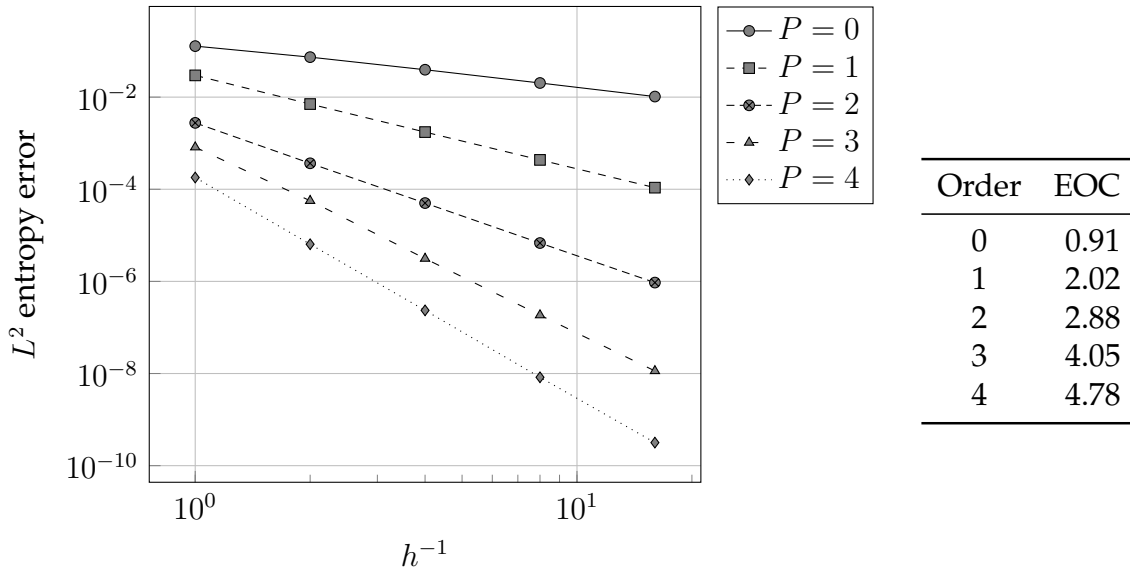
Figure 4.6: Results of the $h$-convergence study for an isentropic vortex in a covolume gas ($\gamma = 1.4$, $b = 0.1$)



| RK Order | EOC |
|----------|--------|
| 1 | 1.02 |
| 2 | 2.00 |
| 3 | 3.00 |
| 4 | 3.99* |
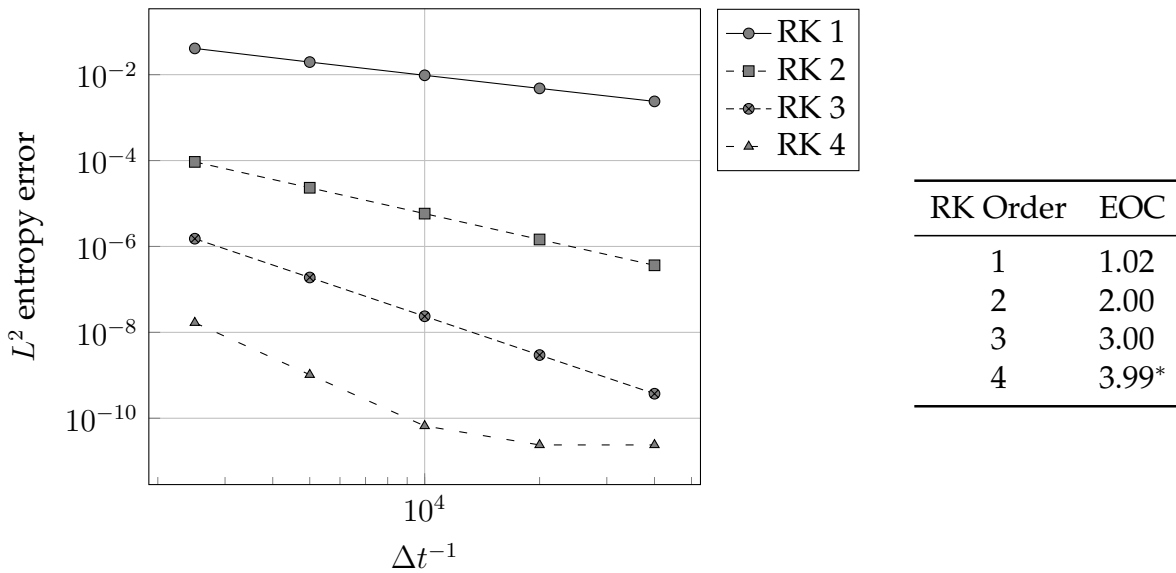
Figure 4.7: Results of the temporal convergence study for an isentropic vortex in a covolume gas ($\gamma = 1.4$, $b = 0.1$)

(a) 16 cells        (b) 64 cells        (c) 256 cells

(d) 1024 cells        (e) 4096 cells
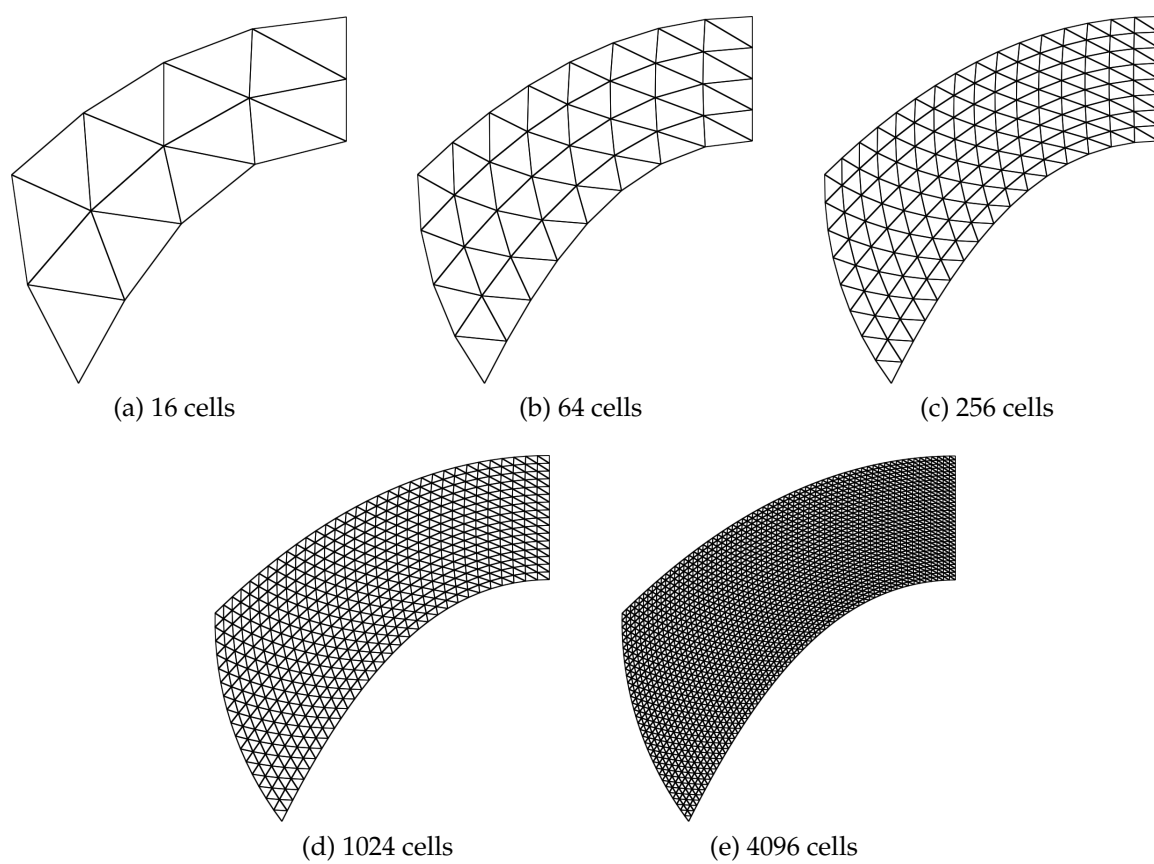
Figure 4.8: Series of grids used in the $h$-convergence study for the Ringleb flow of an ideal gas ($\gamma = 1.4$)

of freedom (DOF) on the coarsest grids, and that the expected rate is restored if further refinements are introduced.

In Figure 4.10, we see that the same findings also hold for the flow of a stiffened fluid that is outlined in Figure 3.11. Again, the measured EOC is close to $O(h^{P+1})$ for $P > 0$, while first order convergence for $P = 0$ is only restored if we introduce further grid refinements (not shown).
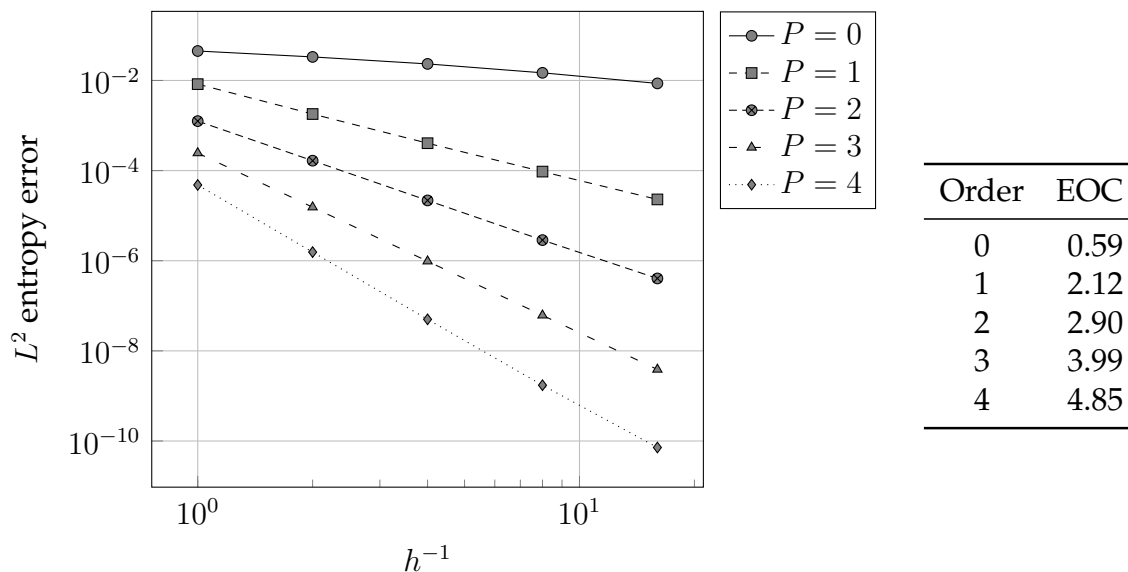
Figure 4.9: Results of the $h$-convergence study for the Ringleb flow of an ideal gas
$(\gamma = 1.4)$
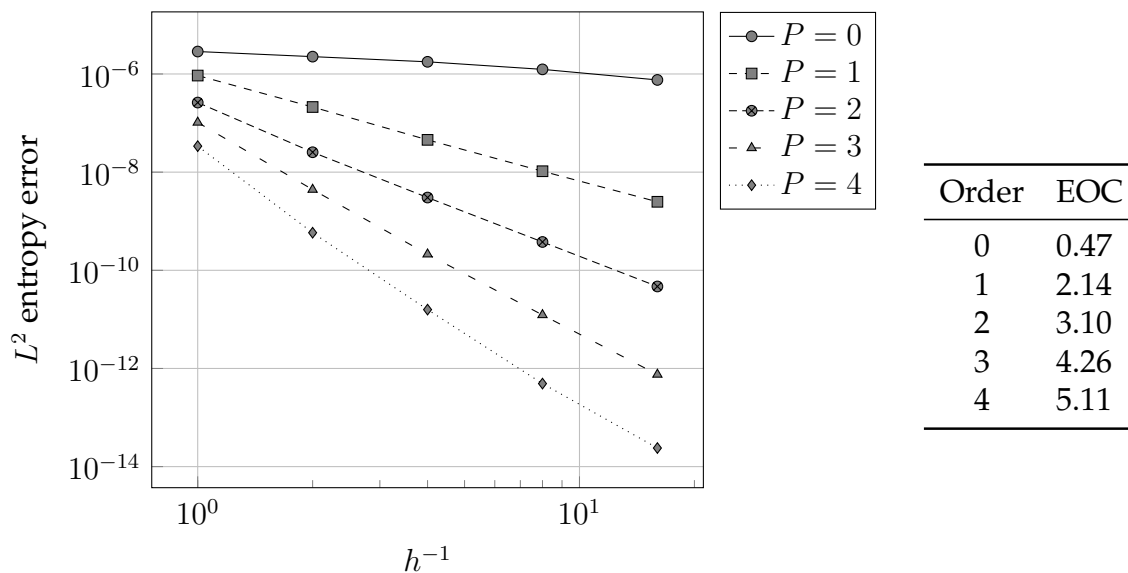


Figure 4.10: Results of the $h$-convergence study for the Ringleb flow of a stiffened gas
$(\gamma = 7.0, \pi = 10)$

# 5 Numerical integration of functions with non-smooth enrichments

Sharp-interface methods that are designed such that they can resolve locally non-smooth effects with sub-cell resolution have recently gained increasing attention. Examples include the Finite Cell Method (FCM) (Düster, Parvizian, Yang & Rank 2008), the DGM (Engwer (2009), Fröhlcke, Gjonaj & Weiland (2012), Kummer & Oberlack (2013)) and, most prominently, partition of unity methods (Melenk & Babuška (1996), Babuška & Melenk (1997)) such as the eXtended Finite Element Method (XFEM) (Moës, Dolbow & Belytschko (1999), Belytschko, Moës, Usui & Parimi (2001), Fries & Belytschko (2010)). A common challenge for all these methods is the necessity to compute integrals of generic functions over curved sub-domains of individual cells. As a direct consequence, their performance is directly linked to the affordable integration accuracy (Fries & Belytschko (2010), Lehrenfeld & Reusken (2013)), above all if higher order interfaces representations are of interest (Stazi, Budyn, Chessa & Belytschko (2003), Legay, Wang & Belytschko (2005), Fries & Zilian (2009), Dréau, Chevaugeon & Moës (2010), Legrain, Chevaugeon & Dréau (2012)).

In the light of this development, it is thus highly attractive to study methods for the numerical integration of functions over domains that are at least partly defined implicitly. That is, we partition a cell $\mathcal{K} \subset \mathbb{R}^D$ by making use of a locally smooth level set function $\varphi : \mathbb{R}^D \to \mathbb{R}$. The domains of interest are then given by the interface

$$\mathcal{I} = \left\{ \boldsymbol{x} \in \mathcal{K} : \varphi(\boldsymbol{x}) = 0 \right\} \tag{5.1}$$

and the sub-volumes

$$\mathcal{A} = \left\{ \boldsymbol{x} \in \mathcal{K} : \varphi(\boldsymbol{x}) < 0 \right\} \tag{5.2}$$

and

$$\mathcal{B} = \left\{ \boldsymbol{x} \in \mathcal{K} : \varphi(\boldsymbol{x}) > 0 \right\}. \tag{5.3}$$

Exemplary configurations for a quadrilateral cell are depicted in Figure 5.1, where the level set normal vector is defined as $\boldsymbol{n}_{\mathcal{I}} = \nabla\varphi / \|\nabla\varphi\|$.

Within this setting, we are interested in volume integrals of the type

$$\int_{\mathcal{A}} g \, dV = \int_{\mathcal{K}} H(-\varphi) \, g \, dV \tag{5.4}$$

and surface integrals of the types

$$\int_{\mathcal{I}} g \, dA = \int_{\mathcal{K}} \delta(\varphi) \, g \, dV \tag{5.5}$$
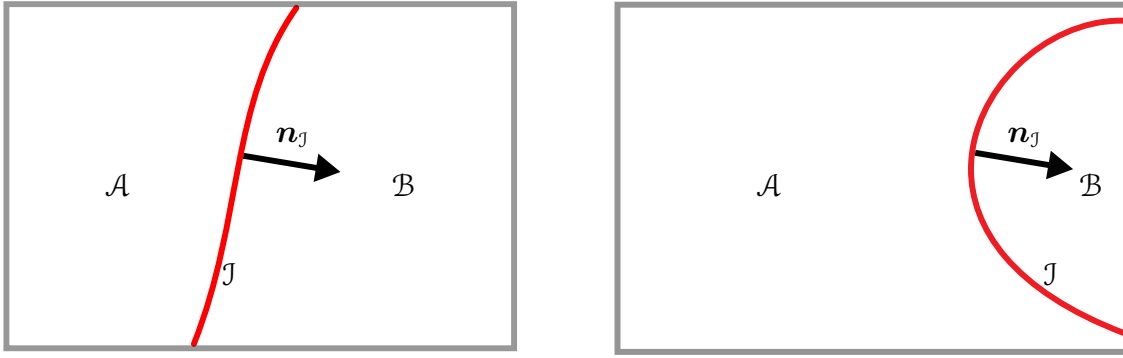
(a) Standard case where the sign of the level set function varies between the vertices of $\mathcal{K}$



(b) Special case where the level set function has the same sign in every vertex

Figure 5.1: Visualization of the domains of interest for exemplary locations of the interface $\mathcal{I}$

and

$$\int_{\mathcal{I}} \boldsymbol{g} \cdot \boldsymbol{n}_{\mathcal{I}} \, dA = \int_{\mathcal{K}} \delta(\varphi) \, \boldsymbol{g} \cdot \boldsymbol{n}_{\mathcal{I}} \, dV, \tag{5.6}$$

where $g : \mathbb{R}^D \to \mathbb{R}$ and $\boldsymbol{g} : \mathbb{R}^D \to \mathbb{R}^D$ are a sufficiently smooth integrands, $\delta : \mathbb{R} \to \mathbb{R}^\infty$ is the Dirac delta distribution and $H : \mathbb{R} \to \mathbb{R}$ is the Heaviside function. Here and in the following, we have focused on the sub-domain $\mathcal{A}$ for the sake of brevity. Some comments about the implications of alternative choices of the domain of integration will be given in Appendix B.

As it has already been mentioned, such expressions commonly appear in discretizations where interfaces are not aligned with the computational grid. Moreover, $g$ is often not easily tractable since it is given by the evaluation of the numerical approximation of a generic differential operator. As a consequence, we will first give a brief overview over existing techniques for the numerical integration of smooth functions on standard domains $\mathcal{K}$ in Section 5.1. In Section 5.2, we will then discuss existing approaches for the setting described above, while Section 5.4 and Section 5.5 will be concerned with the presentation of two new approaches that have been developed during the course of this thesis. Finally, we will present numerical results for these methods in Section 5.6.

## 5.1   Numerical integration of smooth integrands

The multi-dimensional numerical integration of generic, smooth functions over simple domains has been studied for a long time and in great detail (e.g., see Stroud (1972) or Cools (2003)). In the following, we will briefly summarize some results for the special case of integrands from the space of polynomials of maximum degree $P$ on $\mathcal{K}$, hereafter denoted by $\mathcal{P}_{\mathcal{K}}(P)$. Let $\mathcal{F} = \{f_i\}_{i=1,\dots,N}$ be a basis of $\mathcal{P}_{\mathcal{K}}(P)$. A set of nodes $\mathcal{X} =$

$\{\boldsymbol{x}_j\}_{j=1,\ldots,M} \subset \mathbb{R}^{D\times M}$ in combination with a vector of weights $\boldsymbol{w} = (w_1, \ldots, w_M)^\mathsf{T} \subset \mathbb{R}^M$ is called a *quadrature rule* if

$$\int_{\mathcal{K}} f_i \, dV \approx \sum_{j=1}^{M} w_j \, f_i(\boldsymbol{x_j}) \quad \forall i, \tag{5.7}$$

i.e. if it can be used to approximate the integrals of the elements of $\mathcal{F}$ (and thus $\mathcal{P}_{\mathcal{K}}(P)$) over $\mathcal{K}$ by means of function evaluations only. A quadrature rule is called *of order $P$* if the approximation error is zero for all elements of $\mathcal{P}_{\mathcal{K}}(P)$.

In one space dimension, Gaussian quadrature rules require $M$ function evaluations in order to integrate

$$N = 2M - 1 \tag{5.8}$$

basis functions exactly (e.g., see Stroud (1966)). It is well-known that the number of evaluations is optimal in this case. But the situation is much more complex for $D > 1$, where, to the best of our knowledge, a formula for the minimum number of nodes for a given domain is yet to be found. Still, considering the optimality of Gaussian quadrature rules in one dimension, it seems reasonable to expect that a $M$-point quadrature rule cannot integrate more than

$$N = (D + 1)M - 1 \tag{5.9}$$

basis functions exactly. Following Xiao & Gimbutas (2010), we will refer to quadrature rules of this type as *optimal* or *generalized Gaussian* quadrature rules.

The quadrature rules for smooth integrands used within the scope of this work are derived from tensor products of one-dimensional Gauss-Legendre quadrature rules (Stroud 1972). Additionally, we also use these rules as a basis for the construction of quadrature rules for non-smooth integrands in Section 5.4 and Section 5.5.

## 5.2 State of the art for non-smooth integrands

Conventional quadrature rules for $\mathcal{K}$ (Stroud (1972), Cools (2003)) rely on sufficient smoothness of the integrand and are hence not suitable for the evaluation of the integrals indicated by the right-hand sides of Equation (5.4), Equation (5.5) and Equation (5.6). At the same time, $\mathcal{J}$ and $\mathcal{A}$ are only given implicitly, which is why a standard transformation of the physical integration domain onto a simpler reference domain is not easily available.

A number of remedies for this problem have been reported in literature. A straightforward approach can be obtained by regularizing the non-smooth part of the integrand. For example, the singular Delta distribution in Equation (5.5) can be replaced by a smooth function $\delta_\epsilon : \mathbb{R} \to \mathbb{R}$ (with a positive *regularization width $\epsilon$*) that satisfies the properties

$$\lim_{\epsilon \to 0} \delta_\epsilon(x) = \delta(x) \tag{5.10}$$

and

$$\int\limits_{-\infty}^{\infty} \delta_\epsilon(x)\,dx = \int\limits_{-\infty}^{\infty} \delta(x)\,dx = 1. \tag{5.11}$$

The regularized integrand may then be integrated with the aid of conventional quadrature rules. Related methods have been studied extensively for a long time (Osher & Fedkiw (2002), Tornberg (2002), Tornberg & Engquist (2003), Tornberg & Engquist (2004), Engquist, Tornberg & Tsai (2004), Smereka (2006), Towers (2007), Zahedi & Tornberg (2010)) and are appealing due to their simplicity. On the downside, the integration accuracy strongly depends on the choice of $\epsilon$. If $\epsilon$ is too small, for example, the regularized function will still be to steep and the quadrature error will be high. Large values for $\epsilon$, on the other hand, will result in an *analytical* error since the support of $\delta_\epsilon$ will be significantly larger than the cell $\mathcal{K}$. As a result, generally consistent regularizations are hard to define and are limited in terms of overall accuracy on general grids.

A second well-known class of methods relies on an explicit reconstruction of the interface $\mathcal{I}$. In the majority of the cases, a piecewise linear approximation $\mathcal{I}_1$ of $\mathcal{I}$ is introduced (Min & Gibou (2007), Min & Gibou (2008), Engwer (2009)), which renders it straightforward to apply conventional quadrature rules on $\mathcal{I}_1$. Min & Gibou (2007) have demonstrated that this approach can lead to a 2nd order scheme that is highly robust under perturbations of the interface location. The rate of convergence can be increased by resorting to higher order reconstructions, i.e. approximations $\mathcal{I}_P$ of $\mathcal{I}$ where $P \in \mathbb{N}$ with $P > 1$. Methods of this type have been applied by several authors (Legay et al. (2005), Cheng & Fries (2010)), but, to the best of our knowledge, no extensions to general, three-dimensional element types have been reported in literature for $P > 2$.

Both classes of methods are typically complemented by strategies that decrease the *effective* local mesh size by recursively partitioning a cell $\mathcal{K}$ into intersected and non-intersected quadrature sub-cells. Such *tree-based* strategies (Strain 1999) then rely on the application of one of the above-mentioned (or related) methods on the leaves of the subdivision tree. We will present more details on this topic as well as a new method based on a similar technique in Section 5.4.

Apart from these rather classical ideas, Wen has studied a fundamentally different approach in a series of papers (Wen (2007), Wen (2008), Wen (2009), Wen (2010)) discussing the projection of the level set onto the grid axes and splitting multi-dimensional integrals into a series of one-dimensional integrals. The presented method appears to be promising in case of a regular distribution of grid points (i.e., on an equidistant, Cartesian mesh) where the author is able to achieve excellent results. Unfortunately, the required transformations are quite complex and a generalization to more general configurations seems out of reach.

Quite recently, optimization based methods have attracted some attention. In a first step, Bremer, Gimbutas & Rokhlin (2010) and subsequently Xiao & Gimbutas (2010) have studied the generation of quadrature rules for fixed generic domains. The general ideas go back to Karlin & Studden (1966) who introduced the so-called *moment-fitting*

system as a basis for a non-linear optimization procedure that can be used to determine the nodes and weights of a quadrature rule. The above-mentioned method has been proven to be extremely effective for the pre-calculation of efficient quadrature rules that are optimal or nearly-optimal in terms of the number of quadrature points, even in case of non-convex polygonal domains (Mousavi & Sukumar (2010), Mousavi, Xiao & Sukumar (2010)).

Later on, Mousavi & Sukumar (2011) and Sudhakar & Wall (2013) have shown how the non-linear optimization procedure can be reduced to a linear one if piecewise a linear interface is assumed, thus rendering the approach practicable in a broader range of applications (e.g., if the interface movement is significant). Still, the restriction to piecewise linear interface approximations makes a refinement near curved boundaries inevitable and one has to apply an adaptive procedure in order to improve the accuracy. In Section 5.5, we hence present a new method that aims at removing the drawbacks of piecewise linear interface approximations, but without having to perform a complex and potentially problematic higher order reconstruction of the interface.

## 5.3   A note on terminology

In the remainder of this chapter, we will repeatedly make use of Gauss' theorem in order to rewrite volume integrals over a generic polytope $\mathcal{K} \subset \mathbb{R}^D$ as a surface integral over $\partial\mathcal{K}$, and vice versa. Moreover, we will often consider the individual edges of $\Omega$ separately in order to describe the corresponding integration procedure. Recalling the notation introduced in Section 4.2, we therefore address the edges $\{\mathcal{E}_e\}_{e=1,\dots,E}$ of $\mathcal{K}$ as $(D-1)$-dimensional *volume* elements. A *surface* integral over $\partial\mathcal{K}$ thus consists of $E$ distinct, $(D-1)$-dimensional *volume* integrals over the edges $\mathcal{E}_e$.

Especially in three dimensions, this terminology allows for a convenient and consistent identification of the type of integrals that we evaluate on $\mathcal{K}$, $\partial\mathcal{K}$ and even $\partial(\partial\mathcal{K})$. Integrals over $\partial(\partial\mathcal{K})$ are then regarded as $(D-1)$-dimensional *surface* integrals that can be computed from the sum of multiple *volume* integrals over $(D-2)$-dimensional (line) elements.

## 5.4   Simple integration using tree-based adaptivity

Subsequently, we will present a new method for the numerical approximation of the integrals (5.4), (5.5) and (5.6) that has been introduced by Müller, Kummer, Oberlack & Wang (2012). To that end, we will introduce a subdivision-based quadrature for the volume case in the first part. The formulation is relatively standard, and we will thus focus our attention on some details of the subdivision procedure that are a common source of problems for this type of Ansatz. In the second part, we will then show how one can reduce the surface case to the volume case by making use of the derivative information associated with $\varphi$, which is readily accessible if a higher order method is used for its representation.

(a) Line      (b) Triangle      (c) Quadrilateral      (d) Hexahedron
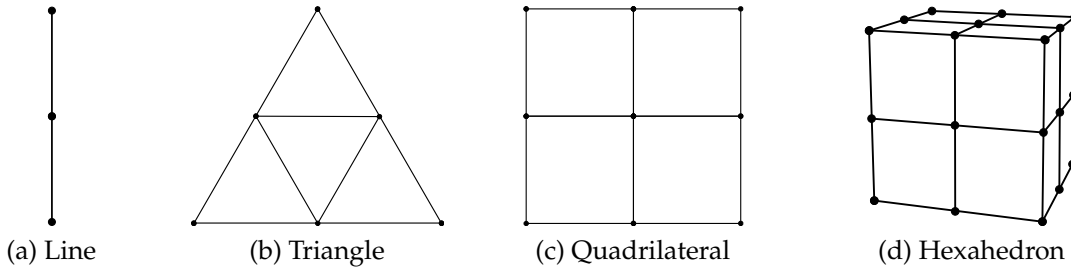
Figure 5.2: Reference polytopes subdivided using the transformations $\boldsymbol{D}_k$. Visible vertices of the sub-polytopes are indicated by black dots

## 5.4.1   Volume integration

The volume integration is based on the subdivision of admissible polytopes $\mathcal{K}$. A subdivision consists of suitable transformations of a reference polytope $\mathcal{K}^0 \subset \mathbb{R}^D$ with vertices $\{\boldsymbol{v}_v^0\}_{v=1,\ldots,V}$ for which a tessellation

$$\mathcal{K}^0 = \mathcal{K}_1^0 \cup \ldots \cup \mathcal{K}_S^0 \tag{5.12}$$

of the form

$$\mathcal{K}_s^0 = \boldsymbol{E}_s(\mathcal{K}^0) \quad \forall s \in \{1, \ldots, S\} \tag{5.13}$$

exists. Here, the $\boldsymbol{E}_s : \mathbb{R}^D \to \mathbb{R}^D$ represent elementary, affine linear transformations that map the vertices of $\mathcal{K}^0$ onto the vertices of $\mathcal{K}_s^0$. The reference polytopes studied in this work have been visualized in Figure 5.2. Details about the individual reference configurations and the corresponding subdivisions can be found in Appendix A.

The simple structure of the elementary transformations allows for an efficient recursive composition of multiple transformations in order to obtain a *subdivision strategy*. We define a subdivision strategy as a set of compositions of elementary transformations $\mathcal{T} = \{\boldsymbol{T}_t\}_{t=1,\ldots,T}$ that define a tessellation of $\mathcal{K}^0$, i.e.

$$\mathcal{K}^0 = \boldsymbol{T}_1(\mathcal{K}^0) \cup \ldots \cup \boldsymbol{T}_T(\mathcal{K}^0). \tag{5.14}$$

For the purposes of this work, we propose a subdivision strategy based on a $S$-tree (e.g., see Strain (1999)). Consequently, we recursively subdivide each (sub-)polytope which is considered cut by the interface $\mathcal{I}$. A simple method for detection of these elements is given by the observation that a polytope $\mathcal{K} = \mathrm{convexHull}(\boldsymbol{v}_1, \ldots, \boldsymbol{v}_V)$ is necessarily being crossed by the zero iso-contour of $\varphi$ if

$$\exists v_1, v_2 \in \{1, \ldots, V\} : \quad \mathrm{sgn}(\varphi(\boldsymbol{v}_{v_1})) \neq \mathrm{sgn}(\varphi(\boldsymbol{v}_{v_2})), \tag{5.15}$$

where $\mathrm{sgn}(x) : \mathbb{R} \to \{-1, 0, 1\}$ denotes the sign function.

Apart from the rather obvious issue that the sign can be zero for one or more of the considered vertices, it is important to note that the inverse of the above-mentioned implication does *not* hold in general. This can for example be seen in Figure 5.1b where

the level set values of all vertices share the same sign. While the issue of these special intersections can often be neglected for low order approximations of $\varphi$ or in the case of low accuracy requirements, they can be the major source of a lack of robustness under perturbations of the interface location. Min & Gibou (2007) hence proposed an additional check that considers $\mathcal{K}$ *potentially* cut if

$$\exists v \in \{1, \ldots, V\} : \quad |\varphi(\boldsymbol{v}_v)| < \frac{1}{2} \operatorname{Lip}(\varphi) \operatorname{diam}(\mathcal{K}) \tag{5.16}$$

holds. In this equation, we have introduced the notation $\operatorname{Lip}(\varphi)$ for the *Lipschitz constant* of $\varphi$ in $\mathcal{K}$, and $\operatorname{diam}(\mathcal{K})$ for the *diameter* of $\mathcal{K}$. The diameter is computed from the maximum of the distances between two vertices of $\mathcal{K}$. Equation (5.16) states that the minimum *distance* of a vertex from the interface that still guarantees that the adjacent edges cannot be intersected by the interface is dictated by the maximum feasible gradient of $\varphi$.

The exact value of $\operatorname{Lip}(\varphi)$ is usually unknown in practical applications, but, contrary to Equation (5.15), this additional check typically overestimates the number of cut (sub-)polytopes. As a result, it is safe to estimate the Lipschitz constant, for example in terms of the local gradient, that is

$$\operatorname{Lip}(\varphi) \approx \max_{v \in \{1, \ldots, V\}} \|\nabla \varphi(\boldsymbol{v}_v)\| . \tag{5.17}$$

If $\varphi$ is a reasonable approximation of a signed-distance function ($\|\nabla \varphi\| \approx 1$) in the vicinity of the interface, one may even apply

$$\operatorname{Lip}(\varphi) \approx 1. \tag{5.18}$$

The latter choice has proven to be sufficient for the purposes of this work and thus been used in all numerical examples presented in Section 5.6, even though the corresponding level set functions often strongly violate the signed-distance property.

All in all, the proposed algorithm for the subdivision of a reference polytope $\mathcal{K}^0$ with up to $L$ levels is given in Figure 5.3. The output of the algorithm for an exemplary configuration is visualized in Figure 5.4. As mentioned above, the output of the algorithm is given by a set of transformations $\{\boldsymbol{T}_t\}_{t=1,\ldots,T}$, which directly serves as input for the assembly of the adapted quadrature rule.

A reasonable choice for the quadrature rule to be used in each of the leaves of the subdivision tree depends on the desired properties of the resulting quadrature rule. For the purposes of this work, we choose a base quadrature rule $\{\mathcal{X}_t, \boldsymbol{w}_t\}$ of the same degree $P$ that is used in non-intersected cells. However, such a choice is possibly sub-optimal in *intersected* leaves. This is due to the fact that the integrand still is non-smooth in the corresponding sub-cell, which is why we simply resort to a first

1: **return** SUBDIVIDE($\mathcal{K}^0$, 0)

2: **function** SUBDIVIDE($\mathcal{K}$, depth)
3:     $\mathcal{T} \leftarrow \emptyset$
4:     **if** depth $< L$ and [(5.15) or (5.16) holds] **then**
5:         **for all** $E_s$ **do**
6:             **for all** $T \in$ SUBDIVIDE($E_i(\mathcal{K})$, depth $+ 1$) **do**      # Do recursion
7:                 $\mathcal{T} \leftarrow \mathcal{T} \cup \{E_i \circ T\}$            # Compose mappings
8:     **else**
9:         $\mathcal{T} \leftarrow \{\text{Identity}\}$            # End of recursion
10:     **return** $\mathcal{T}$

Figure 5.3: Algorithm for the adaptive subdivision strategy



(a) Subdivided cell          (b) Corresponding subdivision tree
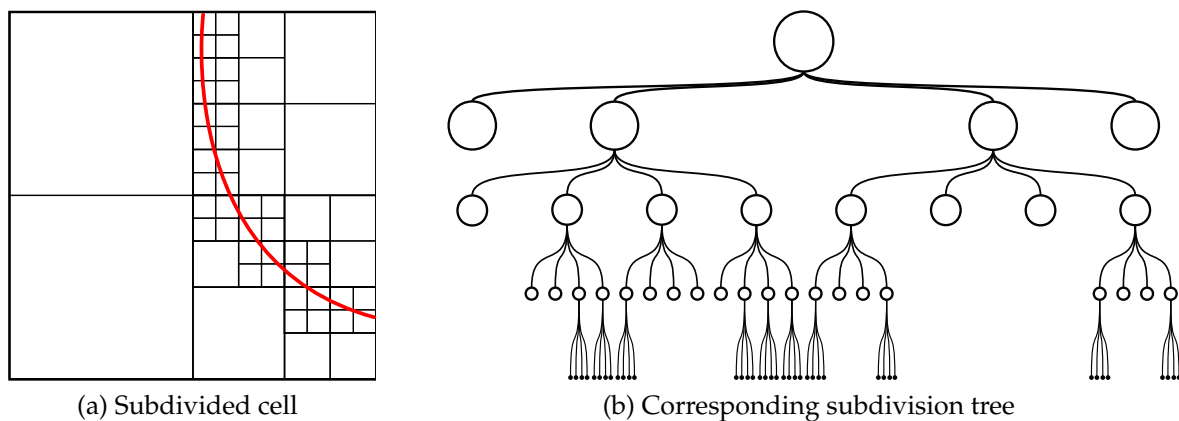
Figure 5.4: Result of the adaptive subdivision for an exemplary configuration with up to four levels of recursion

order rule $\{\mathfrak{X}_t, \boldsymbol{w}_t\}$ in this region. The subdivision $\{\mathfrak{X}, \boldsymbol{w}\}$ rule can finally be assembled via

$$\mathfrak{X} = \bigcup_{t=1}^{T} \boldsymbol{T}_t(\mathfrak{X}_t) \quad \text{and} \quad \boldsymbol{w} = \begin{pmatrix} |\det(J(\boldsymbol{T}_1))|\boldsymbol{w}_1 \\ \vdots \\ |\det(J(\boldsymbol{T}_T))|\boldsymbol{w}_T \end{pmatrix}. \tag{5.19}$$

## 5.4.2 Surface integration

Subsequently, we will focus our attention on surface integrals of the types (5.5) and (5.6), with the additional assumption that we have some derivative information about $g$ and $\boldsymbol{g}$, respectively. We start by noting that the scalar integral,

$$\int_{\mathfrak{I}} g \, dA = \int_{\mathcal{K}} \delta(\varphi) \, g \, dV, \tag{5.5, repeated}$$

is a special case of the integral over a vector-valued function, i.e.

$$\int_{\mathfrak{I}} g \, dA = \int_{\mathfrak{I}} g\boldsymbol{n}_{\mathfrak{I}} \cdot \boldsymbol{n}_{\mathfrak{I}} \, dA = \int_{\mathfrak{I}} \boldsymbol{g} \cdot \boldsymbol{n}_{\mathfrak{I}} \, dA \tag{5.20}$$

with $\boldsymbol{g} = g\boldsymbol{n}_{\mathfrak{I}}$. Consequently, the following considerations will be focused on the vector case without loss of generality.

Gauss' theorem allows us to rewrite Equation (5.6) as

$$\int_{\mathfrak{I}} \boldsymbol{g} \cdot \boldsymbol{n}_{\mathfrak{I}} \, dA = \int_{\partial A} \boldsymbol{g} \cdot \boldsymbol{n} \, dA \qquad - \int_{\partial A \backslash \mathfrak{I}} \boldsymbol{g} \cdot \boldsymbol{n} \, dA \tag{5.21}$$

$$= \int_{A} \nabla \cdot \boldsymbol{g} \, dV \qquad - \int_{\partial A \backslash \mathfrak{I}} \boldsymbol{g} \cdot \boldsymbol{n} \, dA, \tag{5.22}$$

$$= \int_{\mathcal{K}} H(-\varphi) \, \nabla \cdot \boldsymbol{g} \, dV - \int_{\partial \mathcal{K} \backslash \mathfrak{I}} H(-\varphi) \, \boldsymbol{g} \cdot \boldsymbol{n} \, dA, \tag{5.23}$$

where $\boldsymbol{n}$ is the outer unit normal vector on $\partial \mathcal{K}$ respectively $\partial A$, and $\boldsymbol{n} = \boldsymbol{n}_{\mathfrak{I}}$ on $\mathfrak{I}$. As a result, the integral over an implicitly defined surface has been reduced to multiple integrals of the type (5.4) (i.e., one on $\mathcal{K}$ plus one for every edge element in $\partial \mathcal{K}$) that have already been treated in Section 5.4.1. This new formulation has two advantages: First of all, volume and surface integrals can be treated in the same manner, which renders the method conceptually simple. Secondly, no reconstruction of geometric information for the interface $\mathfrak{I}$ is required, which allows for a straightforward implementation for generic element types.

Throughout the above-noted derivation, we have assumed that $\nabla \cdot \boldsymbol{g}$ is accessible and it should be noted that it can be computed from

$$\nabla \cdot \boldsymbol{g} = \nabla \cdot (g\,\boldsymbol{n}_{\text{J}}) \tag{5.24}$$

$$= \nabla g \cdot \boldsymbol{n}_{\text{J}} + g(\nabla \cdot \boldsymbol{n}_{\text{J}}) \tag{5.25}$$

$$= \nabla g \cdot \boldsymbol{n}_{\text{J}} + \frac{g}{\|\nabla \varphi\|}\left(\Delta \varphi - \boldsymbol{n}_{\text{J}}^{\mathsf{T}}\,\boldsymbol{H}(\varphi)\,\boldsymbol{n}_{\text{J}}\right) \tag{5.26}$$

in the scalar case, where $\boldsymbol{H}(\varphi)$ represents the Hessian of $\varphi$. In either case, we require gradient information about the integrand which might not be present in an actual application. In such a case, one should consider a derivative-free approach to numerical integration. One such strategy will be described in the following section, and we will compare the performance of both approaches using the example of some canonical test cases in Section 5.6.

## 5.5 Highly accurate integration by means of moment-fitting

Below, we will present a new method for the numerical approximation of the integrals (5.4), (5.5) and (5.6) that has been introduced by Müller, Kummer & Oberlack (2013). The method is based on the observation that, given the setting described in Section 5.1, any quadrature rule for $\mathcal{K}$ of order $P$ fulfils the so-called moment-fitting system

$$\underbrace{\begin{pmatrix} f_1(\boldsymbol{x}_1) & \dots & f_1(\boldsymbol{x}_M) \\ \vdots & \ddots & \vdots \\ f_N(\boldsymbol{x}_1) & \dots & f_N(\boldsymbol{x}_M) \end{pmatrix}}_{=:\boldsymbol{A}} \begin{pmatrix} w_1 \\ \vdots \\ w_M \end{pmatrix} = \underbrace{\begin{pmatrix} \int\limits_{\mathcal{K}} f_1\,dV \\ \vdots \\ \int\limits_{\mathcal{K}} f_N\,dV \end{pmatrix}}_{=:\boldsymbol{b}} \tag{5.27}$$

exactly (Karlin & Studden 1966). As a result, the system can be solved for the unknown weights and nodes if the right-hand side is known. Even if this is the case, the solution procedure is not straightforward, especially in higher dimensions and for larger values of $P$. This is due to the fact that the system is strongly non-linear in the nodes, contains many unknowns and, as it has been mentioned before, the optimal number of nodes is not known a priori (Bremer et al. 2010).

Therefore, we will discuss in the following how we can greatly simplify the solution of (5.27) if the following conditions are met:

1. An appropriate set of nodes $\mathcal{X}$ can be predefined.

2. A good approximation of the right-hand side can be evaluated cheaply.

In such a situation, (5.27) reduces to a possibly over- or under-determined *linear* system

$$\boldsymbol{A}\boldsymbol{w} = \boldsymbol{b} \tag{5.28}$$

which can be solved efficiently. While the obtained solution will usually be sub-optimal in the global sense, the gain in efficiency renders the approach attractive under very general conditions.

## 5.5.1 Recursive strategy

We are interested in the construction of quadrature rules for $\mathcal{A}$ as well as for $\partial\mathcal{A}$. The latter can be decomposed into the actual interface $\mathcal{I}$ and the surface $\partial\mathcal{A} \setminus \mathcal{I} = \{\boldsymbol{x} \in \partial\mathcal{K} : \varphi(\boldsymbol{x}) < 0\}$. The idea of the proposed approach is to apply a recursive strategy in order to accomplish this goal. To that end, we will manipulate the right-hand side of (5.27) such that the integrals can be evaluated on simpler domains using quadrature rules that are created in the next level of recursion. Consequently, the output of the proposed algorithm will be a *hierarchy* of quadrature rules, starting from one space dimension.

### 5.5.1.1 One-dimensional case

If $\mathcal{K}$ is one-dimensional (i.e., a line element), we construct a quadrature rule of order $P$ by finding the roots of $\varphi$ on $\mathcal{K}$. To that end, we apply a root-finding algorithm such as the safe-guarded Newton method described by Press (2007). On each of the emerging sub-sections, we use standard, one-dimensional Gaussian quadrature rules. Assuming a sufficient accuracy of the root-finding procedure, the composite quadrature rule will be exact up to numerical precision.

### 5.5.1.2 Two-dimensional case

If $\mathcal{K}$ is two-dimensional (i.e., a polygon such as a triangle or a quadrilateral), we construct a quadrature rule for $\mathcal{I}$ by reducing the integrals on the right-hand side of (5.27) to integrals over $\partial\mathcal{K} \cap \overline{\mathcal{A}}$ for a special choice of basis functions (see Section 5.5.3). Sub-domain $\partial\mathcal{K} \cap \overline{\mathcal{A}}$, in turn, is composed of several line elements which can be treated as described in the previous paragraph. Having constructed quadrature rules for $\mathcal{I}$ and $\partial\mathcal{K} \cap \overline{\mathcal{A}}$, the methods presented in Section 5.5.4 can be applied to construct a quadrature rule for $\mathcal{A}$.

### 5.5.1.3 Three-dimensional case

If $\mathcal{K}$ is three-dimensional (i.e., a polyhedron such as a hexahedron), we construct a quadrature rule for $\mathcal{I}$ by reducing the integrals on the right-hand side of (5.27) to integrals over $\partial\mathcal{K} \cap \mathcal{A}$ for a special choice of basis functions (see Section 5.5.3). Sub-domain $\partial\mathcal{K} \cap \overline{\mathcal{A}}$ is composed of a set of plane, two-dimensional domains. For each of these implicit domains, we construct volume quadrature rules using the methods presented in the previous paragraph. During this process, the algorithm will generate

(a) A cell $\mathcal{K}$ intersected by the zero iso-contour

(b) Sub-volume $\mathcal{A}$

(c) Interface $\mathcal{I}$

(d) Sub-volumes of $\partial\mathcal{K}$ confining $\mathcal{A}$, i.e. $\partial\mathcal{K} \cap \overline{\mathcal{A}}$

(e) Parts of $\mathcal{I}$ confining $\partial\mathcal{K} \cap \overline{\mathcal{A}}$, i.e. $\partial\mathcal{I}$

(f) Sub-volumes of $\partial(\partial\mathcal{K})$ confining $\partial\mathcal{A}$, i.e. $\partial(\partial\mathcal{K}) \cap \overline{\mathcal{A}}$
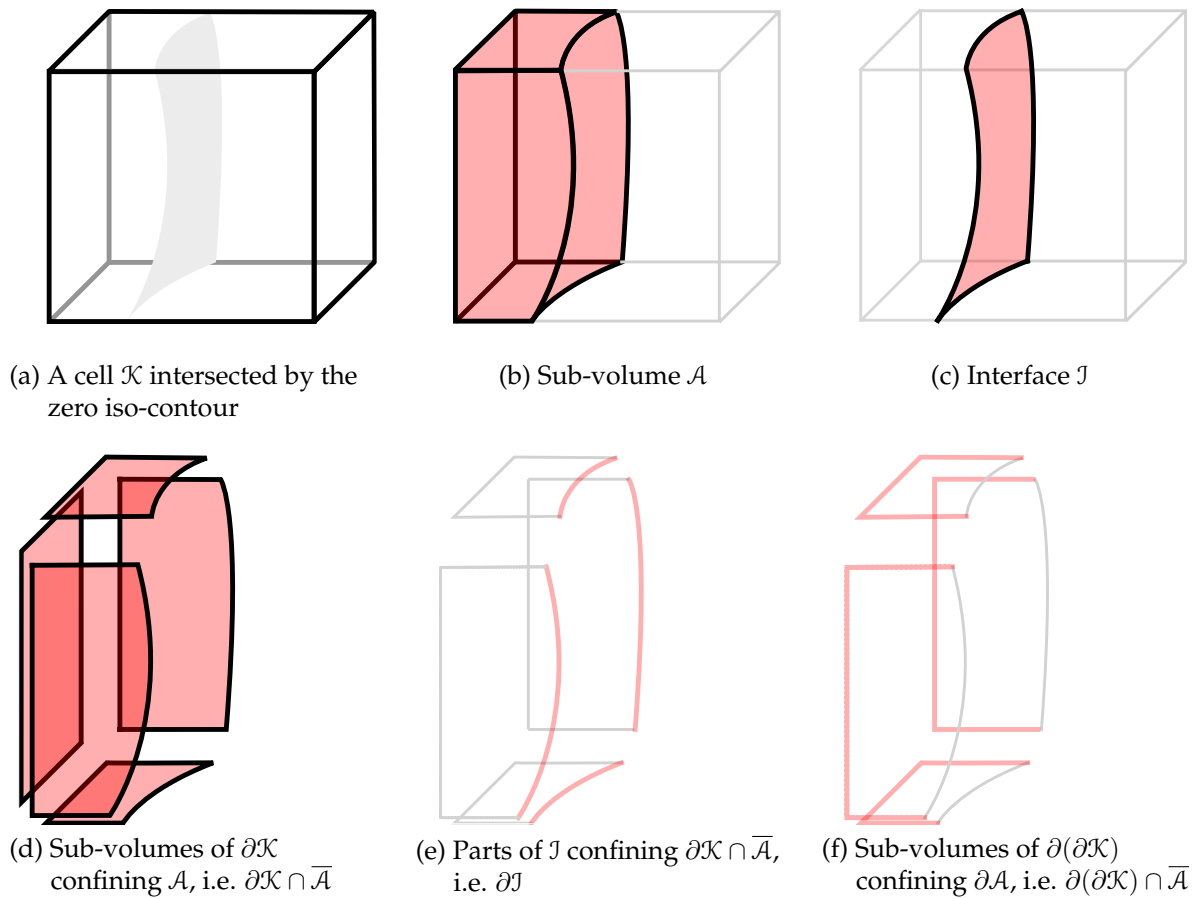
Figure 5.5: Illustration of the different domains of integration for a hexahedron intersected by the zero iso-contour of the level set

a surface quadrature rule for $\partial\mathcal{K} \cap \overline{\mathcal{I}} = \partial\mathcal{I}$ by creating a volume rule on $\partial(\partial\mathcal{K}) \cap \overline{\mathcal{A}}$. The sets involved in this process are illustrated in Figure 5.5 using the example of an intersected hexahedron.

## 5.5.2 Predefined quadrature nodes

The requirements formulated in Section 5.5 state that the set of nodes $\mathcal{X}$ should be kept constant during the optimization process. We emphasize that this does *not* imply that the quadrature nodes have to be located on $\mathcal{I}$ in the surface case or solely in $\mathcal{A}$ in the volume case. Obviously, this assumption dictates that $\mathcal{F}$ consists of smooth functions and that a smooth extension of the integrands of the surface integrals (5.5) and (5.6) from $\mathcal{I}$ to $\mathcal{K}$ is known. Fortunately, this is a very mild assumption in the setting we have described in the beginning of this chapter.

Accordingly, many options for the actual choice of the nodes are feasible, for example random and equidistant point distributions, as well as the nodes associated with traditional quadrature rules for $\mathcal{K}$. Our numerical experiments indicate that using the

latter option generally leads to the best results, which is why we follow this approach in what follows. It is worth noting that the accuracy of the surface integration can be further improved by projecting the quadrature nodes onto the actual interface $\mathcal{I}$. Nevertheless, we abstain from this approach for the following reasons:

- The projection is computationally expensive, especially if the required number of integration points is high

- While the projection works relatively well in two space dimensions, the three-dimensional case is more problematic since the naive projection of a node is regularly located outside of $\mathcal{K}$

- Using the same nodes in all cut cells allows for further optimizations in the implementation as, for example, fewer linear systems have to be solved (see Section 5.5.4).

In any case, it is sensible to make sure that the number of nodes exceeds the number of moments, i.e. that $M > N$ holds. In other words, it should be ensured that the linear system

$$\boldsymbol{A}\,\boldsymbol{w} = \boldsymbol{b} \qquad\qquad \text{(5.28, repeated)}$$

is *under*-determined in order to avoid any additional numerical errors due to the least-squares Ansatz. This can be seen from the generic definition of the least-squares solution of an under-determined system which reads

$$
\begin{aligned}
\min \ & \|\boldsymbol{w}\|^2 \\
\text{s. t. } & \boldsymbol{A}\,\boldsymbol{w} = \boldsymbol{b}.
\end{aligned}
\qquad\qquad \text{(5.29)}
$$

Here, it becomes obvious that the original system of equations has been transformed into a constraint that has to be fulfilled *exactly* by any admissible solution $\boldsymbol{w}$. The unique solution of (5.29) for the under-determined case is given by

$$\boldsymbol{w} = \boldsymbol{A}^{\mathsf{T}}(\boldsymbol{A}\boldsymbol{A}^{\mathsf{T}})^{-1}\,\boldsymbol{b} \qquad\qquad \text{(5.30)}$$

and can be obtained with the aid of any standard linear solver, but it should be taken into account that $\boldsymbol{A}$ may be rank-deficient and that the system may be severely ill-conditioned due to the fixed node distribution. Accordingly, we solve (5.28) by means of a complete orthogonal factorization using the procedure DGELSY from the Linear Algebra Package (LAPACK) (Anderson, Bai, Bischof, Blackford, Demmel, Dongarra, Croz, Greenbaum, Hammarling, McKenney & Sorensen 1999).

### 5.5.3 Surface integrals

In the following discussion concerning surface integrals, we will focus on integrals of the type

$$\int_{\mathcal{I}} g \, dA = \int_{\mathcal{K}} \delta(\varphi) \, g \, dV, \qquad\qquad \text{(5.5, repeated)}$$

while noting that the same strategy directly applies to integrals of the type (5.6) using the definition $g = \boldsymbol{g} \cdot \boldsymbol{n}_\mathbb{J}$. As mentioned before, $g$ might not be known explicitly in applications such as the spatial discretization of PDEs. Accordingly, we strive at creating a quadrature rule based on the functions in $\mathcal{F}$ that can later be used to evaluate (5.5) efficiently.

In general, the evaluation of

$$\int_\mathbb{J} f_i \, dA \tag{5.31}$$

is just as difficult as the evaluation of (5.5). However, we can define a *divergence-free* basis $\{\boldsymbol{f}_k\}_{k=1,\dots,K}$ ($\boldsymbol{f}_k : \mathbb{R}^D \to \mathbb{R}^D$) of degree $P$ associated to $\mathcal{F}$ and define a new, generally larger set $\mathcal{F}' = \{\boldsymbol{f}_k \cdot \boldsymbol{n}_\mathbb{J}\}_{k=1,\dots,K}$ of integrands $(K > N)$ for which the evaluation is much simpler. A method for the construction of a suitable divergence-free basis is described in Appendix C. Making use of this definition, we can apply Gauss' theorem in order to arrive at

$$\int_\mathbb{J} \boldsymbol{f}_k \cdot \boldsymbol{n}_\mathbb{J} \, dA = \int_{\partial\mathcal{A}} \boldsymbol{f}_k \cdot \boldsymbol{n} \, dA \;-\; \int_{\partial\mathcal{A}\setminus\mathbb{J}} \boldsymbol{f}_k \cdot \boldsymbol{n} \, dA \tag{5.32}$$

$$= \int_\mathcal{A} \nabla \cdot \boldsymbol{f}_k \, dA \;-\; \int_{\partial\mathcal{A}\setminus\mathbb{J}} \boldsymbol{f}_k \cdot \boldsymbol{n} \, dA \tag{5.33}$$

$$= 0 \qquad\qquad -\int_{\partial\mathcal{A}\setminus\mathbb{J}} \boldsymbol{f}_k \cdot \boldsymbol{n} \, dA \tag{5.34}$$

$$\Rightarrow \int_\mathbb{J} \boldsymbol{f}_k \cdot \boldsymbol{n}_\mathbb{J} \, dA = -\int_{\partial\mathcal{K}} H(-\Phi) \, \boldsymbol{f}_k \cdot \boldsymbol{n} \, dA. \tag{5.35}$$

Formulation (5.35) has the advantage that we have transformed the integral over a *curved* surface into the integral over a plane surface $\partial\mathcal{A} \setminus \mathbb{J}$. Moreover, it can be interpreted as the *volume* integral of a discontinuous integrand over the *edges* of $\mathcal{K}$. Integrals of this type will be treated in the next level of recursion (cf. Section 5.5.1) that will be discussed in detail in Section 5.5.4. We will meanwhile assume that they can be evaluated accurately and efficiently.

In summary, the non-linear system (5.27) has been replaced by the larger but linear system

$$\begin{pmatrix} \boldsymbol{f}_1(\boldsymbol{x}_1) \cdot \boldsymbol{n}_\mathbb{J}(\boldsymbol{x}_1) & \dots & \boldsymbol{f}_1(\boldsymbol{x}_M) \cdot \boldsymbol{n}_\mathbb{J}(\boldsymbol{x}_M) \\ \vdots & \ddots & \vdots \\ \boldsymbol{f}_K(\boldsymbol{x}_1) \cdot \boldsymbol{n}_\mathbb{J}(\boldsymbol{x}_1) & \dots & \boldsymbol{f}_K(\boldsymbol{x}_M) \cdot \boldsymbol{n}_\mathbb{J}(\boldsymbol{x}_M) \end{pmatrix} \begin{pmatrix} w_1 \\ \vdots \\ w_M \end{pmatrix} = \begin{pmatrix} -\int\limits_{\partial\mathcal{A}\setminus\mathbb{J}} \boldsymbol{f}_1 \cdot \boldsymbol{n} \, dA \\ \vdots \\ -\int\limits_{\partial\mathcal{A}\setminus\mathbb{J}} \boldsymbol{f}_K \cdot \boldsymbol{n} \, dA \end{pmatrix} \tag{5.36}$$

that can be solved for the weights of the surface quadrature rule.

### 5.5.3.1   A note on the replacement of the basis functions

We emphasize that replacing the integrand in (5.32) introduces an analytical error because, in general, $\boldsymbol{f}_k \cdot \boldsymbol{n}_{\mathfrak{I}} \neq f_i \, \forall i$. Since this is the only non-numerical error present in the proposed approach, its performance directly depends on the question whether the functions in $\mathcal{F}$ can be represented or approximated by the functions in $\mathcal{F}'$. As a result, we will briefly address this issue using the example of a generic, two-dimensional element with the 2nd order monomial basis $\mathcal{F} = \{1, x, y, x^2, xy, y^2\}$ and the corresponding divergence-free basis presented in Appendix C.

To that end, consider a linear interface $\mathfrak{I}_1$ with normal vector

$$\boldsymbol{n}_{\mathfrak{I}} = \begin{pmatrix} \cos(\alpha) \\ \sin(\alpha) \end{pmatrix}, \quad \alpha \in [0, 2\pi], \tag{5.37}$$

intersecting $\mathcal{K}$. Inserting this into the definition $\mathcal{F}'$ results in

$$\begin{aligned} \mathcal{F}' = \{ \, &\cos(\alpha), \, \sin(\alpha), \, \sin(\alpha)\, x, \, \cos(\alpha)\, x - \sin(\alpha)\, y, \, \cos(\alpha)\, y, \, \cos(\alpha)\, y^2, \\ &2\cos(\alpha)\, xy - \sin(\alpha)\, y^2, \, \cos(\alpha)\, x^2 - 2\sin(\alpha)\, xy, \, \sin(\alpha)\, x^2 \}, \end{aligned} \tag{5.38}$$

which reveals the fact that $\mathcal{F}'$ is a *spanning set* of $\mathcal{P}_{\mathcal{K}}(2)$ for any fixed $\alpha$. In other words, we have constructed a set $\mathcal{F}'$ for which we can evaluate the right-hand side of (5.36) *exactly* and whose elements can be used to represent the functions in $\mathcal{F}$ *exactly*. A quadrature rule following from (5.36) will consequently integrate all elements of $\mathcal{F}$ as well as their linear combinations, i.e. all functions in $\mathcal{P}_{\mathcal{K}_i}(2)$, *exactly*.

This line of argument obviously generalizes to arbitrary dimensions and basis degrees $P$, from which we can see that the quadrature rules obtained by means of the presented approach are exacts in case of linear interfaces with constant normal vector field. There is, however, no straightforward extension of this statement to general non-linear interfaces, especially because $\boldsymbol{n}_{\mathfrak{I}}$ necessarily becomes non-polynomial if $\mathfrak{I}$ is curved. Still, the results of our numerical experiments suggest that the integration error decreases with a rate of $O(h^{P+1})$, hence indicating that $\mathcal{F}'$ is a reasonable *approximation* of a spanning set of $\mathcal{F}$. A more detailed analysis of this aspect will be subject of further research.

### 5.5.3.2   Frame of reference

In most computational methods, it is good practice to perform the numerical integration on a reference element $\mathcal{K}$ which can be mapped onto the physical domain of integration via bijective transformations $\boldsymbol{T} : \mathbb{R}^D \to \mathbb{R}^D$. This strategy is also crucial for the presented method because the divergence operator is *not* invariant under general transformations $\boldsymbol{T}$, which is why a divergence-free basis will generally be different for each physical element $\boldsymbol{T}(\mathcal{K})$. In addition to the implications of the more well-known transformation of volume integrals, it is essential to account for the rescaling of the

size of an infinitesimal surface element $dA$ when transferring surface integrals from the reference to the physical element, i.e.

$$\int_{\boldsymbol{T}(\mathbb{I})} d\tilde{A} = \int_{\mathbb{I}} \frac{\|\nabla_{\boldsymbol{x}}\varphi\|}{\|\nabla_{T(\boldsymbol{x})}\varphi\|} |\det(J(\boldsymbol{T}))|\, dA. \tag{5.39}$$

We therefore assemble and solve Equation (5.36) in the reference coordinate system and obtain the physical weights $\tilde{\boldsymbol{w}}$ via

$$\tilde{\boldsymbol{w}} = \frac{\|\nabla_{T(\boldsymbol{x})}\varphi\|}{\|\nabla_{\boldsymbol{x}}\varphi\|} \frac{\boldsymbol{w}}{|\det(J(\boldsymbol{T}))|}. \tag{5.40}$$

## 5.5.4   Volume integrals

In the next step, we consider volume integrals of the type

$$\int_{\mathcal{A}} g\, dV = \int_{\mathcal{K}} H(-\varphi)\, g\, dV. \tag{5.4, repeated}$$

Just as before, we assume that $g$ is not known explicitly which is why we have to use a quadrature rule based on the functions in $\mathcal{F}$.

### 5.5.4.1   Specification of the moment-fitting system

Due to the fact that the functions $f_i$ are known explicitly, it is straightforward to define suitable antiderivatives $\boldsymbol{f}_i$ such that $\nabla \cdot \boldsymbol{f}_i = f_i$ holds, e.g.

$$\boldsymbol{f}_i = \frac{1}{2}\begin{pmatrix} \int f_i\, dx \\ \int f_i\, dy \end{pmatrix} \quad \text{and} \quad \boldsymbol{f}_i = \frac{1}{3}\begin{pmatrix} \int f_i\, dx \\ \int f_i\, dy \\ \int f_i\, dz \end{pmatrix} \tag{5.41}$$

in two and three dimensions, respectively. Using Gauss' theorem once again, such a definition allows us to rewrite the volume integrals over the basis functions as

$$\int_{\mathcal{A}} f_i\, dV = \int_{\mathcal{A}} \nabla \cdot \boldsymbol{f}_i\, dV \tag{5.42}$$

$$= \int_{\partial\mathcal{A}} \boldsymbol{f}_i \cdot \boldsymbol{n}\, dA \tag{5.43}$$

$$= \int_{\mathbb{I}} \boldsymbol{f}_i \cdot \boldsymbol{n}_{\mathbb{I}}\, dA + \int_{\partial\mathcal{A}\backslash\mathbb{I}} \boldsymbol{f}_i \cdot \boldsymbol{n}\, dA. \tag{5.44}$$

Now, both integrals are defined on $D-1$-dimensional sub-manifolds and can be evaluated efficiently by means of the strategy depicted in Section 5.5.1.

Summing up, the non-linear system (5.27) reduces to the linear system

$$\begin{pmatrix} f_1(\boldsymbol{x}_1) & \dots & f_1(\boldsymbol{x}_M) \\ \vdots & \ddots & \vdots \\ f_N(\boldsymbol{x}_1) & \dots & f_N(\boldsymbol{x}_M) \end{pmatrix} \begin{pmatrix} w_1 \\ \vdots \\ w_M \end{pmatrix} = \begin{pmatrix} \int\limits_{\partial A} \boldsymbol{f}_1 \cdot \boldsymbol{n} \, dA \\ \vdots \\ \int\limits_{\partial A} \boldsymbol{f}_N \cdot \boldsymbol{n} \, dA \end{pmatrix}. \qquad (5.45)$$

### 5.5.4.2   A note on efficiency

It is important to note that this system contains the same number of moments as the original, non-linear system (5.27), which is why less nodes are required in the volume case compared to the surface case. Furthermore, the system matrix $\boldsymbol{A}$ is now completely independent of the level set function and, due to the fixation of the quadrature nodes, identical in each cell of a computational grid with equal topology. Consequently, its factorization only has to be computed *once* during the whole computation, which greatly improves the efficiency of the proposed scheme.

We also note that, even though more efficient choices than (5.41) exist for special cases (e.g., see Sudhakar & Wall (2013)), we stick with this formulation because it is generally applicable and easy to implement. The overall runtime of the proposed hierarchical algorithm is in any case dominated by the time required for the construction of the surface quadrature rules, which is why the additional performance penalty is negligible within the scope of this work. Still, one should keep in mind that one is free in the choice of the method for the computation of the right-hand side of (5.45). If the problem of interest admits a cheaper evaluation of the surface integrals, for example, it can be beneficial to consider alternative choices of $\boldsymbol{f}_i$ requiring less function evaluations (Abedian, Parvizian, Düster, Khademyzadeh & Rank (2013), Sudhakar & Wall (2013)).

## 5.6   Numerical experiments

Throughout this section, we present numerical results for test cases presented by Smereka (2006) (surface integrals) and Min & Gibou (2007) (volume integrals). Reported errors are relative errors and have been computed from the average over 100 random perturbations of the interface location. The tests using quadrilateral and the hexahedral cells have been performed on equidistant grids with uniform grid-spacing $h$. In case of triangular cells, unstructured grids with characteristic edge length $h$ have been used. The coarsest grids for each configuration are depicted in Figure 5.6. When reporting results obtained by means of a subdivision strategy (i.e., results obtained by Min & Gibou (2007) and using the adaptive strategy presented in Section 5.4), we consider the *effective* resolution $h$ based on the smallest sub-polytopes.

Timing results were obtained on a PC with a single 3.3 GHz Intel Core i5-2500 CPU. In the context of the adaptive quadrature, they include the time for the assembly of all required subdivision trees, the transformation of the quadrature rules and a

(a) Quadrilaterals (25 cells)     (b) Triangles (60 cells)     (c) Hexahedrons (125 cells)
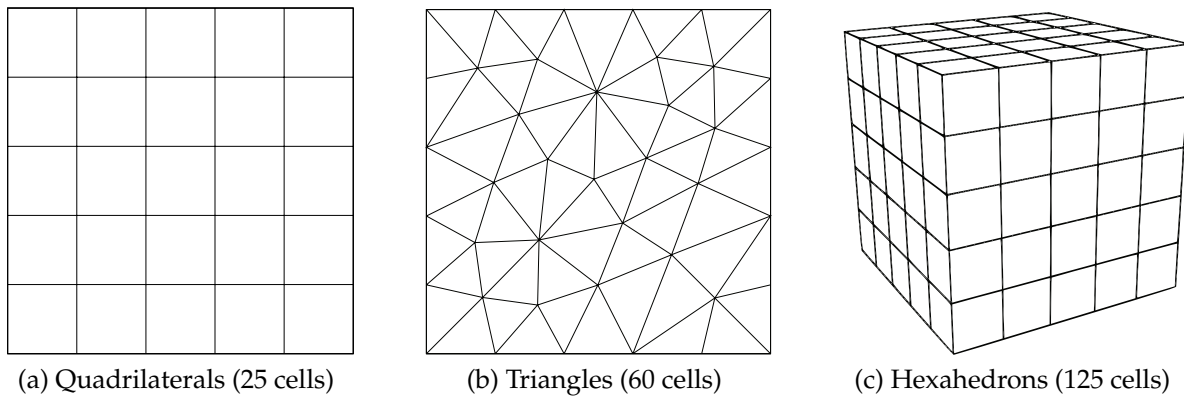
Figure 5.6: Coarsest grids ($h = 0.8$) for each type of grid element used in the numerical examples

single evaluation of the integral using the final quadrature rule. In the context of the moment-fitting approach, they include the time required for the construction of the full hierarchy of quadrature rules as well as a single evaluation of the integral using the final quadrature rule. In the latter case, the time for the construction of a quadrature rule dominates the actual execution time, which is why the efficiency is typically even higher in practical applications where multiple integrals are evaluated in the same configuration.

In the following discussion, we use the term *Adaptive* to indicate results that have been obtained using the tree-based, adaptive strategy presented in Section 5.4. Results obtained by means of the hierarchical moment-fitting (HMF) strategy presented in Section 5.5, on the other hand, will be denoted by HMF($P$), where the parameter $P$ indicates the maximal order of the basis functions that have been included in the moment-fitting basis. All relative computation times $t_\text{rel}$ have been normalized with respect to HMF(0). In the calculation of the EOC, values clearly deteriorated by the machine accuracy have been omitted. Affected convergence rates are marked with an asterisk.

In order to separate approximation from integration errors, all level set functions have been chosen such that they can be represented exactly by a basis of degree two. This is at variance with the definition of the test cases by Smereka (2006) and Min & Gibou (2007), and leads to the fact that the functions strongly violate the signed-distance property. Even though the modifications do not affect the zero iso-contour, this makes the test cases slightly more challenging.

Finally, we emphasize that the HMF results for the three-dimensional test cases stated below are more accurate than the results originally published by Müller et al. (2013). There are two major reasons for the these differences: Firstly, we have modified the recursive strategy (cf. Section 5.5.1) such that we increase the moment-fitting degree to $P + 1$ when integrating over the boundary of $\mathcal{K}$ (cf. Figure 5.5d). This is necessary since we transform the integral using Gauss theorem, and thus in order to restore the full convergence rate $O(h^{P+1})$ in the three-dimensional cases (in contrast to the

originally published rate of $O(h^P)$). Secondly, we have increased the robustness with respect to perturbations of the interface location by further increasing the number of quadrature nodes $M$ in the surface case (cf. Section 5.5.2). The presented three-dimensional results have been obtained with $M/K \approx 3$ for the surface case ($K$ being the size of the divergence-free basis), whereas we still use $M/N \approx 1$ in the volume case. Obviously, this severe increase in the size of the moment-fitting system entails a significant performance penalty, which is only justified if the accuracy requirements are comparatively high (that is, in the order of $10^{-8}$ or higher). In practical applications, it is thus recommended to account for this trade-off when selecting a factor $M/K > 1$.

## 5.6.1 Quadratic integrand on a circle

The first test case is the line integral

$$\int_{\mathcal{I}} (3x^2 - y^2)\, dA = 2\pi \tag{5.46}$$

on the unit circle with the level set function $\varphi(x, y) = x^2 + y^2 - 1$.

Table 5.1 summarizes the results for this case in a format that allows for an easy comparison with results reported in literature. Here, we see that the error obtained using the adaptive strategy is in the same order of magnitude as the errors obtained by Smereka (2006) using an approximation of the delta function by means of Green's functions. The results corresponding to the presented HMF strategy, on the other hand, are significantly smaller for moderate values $P$, despite a much coarser resolution. Furthermore, it can be observed that, independent of the element type, the errors decrease rapidly with an increasing order of the moments. At the same time, the measured computational effort only grows moderately with increasing $P$.

Figures 5.7 and 5.8 visualize the output of the proposed algorithms using the example of an equidistant grid with a spacing of $h = 0.4$. The illustration of the adaptive strategy (Figure 5.7) assumes that the surface integral is computed from the adaptive subdivision of $\mathcal{A}$ using a maximum of three recursion levels, and a quadrature rule of degree 1 in all leaves of the subdivision tree. In the case of the HMF strategy (Figure 5.8), on the other hand, we have used a basis of degree $P = 2$ and distinguished between the quadrature rules for the surface and the volume case. Even though the volume quadrature rule is not required for the evaluation of (5.46), it is worthwhile to explore the differences in the final weight distribution. The largest weights in the surface case are associated with the nodes closest to the zero iso-contour of the level set, just as it would be the case for a regularized delta distribution. A similar situation can be observed in the corresponding volume case, where the better part of the accumulated weight is concentrated on the sub-domain $\mathcal{A}$, thus resembling the behaviour of a regularized Heaviside function. In the direct comparison between the illustrations, it becomes clearly evident that the adaptive strategy requires substantially more point evaluations, even though the HMF approach achieves a lower overall error.
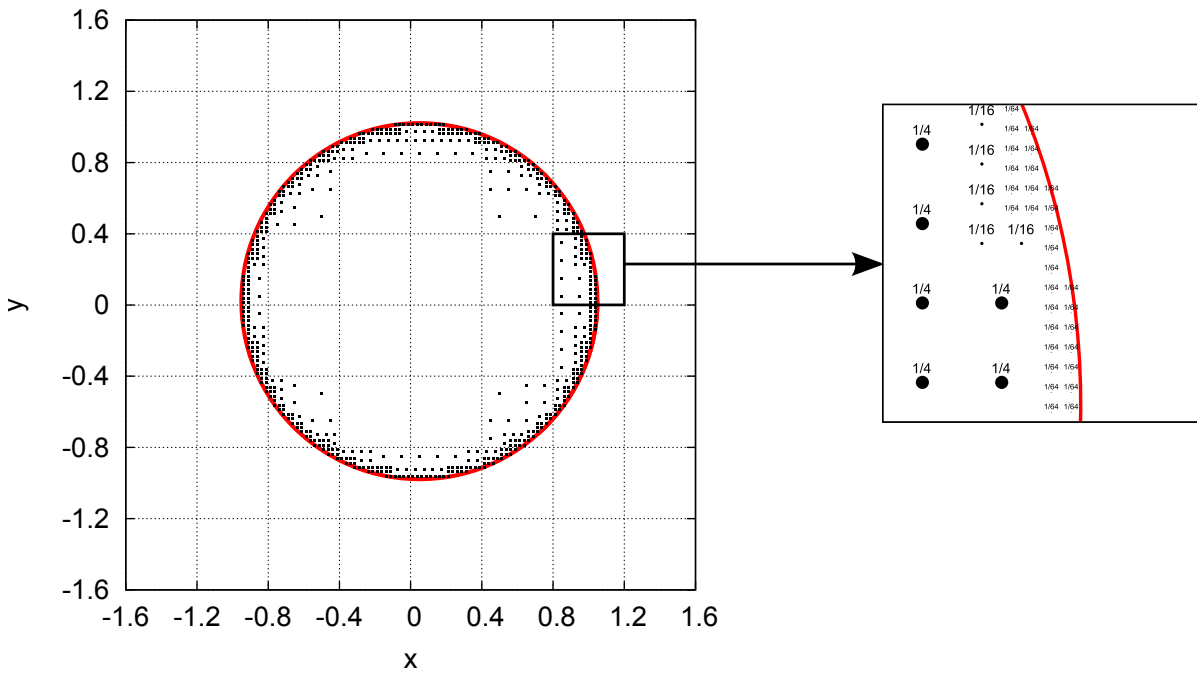
Figure 5.7: Quadrature rules for the integration over a circle (red line) using the adaptive strategy with three subdivision levels. Left part: Location of quadrature nodes (Black squares). Right part: Visualization of the absolute values of the weights in a selected cell in the reference configuration
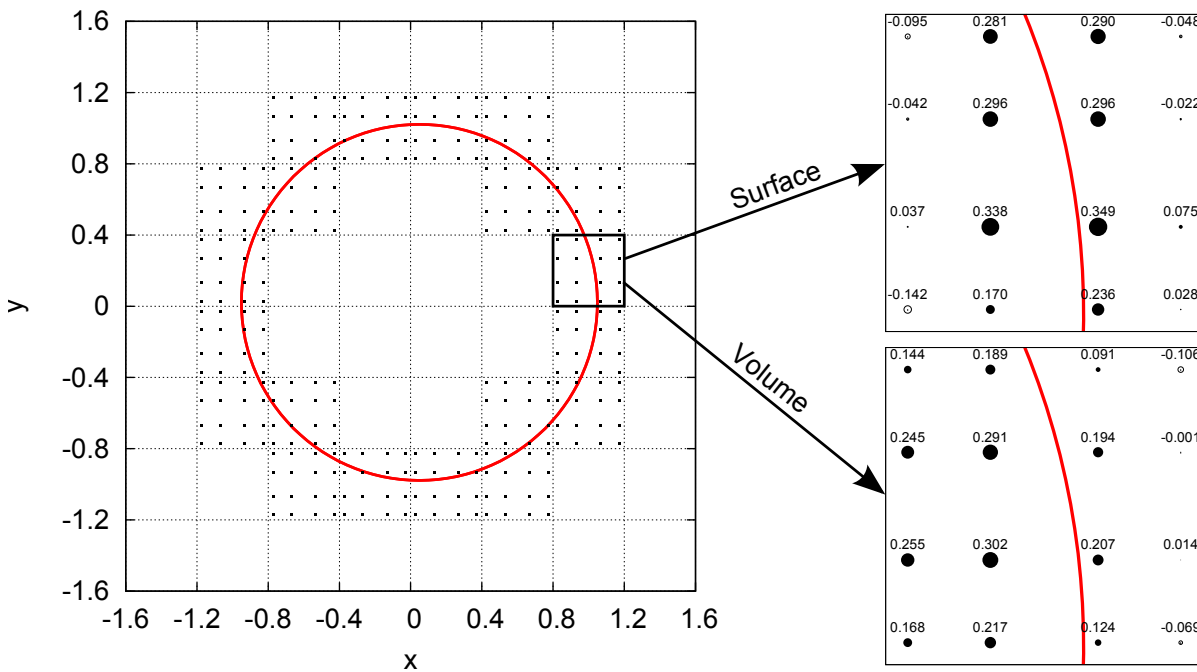


Figure 5.8: Quadrature rules for the integration over a circle (red line) using HMF(2), i.e., the moment-fitting strategy with a 2nd order basis. Left part: Location of quadrature nodes (Black squares). Right part: Visualization of the absolute values of the weights (Filled circle: positive weight; empty circle: negative weight) in a selected cell in the reference configuration

| Method | h | Quadrilaterals | | Triangles | |
|--------|---|------|------|------|------|
| | | Error | $t_{\text{rel}}$ | Error | $t_{\text{rel}}$ |
| Smereka | $0.4 \cdot 2^{-6}$ | 1.22e-05 | - | - | - |
| Adaptive | $0.4 \cdot 2^{-6}$ | 5.47e-05 | 15.6 | 4.57e-05 | 20.4 |
| HMF(0) | 0.4 | 8.72e-02 | 1.0 | 3.70e-02 | 1.0 |
| HMF(1) | 0.4 | 1.62e-02 | 1.1 | 5.58e-03 | 1.0 |
| HMF(2) | 0.4 | 9.23e-06 | 1.1 | 1.00e-06 | 1.1 |
| HMF(3) | 0.4 | 4.93e-06 | 1.2 | 3.47e-07 | 1.1 |
| HMF(4) | 0.4 | 5.11e-07 | 1.3 | 1.71e-08 | 1.3 |

Table 5.1: Results for the evaluation of a line integral on a circle



| Method | EOC |
|--------|-----|
| Smereka | 2.00 |
| Adaptive | 1.49 |
| HMF(0) | 1.13 |
| HMF(1) | 2.01 |
| HMF(2) | 4.77 |
| HMF(3) | 4.69 |
| HMF(4) | 5.76 |
| HMF(5) | 6.87 |
| HMF(6) | 7.92 |
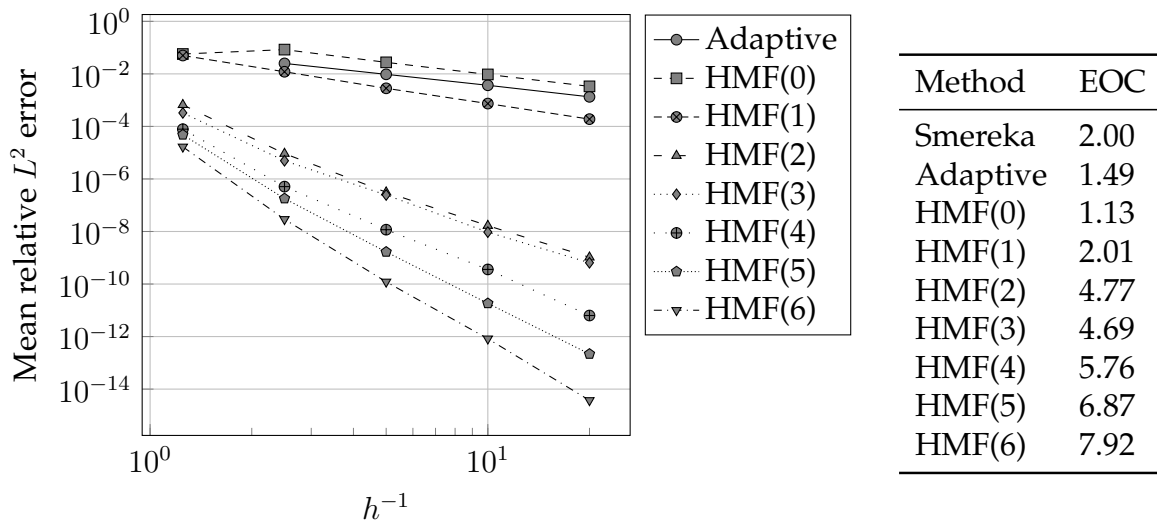
Figure 5.9: Study of the $h$-convergence for the evaluation of a line integral on a circle using quadrilateral elements

Noting that the example has been chosen such that both cases require approximately the same computational effort, this underlines the principal advantages of the HMF method in comparison with general subdivision based methods.

The above-noted trend is elaborated in more detail in the $h$-convergence studies depicted in Figures 5.9 (quadrilaterals) and 5.10 (triangles). The measured EOC for the adaptive approach is around $1.5$ in both cases and only outperforms HMF(0) in terms of accuracy on a fixed grid. In case of the HMF strategy, the EOC is remarkably high in all cases, and the results suggest a lower bound in the order of $h^{P+1}$. To the best of our knowledge, similar convergence rates have only been observed using higher order interface reconstructions (Cheng & Fries 2010).

| Method | EOC |
|--------|------|
| Adaptive | 1.47 |
| HMF(0) | 1.64 |
| HMF(1) | 1.86 |
| HMF(2) | 4.34 |
| HMF(3) | 4.75 |
| HMF(4) | 5.54 |
| HMF(5) | 6.65 |
| HMF(6) | 7.28 |
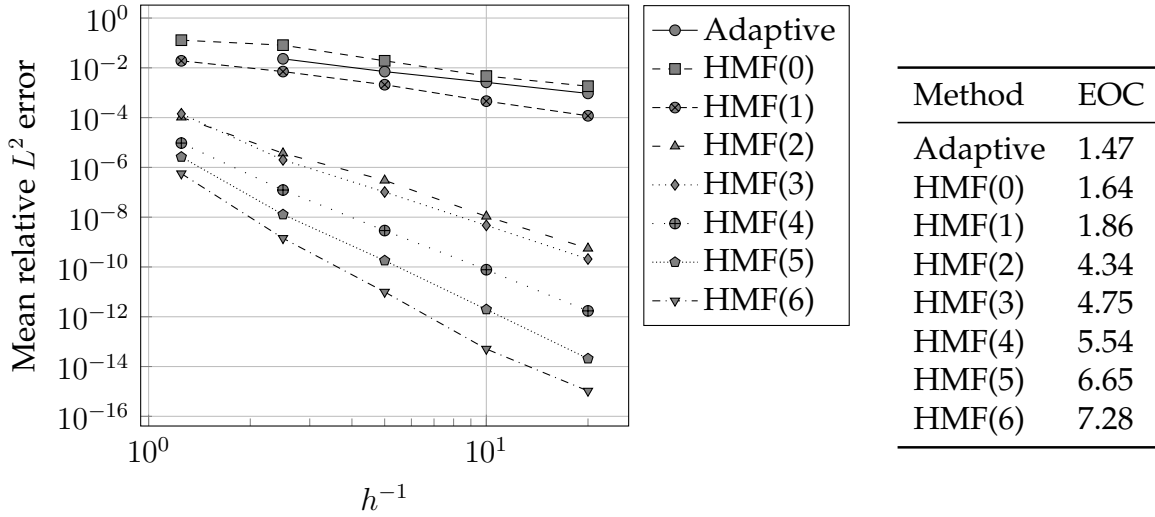
Figure 5.10: Study of the $h$-convergence for the evaluation of a line integral on a circle using triangular elements

| | | Quadrilaterals | | Triangles | |
|--------|--------|-------|-------------|-------|-------------|
| Method | $h$ | Error | $t_{\text{rel}}$ | Error | $t_{\text{rel}}$ |
| Min & Gibou | $0.4 \cdot 2^{-6}$ | 1.46e-05 | - | - | - |
| Adaptive | $0.4 \cdot 2^{-6}$ | 9.08e-05 | 3.4 | 4.50e-05 | 4.0 |
| HMF(0) | 0.4 | 4.96e-03 | 1.0 | 2.38e-03 | 1.0 |
| HMF(1) | 0.4 | 2.21e-04 | 1.0 | 2.62e-05 | 1.0 |
| HMF(2) | 0.4 | 1.60e-05 | 1.1 | 2.94e-06 | 1.1 |
| HMF(3) | 0.4 | 2.78e-06 | 1.2 | 1.44e-07 | 1.2 |
| HMF(4) | 0.4 | 3.98e-07 | 1.4 | 1.58e-08 | 1.3 |

Table 5.2: Results for the calculation of the area of an ellipse

## 5.6.2 Area and arc-length of an ellipse

In the next test case, we consider the area and the arc-length of an ellipse with the level set function

$$\Phi(x, y) = \left(\frac{x}{1.5}\right)^2 + \left(\frac{y}{0.75}\right)^2 - 1. \tag{5.47}$$

The respective reference solutions are given by

$$\int_{\mathcal{A}} 1 \, dV = \frac{9}{8}\pi \tag{5.48}$$

and

$$\int_{\mathcal{J}} 1 \, dA \approx 7.26633616541076. \tag{5.49}$$

| Method | EOC |
|--------|------|
| Min | 2.02 |
| Adaptive | 1.52 |
| HMF(0) | 1.85 |
| HMF(1) | 3.84 |
| HMF(2) | 4.59 |
| HMF(3) | 5.72 |
| HMF(4) | 6.64 |
| HMF(5) | 7.29 |
| HMF(6) | 8.88* |
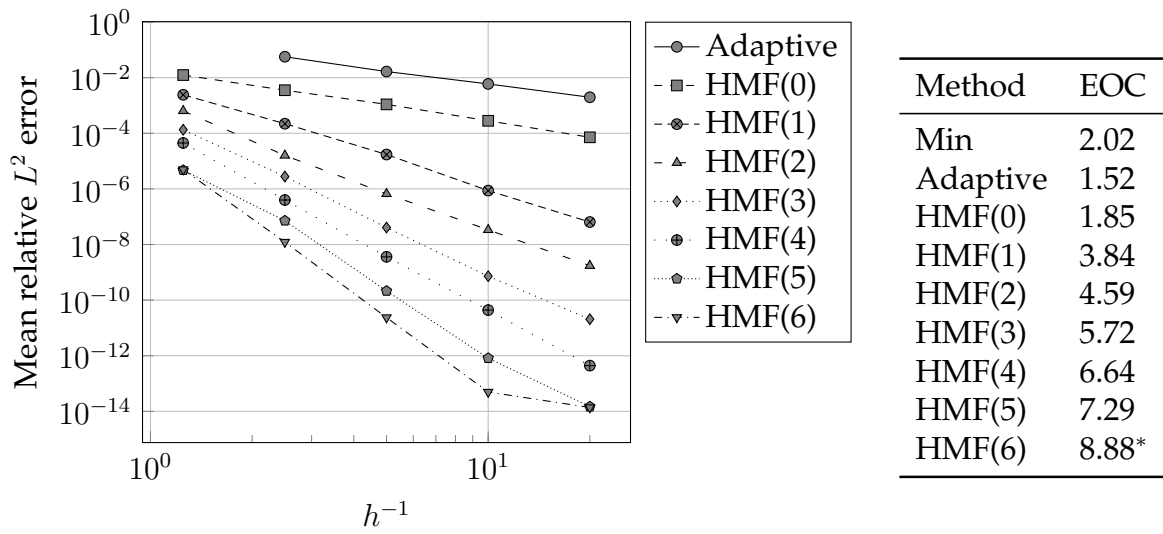
Figure 5.11: Study of the $h$-convergence for the calculation of the area of an ellipse using quadrilateral elements



| Method | EOC |
|--------|------|
| Adaptive | 1.54 |
| HMF(0) | 1.80 |
| HMF(1) | 3.44 |
| HMF(2) | 4.46 |
| HMF(3) | 5.39 |
| HMF(4) | 6.33 |
| HMF(5) | 6.84 |
| HMF(6) | 8.16* |

Figure 5.12: Study of the $h$-convergence for the calculation of the area of an ellipse using triangular elements

| Method | h | Quadrilaterals | | Triangles | |
|--------|---|-------|-----------|-------|-----------|
|        |   | Error | $t_{\rm rel}$ | Error | $t_{\rm rel}$ |
| Min | $0.4 \cdot 2^{-6}$ | 4.90e-06 | - | - | - |
| Smereka | $0.4 \cdot 2^{-6}$ | 1.89e-06 | - | - | - |
| Adaptive | $0.4 \cdot 2^{-6}$ | 9.04e-06 | 12.5 | 5.05e-06 | 17.0 |
| HMF(0) | 0.4 | 1.55e-03 | 1.0 | 6.66e-04 | 1.0 |
| HMF(1) | 0.4 | 1.51e-03 | 1.0 | 8.02e-04 | 1.0 |
| HMF(2) | 0.4 | 2.29e-04 | 1.1 | 1.57e-05 | 1.0 |
| HMF(3) | 0.4 | 1.95e-05 | 1.1 | 3.24e-06 | 1.2 |
| HMF(4) | 0.4 | 7.03e-06 | 1.3 | 2.58e-07 | 1.3 |

Table 5.3: Results for the calculation of the arc-length of an ellipse

Results for the volume case are given in Table 5.2. Just as in the previous case, the measured errors for the adaptive strategy are only lower than those for the HMF method for low orders of the moment-fitting basis. This is due to the fact that the errors for the HMF method on the coarsest grid decrease dramatically as $P$ is increased. The corresponding $h$-convergence studies (Figures 5.11 and 5.12) confirm that the high values for the EOC can also be obtained for the volume integration. The resolution on the coarsest triangular meshes, however, seems to lie outside of the asymptotic regime. In order to avoid an *overestimation* of the EOC, we have omitted the corresponding values in the evaluation.

The results for the corresponding surface case are summarized in Table 5.3. Once more, we see that the errors based on the HMF approach strongly decrease as the order of the moments is increased. At the same time, the adaptive method does not perform as good as the methods proposed by Min & Gibou (2007) and Smereka (2006), at least in terms of the integration error for a given resolution. The corresponding convergence results are analogous to the findings reported above, which is why we study the computational efficiency in this case instead (Figures 5.13 and 5.14). Here, it is clearly visible that the adaptive strategy can only compete with the HMF strategy using low orders. This finding can mainly be attributed to two aspects: Firstly, a relatively large number of evaluations of the level set function is required for the construction of the subdivision tree. Secondly, the fact that the number of nodes as well as their location is different in every intersected cell prohibits the exploitation of essential optimizations as, for instance, the use of highly efficient Basic Linear Algebra Subprograms (BLAS) sub-routines. Furthermore, it can be observed that, for a given error level which is suitable for a particular application, moderate orders of the moment-fitting basis ($2 \leq P \leq 3$) are most efficient in case of low accuracy requirements, and that higher orders gradually pay off if the requirements are increased.

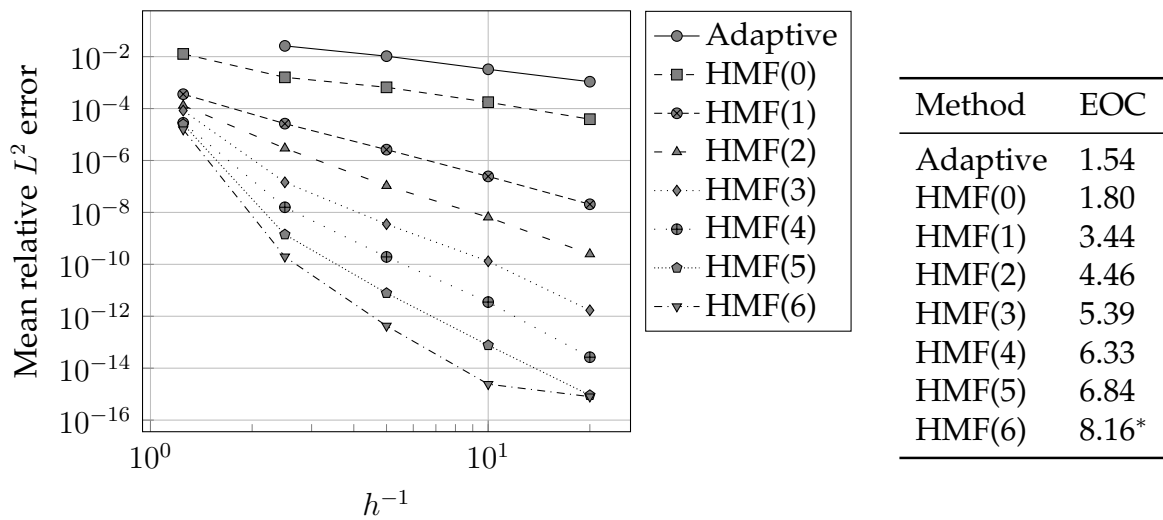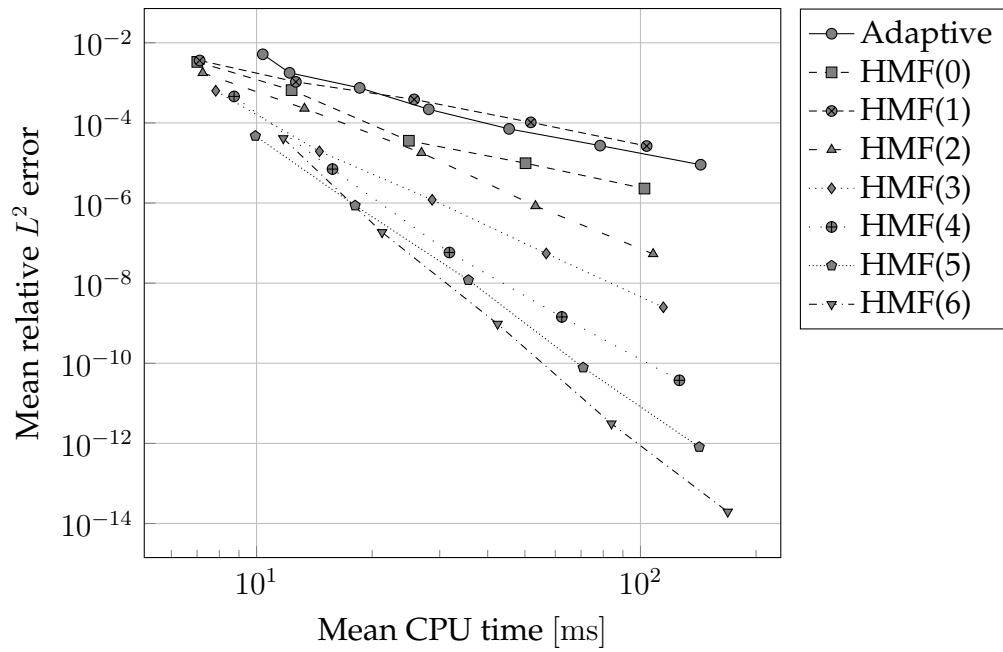Figure 5.13: Study of the error as a function of the mean CPU time for the calculation of the arc-length of an ellipse using quadrilateral elements
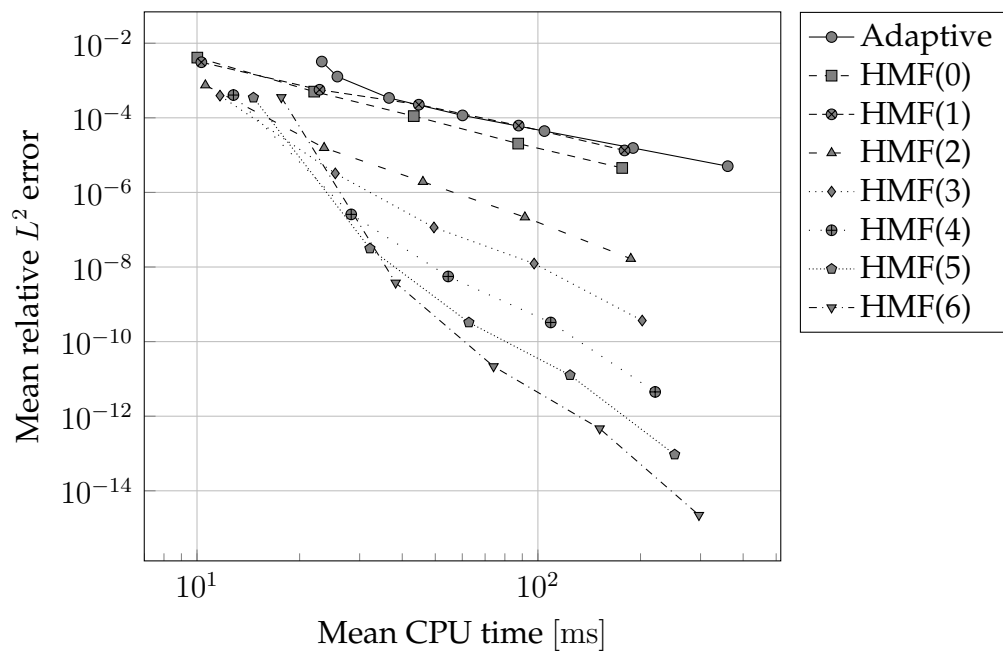


Figure 5.14: Study of the error as a function of the mean CPU time for the calculation of the arc-length of an ellipse using triangular elements

|         |                   | Hexahedrons |             |
|---------|-------------------|-------------|-------------|
| Method  | h                 | Error       | $t_{\text{rel}}$ |
| Smereka  | $0.4 \cdot 2^{-5}$ | 8.42e-06 | -   |
| Adaptive | $0.4 \cdot 2^{-5}$ | 5.47e-06 | 8.9 |
| HMF(0)   | $0.4 \cdot 2^{-1}$ | 4.39e-03 | 1.0 |
| HMF(1)   | $0.4 \cdot 2^{-1}$ | 2.82e-05 | 1.2 |
| HMF(2)   | $0.4 \cdot 2^{-1}$ | 9.70e-07 | 1.5 |
| HMF(3)   | $0.4 \cdot 2^{-1}$ | 4.78e-07 | 2.2 |
| HMF(4)   | $0.4 \cdot 2^{-1}$ | 5.62e-08 | 3.6 |

Table 5.4: Results for the evaluation of a surface integral on a sphere



| Method   | EOC  |
|----------|------|
| Smereka  | 2.50 |
| Adaptive | 1.86 |
| HMF(0)   | 1.97 |
| HMF(1)   | 3.69 |
| HMF(2)   | 4.99 |
| HMF(3)   | 4.67 |
| HMF(4)   | 6.45 |
| HMF(5)   | 8.29 |
| HMF(6)   | 9.19 |
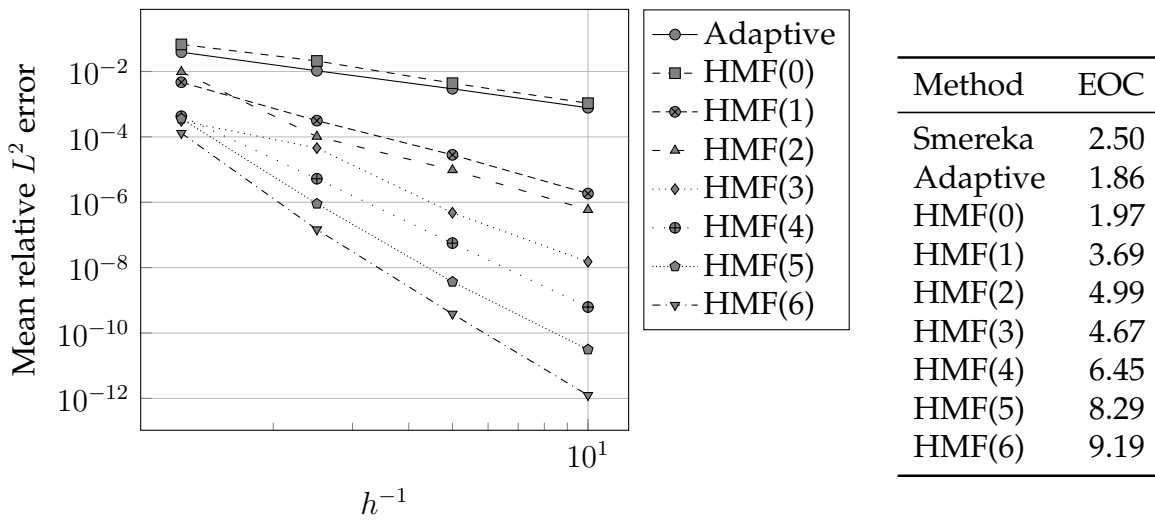
Figure 5.15: Study of the $h$-convergence for the calculation of a quadratic integrand on a sphere using hexahedral elements

### 5.6.3 Quadratic integrand on a sphere

The first three-dimensional test case is given by the surface integral

$$\int_{\mathfrak{I}} (4 - 3x^2 + 2y^2 - z^2) \, dA = \frac{40}{3}\pi \tag{5.50}$$

on the unit sphere with the corresponding level set function $\Phi(x, y, z) = x^2 + y^2 + z^2 - 1$.

The results in Table 5.4 demonstrate that the basic findings from the corresponding two-dimensional case generalize to three dimensions. It should be noted, however, that the relative runtime of the HMF approach now increases faster as $P$ is increased. This finding can clearly be attributed to the higher number of basis functions for a given order $P$ of the moment-fitting basis (see Appendix C). In contrast to the corresponding two-dimensional test case, the adaptive integration scheme performs slightly better than the method proposed by Smereka (2006) for the given resolution. Figure 5.15

| | | Hexahedrons | |
|---|---|---|---|
| Method | h | Error | $t_{\mathrm{rel}}$ |
| Min | $0.4 \cdot 2^{-5}$ | 5.31e-05 | - |
| Adaptive | $0.4 \cdot 2^{-5}$ | 7.62e-05 | 1.9 |
| HMF(0) | $0.4 \cdot 2^{-1}$ | 1.46e-03 | 1.0 |
| HMF(1) | $0.4 \cdot 2^{-1}$ | 8.32e-06 | 1.1 |
| HMF(2) | $0.4 \cdot 2^{-1}$ | 8.56e-07 | 1.4 |
| HMF(3) | $0.4 \cdot 2^{-1}$ | 1.58e-07 | 2.0 |
| HMF(4) | $0.4 \cdot 2^{-1}$ | 2.80e-07 | 2.8 |

Table 5.5: Results for the calculation of the volume of an ellipsoid

shows the $h$-convergence results on hexahedral elements. Just as in the analogous two-dimensional case, the EOC exceeds $h^{P+1}$.

## 5.6.4 Volume and surface area of an ellipsoid

The last test case is concerned with the calculation of the volume and the surface area of an ellipsoid represented by the level set function

$$\Phi(x, y, z) = \left(\frac{x}{1.5}\right)^2 + \left(\frac{y}{0.75}\right)^2 + \left(\frac{z}{0.5}\right)^2 - 1. \tag{5.51}$$

The reference solutions are given by

$$\int_{A} 1 \, dV = \frac{3}{4}\pi \tag{5.52}$$

and

$$\int_{\mathcal{J}} 1 \, dA \approx 9.90182151329315, \tag{5.53}$$

respectively.

The results for the volume case (see Table 5.5) show once again that the HMF yields good results on relatively coarse grids where complicated intersections occur regularly. Regarding computational effort, however, the adaptive strategy is much more competitive in the three-dimensional case than it is in the two-dimensional case. The corresponding $h$-convergence study (see Figure 5.16) is consistent with previous observations and underlines the fact that the method is able to cope with the regions of strong curvature at the tips of the ellipsoid if the resolution is sufficiently fine (e.g., $h \leq 0.4$ in the given configuration). As a consequence, we have omitted the coarsest resolution in the calculation of the EOC in order to avoid an overestimation.

Finally, the results for the surface case are summarized in Table 5.6. We observe once more that the results for adaptive strategy are much closer to the results for HMF

| Method | EOC |
|---|---|
| Min | 2.00 |
| Adaptive | 1.92 |
| HMF(0) | 1.39 |
| HMF(1) | 4.77 |
| HMF(2) | 5.60 |
| HMF(3) | 6.95 |
| HMF(4) | 7.15 |
| HMF(5) | 8.62 |
| HMF(6) | 8.96 |
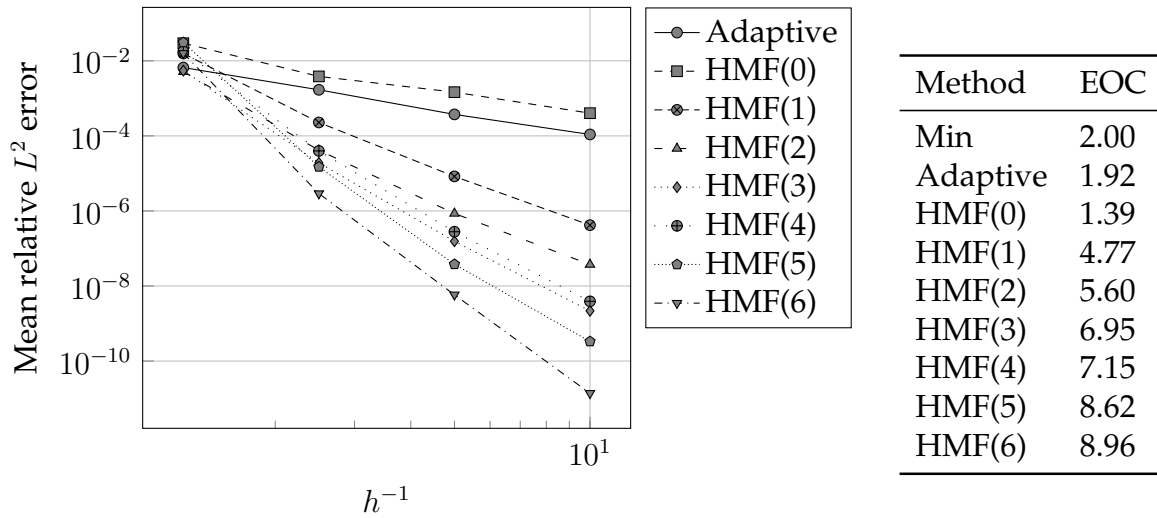
Figure 5.16: Study of the $h$-convergence for the calculation of the volume of an ellipsoid using hexahedral elements

| Method | h | Hexahedrons | |
|---|---|---|---|
| | | Error | $t_{\text{rel}}$ |
| Min | $0.4 \cdot 2^{-4}$ | 4.94e-04 | - |
| Smereka | $0.4 \cdot 2^{-5}$ | 9.30e-06 | - |
| Adaptive | $0.4 \cdot 2^{-5}$ | 7.49e-06 | 5.4 |
| HMF(0) | $0.4 \cdot 2^{-1}$ | 1.70e-03 | 1.0 |
| HMF(1) | $0.4 \cdot 2^{-1}$ | 8.89e-06 | 1.2 |
| HMF(2) | $0.4 \cdot 2^{-1}$ | 5.15e-06 | 1.5 |
| HMF(3) | $0.4 \cdot 2^{-1}$ | 7.20e-07 | 2.2 |
| HMF(4) | $0.4 \cdot 2^{-1}$ | 1.07e-07 | 3.6 |

Table 5.6: Results for the calculation of the surface area of an ellipsoid
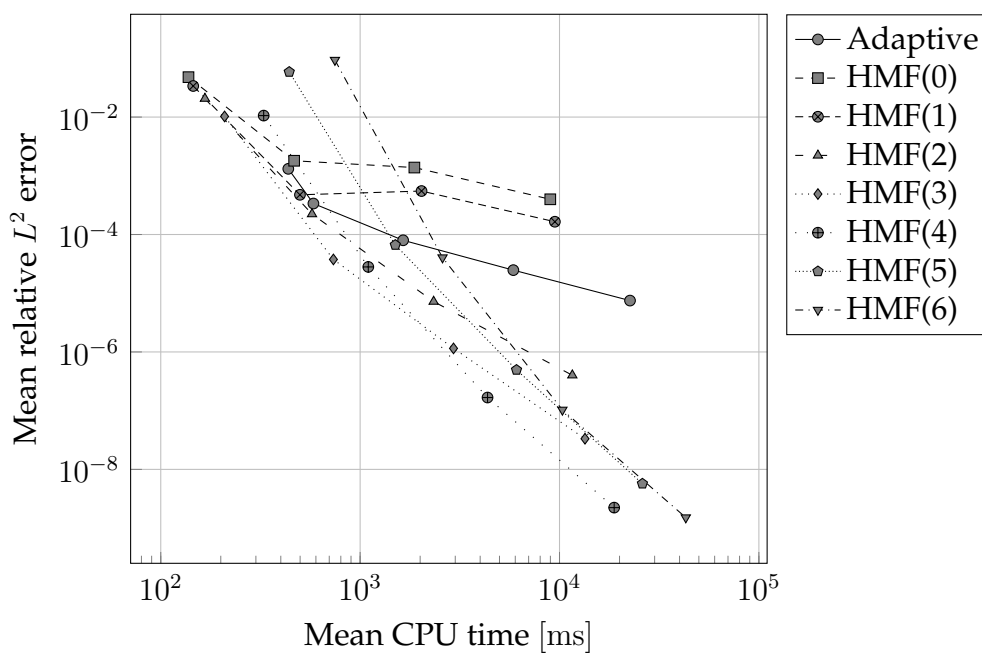
Figure 5.17: Study of the error as a function of the mean CPU time required for the calculation of the surface area of an ellipsoid using hexahedral elements with $M/K \approx 1.6$
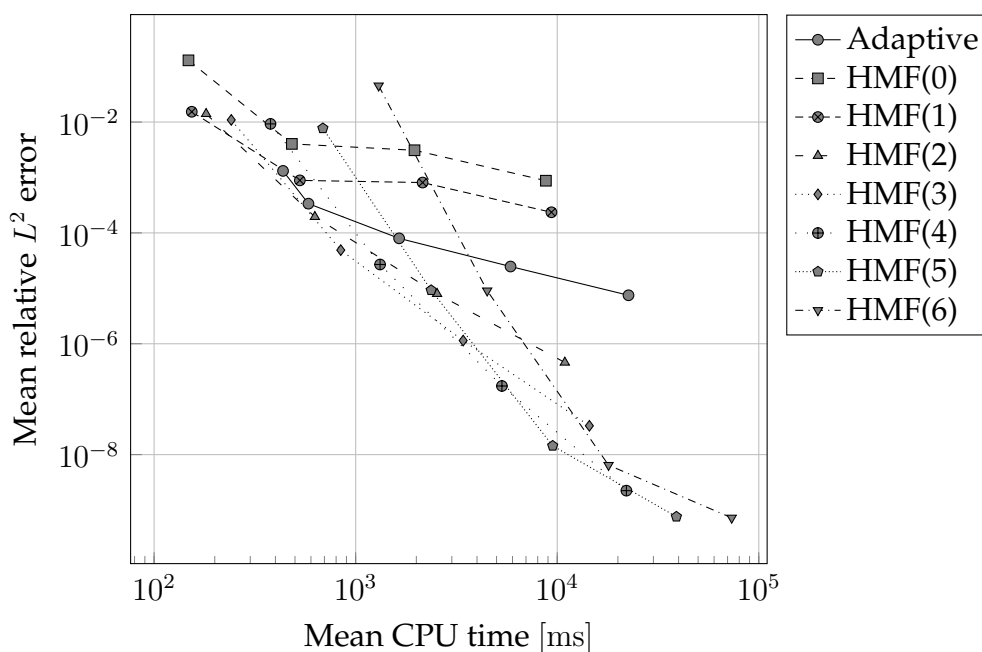


Figure 5.18: Study of the error as a function of the mean CPU time required for the calculation of the surface area of an ellipsoid using hexahedral elements with $M/K \approx 3.0$

strategy than in the two-dimensional examples. Since the general findings with respect to the observed convergence rates are very similar to the volume case, we study the computational efficiency in this configuration instead. In Figure 5.17 and Figure 5.18, we compare two different settings for the number of integrations nodes $M$ for a given number of basis functions $K$. The results for the original setting used by Müller et al. (2013) are given in Figure 5.17, whereas Figure 5.18 corresponds to the significantly increased number of integration points mentioned in the beginning of this section. In this direct comparison, we note a faster decrease of the integration error under grid refinement in the latter case, along with a relatively strong impact of the increased number of integration points on the runtime. Moreover, we observe a lower bound for the integration error in the order of $7 \cdot 10^{-10}$ which we did not observe in the previous test cases.

### 5.6.5 Discussion of the results

The results of the numerical experiments presented in the previous sections indicate that the adaptive integration strategy depicted in Section 5.4 compares well with existing methods, especially in three-dimensional cases. Its main appeal compared to the practice of linear interface reconstruction (e.g., see (Min & Gibou 2007)) is due to its simplicity that renders it virtually independent of geometrical issues related to the chosen element type.

The HMF quadrature (cf. Section 5.5), on the other hand, requires only very coarse grids and outperforms existing methods by several orders of magnitude in terms of accuracy. This finding also holds for the computational efficiency in two-dimensional cases, whereas the advantage is less distinctive in the three-dimensional configurations. Here, the larger number of quadrature nodes as well as the necessity to construct *multiple* quadrature rules per cell attenuates the advantage of the higher-order convergence of the integration error to some extent. Nonetheless, we emphasize that the presented concept is significantly simpler than a higher-order interface reconstruction on general polytopes $\mathcal{K}$, most prominently because no case-by-case analysis of the actual interface geometry is required. The focus of our further research in this context will consequently lie on finding practical estimates for the optimal choice of the number of integration points and the order of the moment-fitting system in a given configuration.

# 6 Conclusion

The conclusion of this thesis is subdivided into two parts. In the first part, we summarize the individual results that have been obtained in the previous chapters. Furthermore, we emphasize that the considered methods, implementations and results are prospective building blocks for a broad class of advanced applications. We will thus give a brief outlook on potential application scenarios in the second part of this chapter, including first results for a simple IBM based on the RKDGM presented in Chapter 4 and the moment-fitting quadrature presented in Section 5.5.

## 6.1  Summary

In this thesis, we have been concerned with different aspects of the numerical simulation of inviscid, compressible flows of different types of fluids using a DGM. In Chapter 2, we have presented useful properties of variations of the ideal gas EOS, namely the stiffened gas EOS, Tait's EOS and the covolume gas EOS. These properties have been exploited in Chapter 3 in order to extend two well-known analytical solutions for ideal gases, namely the isentropic vortex flow and Ringleb's solution, to these more general EOS. In case of the isentropic vortex solution, we have additionally shown how the individual single-phase test cases can be combined into a set of non-trivial multi-phase test cases. To the best of our knowledge, similar solutions have not been reported in literature and may hence serve as a helpful tool for the verification of numerical methods for non-standard EOS.

Subsequently, we have introduced a RKDGM for the numerical simulation of the corresponding PDEs. This scheme has been implemented during the course of this thesis by making use of the BoSSS Discontinuous Galerkin library. The verification results for the above-mentioned test cases (Chapter 4) indicate that the implemented scheme is generally suitable for the numerical simulation of the Euler equations with variable EOS.

The second part of this thesis deals with the numerical integration of non-smooth functions. In Chapter 5, we have thus presented two novel approaches for the numerical integration over surfaces and volumes that are at least partly defined on behalf of the zero iso-contour of a level set function. The first method (see Section 5.4) makes use of a simple, adaptive approach. Despite its simplicity, our numerical experiments suggest that it performs well on generic element types and is competitive with existing, more complicated approaches. The second method presented in Section 5.5, on the other hand, is based on the solution of a simplified moment-fitting system of arbitrary order $P$. Even though this approach has been designed such that a cumbersome, $P$-th order

reconstruction of the interface can be avoided, our numerical experiments suggest that the same rate of convergence of the integration error ($O(h^{P+1})$) can be obtained using HMF($P$).

## 6.2 Outlook

Several authors have demonstrated that methods like the XFEM (Chessa & Belytschko (2003b), Chessa & Belytschko (2003a), Moës, Béchet & Tourbier (2006), Fries (2009), van der Bos & Gravemeier (2009), Gross & Reusken (2011), Rasthofer, Henke, Wall & Gravemeier (2011), Sauerland & Fries (2011), Lehrenfeld & Reusken (2013)) and extensions of the DGM (Heimann, Engwer, Ippisch & Bastian (2013), Kummer & Oberlack (2013)) are well-suited for the numerical simulation of flows with immersed interfaces because they allow for the realization of arbitrary discretization orders, even in the presence of the inherent kinks and jumps of fluid properties at the interface. We have already argued that their efficiency heavily relies on the performance of the numerical integration (cf. Chapter 5), which is why we consider the presented HMF quadrature as the main result of this thesis.

In this context, we will now briefly sketch the principle ideas and some preliminary results for the model case of the extension of the numerical scheme introduced in Chapter 4 to flows with fixed immersed boundaries. Two major advantages of an IBM in comparison to boundary-fitted approaches are given by the simplification of the mesh generation and the spatial discretization in the case of curved domain boundaries. On the other hand, the IBM also implies that the boundary cells of the background mesh may be cut arbitrarily by the interface, which is why one has to be able to evaluate the discrete operators in rather complicated domains.

### 6.2.1 An RKDGM for domains with immersed boundaries

Given a representation of an immersed boundary in the form of a level set function $\varphi$, a natural extension of the RKDGM can be formulated starting from the discrete weak formulation of a scalar conservation law in a cell $\mathcal{K}_i$, i.e.

$$\int_{\mathcal{K}_i} \frac{\partial c}{\partial t} \Phi_{i,j} \, dV + \int_{\partial \mathcal{K}_i} (\boldsymbol{f}(c) \cdot \boldsymbol{n}) \, \Phi_{i,j} \, dA - \int_{\mathcal{K}_i} \boldsymbol{f}(c) \cdot \nabla \Phi_{i,j} \, dV = 0. \qquad \text{(4.2, repeated)}$$

Hereafter, we restrict the *physical* problem domain to the sub-domain associated with negative level set values. The domains of integration in cell $\mathcal{K}_i$ are thus replaced by the sub-domains $\mathcal{A}_i = \{\boldsymbol{x} \in \mathcal{K}_i : \varphi(\boldsymbol{x}) < 0\}$ and $\partial \mathcal{A}_i$, respectively. Taking into account that the surface $\partial \mathcal{A}_i$ consists of the edges $\{\mathcal{E}_{i,e}^{\mathcal{A}}\}_{e=1,\ldots,E_i} = \{\mathcal{E}_{i,e} \cap \overline{\mathcal{A}}_i\}_{e=1,\ldots,E_i}$ and the

interface $\mathfrak{I}_i = \{\boldsymbol{x} \in \mathcal{K}_i : \varphi(\boldsymbol{x}) = 0\}$, it follows that the discrete weak formulation in the context of an IBM can be written as

$$
\int\limits_{\mathcal{A}_i} \frac{\partial c}{\partial t} \Phi_{i,j} \, dV + \sum_{e=1}^{E_i} \int\limits_{\mathcal{E}_{i,e}^{\mathcal{A}}} \left( \boldsymbol{f}(c) \cdot \boldsymbol{n} \right) \Phi_{i,j} \, dA
$$
$$
+ \int\limits_{\mathfrak{I}_i} \left( \boldsymbol{f}(c) \cdot \boldsymbol{n}_{\mathfrak{I}} \right) \Phi_{i,j} \, dA - \int\limits_{\mathcal{A}_i} \boldsymbol{f}(c) \cdot \nabla \Phi_{i,j} \, dV = 0, \tag{6.1}
$$

where $\boldsymbol{n}_{\mathfrak{I}} = \nabla \varphi / \|\nabla \varphi\|$.

Regarding the introduction of the modal approximation (4.5), the additional integral over $\mathfrak{I}_i$ in Equation (6.1) is treated in the same way as the integrals over $\mathcal{E}_{i,e}^{\mathcal{A}}$, namely by resorting to a numerical flux function $f(c^-, c^+, \boldsymbol{n})$ that resolves the ambiguity in the integrand in a consistent manner. We note that we will again apply the Rusanov flux outlined in Section (4.2.1) in the following. Moreover, the value of $c^+$ on $\mathfrak{I}$ will evidently be prescribed according to the boundary condition imposed on the interface.

All in all, the modified system of ODEs following from Equation (6.1) can be summarized as

$$
\frac{\partial \boldsymbol{c}_i}{\partial t} + \underline{\boldsymbol{M}}_i^{-1} \underline{\boldsymbol{f}}_i = \boldsymbol{0}, \tag{6.2}
$$

where

$$
(\underline{\boldsymbol{M}}_i)_{k,j} = \int\limits_{\mathcal{A}_i} \Phi_{i,k} \Phi_{i,j} \, dV \tag{6.3}
$$

and

$$
(\underline{\boldsymbol{f}}_i)_j = \sum_{e=1}^{E_i} \int\limits_{\mathcal{E}_{i,e}^{\mathcal{A}}} f(c^-, c^+, \boldsymbol{n}) \Phi_{i,j} \, dA + \int\limits_{\mathfrak{I}_i} f(c^-, c^+, \boldsymbol{n}_{\mathfrak{I}}) \Phi_{i,j} \, dA - \int\limits_{\mathcal{A}_i} \boldsymbol{f}(c_i) \cdot \nabla \Phi_{i,j} \, dV. \tag{6.4}
$$

The temporal discretization of these equations can still be accomplished by virtue of the RK methods defined by Equation (4.16) and Equation (4.17).

We emphasize that the changes in the implementation for the evaluation of the mass matrix $\underline{\boldsymbol{M}}_i$ and the modified discrete operator $\underline{\boldsymbol{f}}_i$ are almost trivial with respect to the original scheme. This is due to the fact that we can simply replace the standard numerical integration procedures by the HMF approach without any further changes to the existing code, except for the incorporation of the accessory integral over $\mathfrak{I}_i$ (Lieb 2013). Again, this term can easily be evaluated by making use of the existing implementation of a given numerical flux function and the surface quadrature rules following from the HMF approach.

Obviously, the presence of intersected cells $\mathcal{K}_i$ with extremely small volume fractions $\text{vol}(\mathcal{A}_i)$ inside of the physical problem domain causes significant problems in terms of the CFL constraint (cf. Equation (4.19)) as well as the conditioning of the mass matrix (cf. Equation (4.12)). Warburton & Hagstrom (2008) have shown how the first

issue can be alleviated using a special filtering strategy. Additionally, several authors have considered local time-stepping strategies as an interesting alternative to implicit time discretizations (Lörcher et al. (2007), Lörcher et al. (2008), Dumbser et al. (2008), Hindenlang et al. (2012), Winters & Kopriva (2013)). For the purposes of this outlook, it suffices to replace the original estimate for the stability limit (Equation (4.19)) by an estimate that accounts for the size of $\mathcal{A}_i$, for example

$$\Delta t \leq \frac{c_{\text{CFL}}}{2P+1} \frac{\sqrt[D]{\text{vol}(\mathcal{A}_i)}}{\|\boldsymbol{u}\| + a}. \tag{6.5}$$

The conditioning of the mass matrix, on the other hand, can be improved by an appropriate rescaling of the basis functions (Bastian & Engwer (2009), Heimann et al. (2013)) that can be complemented with a cell-merging strategy if necessary (Johansson & Larson 2012). In what follows, we will however limit ourselves to steady problems where the temporal term in Equation (6.2) is identically zero for the exact solution. This allows for the replacement of the true mass matrix by the identity matrix in the exemplary configuration studied in the following section.

## 6.2.2 Results for a steady isentropic vortex

We verify our implementation of an IBM using the example of a steady variant $(u', v') = (0, 0)$ of the isentropic vortex in an ideal gas ($\gamma = 1.4$) that has been simulated in Section 4.3.1 by virtue of a standard RKDGM. To that end, we introduce the level set function

$$\varphi(x, y) = x^2 + y^2 - 1.25^2 \tag{6.6}$$

such that the physical problem domain is restricted to a disk with radius $1.25$. The streamlines of the steady vortex solution are given by concentric circles, which is why we can enforce the slip wall boundary condition

$$\boldsymbol{u} \cdot \boldsymbol{n}_{\text{J}} = 0 \tag{6.7}$$

at $\varphi(x, y) = 0$ without altering the exact solution depicted in Section 3.1. This condition can conveniently be enforced by setting

$$\begin{pmatrix} \rho^+ \\ \boldsymbol{u}^+ \\ p^+ \end{pmatrix} = \begin{pmatrix} \rho^- \\ \boldsymbol{u}^- - 2(\boldsymbol{u}^- \cdot \boldsymbol{n}_{\text{J}})\boldsymbol{n}_{\text{J}} \\ p^- \end{pmatrix} \tag{6.8}$$

when evaluating the numerical flux at the interface (Feistauer et al. 2003).

In our numerical examples, the physical domain is embedded into the computational domain $[-2, 2] \times [-2, 2]$ that we discretize by means of a series of equidistant, Cartesian grids with $2 \times 2$, $4 \times 4$, $8 \times 8$, $16 \times 16$ and $32 \times 32$ cells, respectively. The resulting initial configurations for the different resolutions are visualized in Figure 6.1. We advance the numerical solution in time until $t = 0.1$ using a 4th order RK scheme, where the

size of the time-steps is computed from (6.5) with $c_{\mathrm{cfl}} = 0.05$ in order to rule out an influence of the time discretization error. Accordingly, the present test case mainly verifies whether our implementation is able to sustain a given exact solution of the Euler equations. Despite the fact that this renders the test case rather simple from a theoretical point of view, Bassi & Rebay (1997) have strikingly shown that even minor inaccuracies in the representation of curved boundaries can tremendously deteriorate the quality of numerical solutions obtained via higher order methods.

Figure 6.2 shows the convergence of the entropy error (4.20) under grid refinement. Here, we have used quadrature rules obtained by means a of hierarchical moment-fitting strategy with Ansatz order 9, viz. HMF(9) according to the nomenclature introduced in Chapter 5. Even though we have omitted the solutions on the coarsest grid in the evaluation of the EOC in order to avoid an overestimation, the observed rates even exceed the expected rate for a DGM.

We are now interested in the influence of the integration error on this result. Accordingly, we have repeated the $h$-convergence study for the 4th order DGM (i.e., the last graph in Figure 6.2) using quadrature rules based on HMF($P$) with $4 \leq P \leq 9$. The corresponding results for the entropy error are displayed in the left part of Figure 6.3. In case of HMF(4), we see that the global error hardly decreases in the range from $h = 0.5$ to $h = 0.125$, while the simulation on the finest grid even diverges. This problem vanishes for higher values of $P$, but we observe a strong influence of the numerical integration on the EOC, especially on the finest grids.

At the same time, the significance of the choice of $P$ for the computational effort decreases under grid refinement. This fact is illustrated by the right part of Figure 6.3, where we have noted the relative runtime $t_{\mathrm{rel}}$ in terms of the respective simulations using HMF(5) for the two finest resolutions. On the finest grid, for example, we can gain almost four orders of magnitude regarding the global entropy error, whereas the runtime only increases by five percent.

All in all, the presented results are extremely promising, even though one has to keep in mind that the provisional assumptions formulated in Section 6.2.1 are rather restrictive. Our further research efforts will thus be focussed on the elimination of these limitations and on a more extensive verification of the resulting scheme.

(a) $h = 1$ (12 non-empty cells)

(b) $h = 0.5$ (32 non-empty cells)

(c) $h = 0.25$ (104 non-empty cells)

(d) $h = 0.125$ (360 non-empty cells)

(e) $h = 0.0625$ (1376 non-empty cells)

(f) Pressure scale
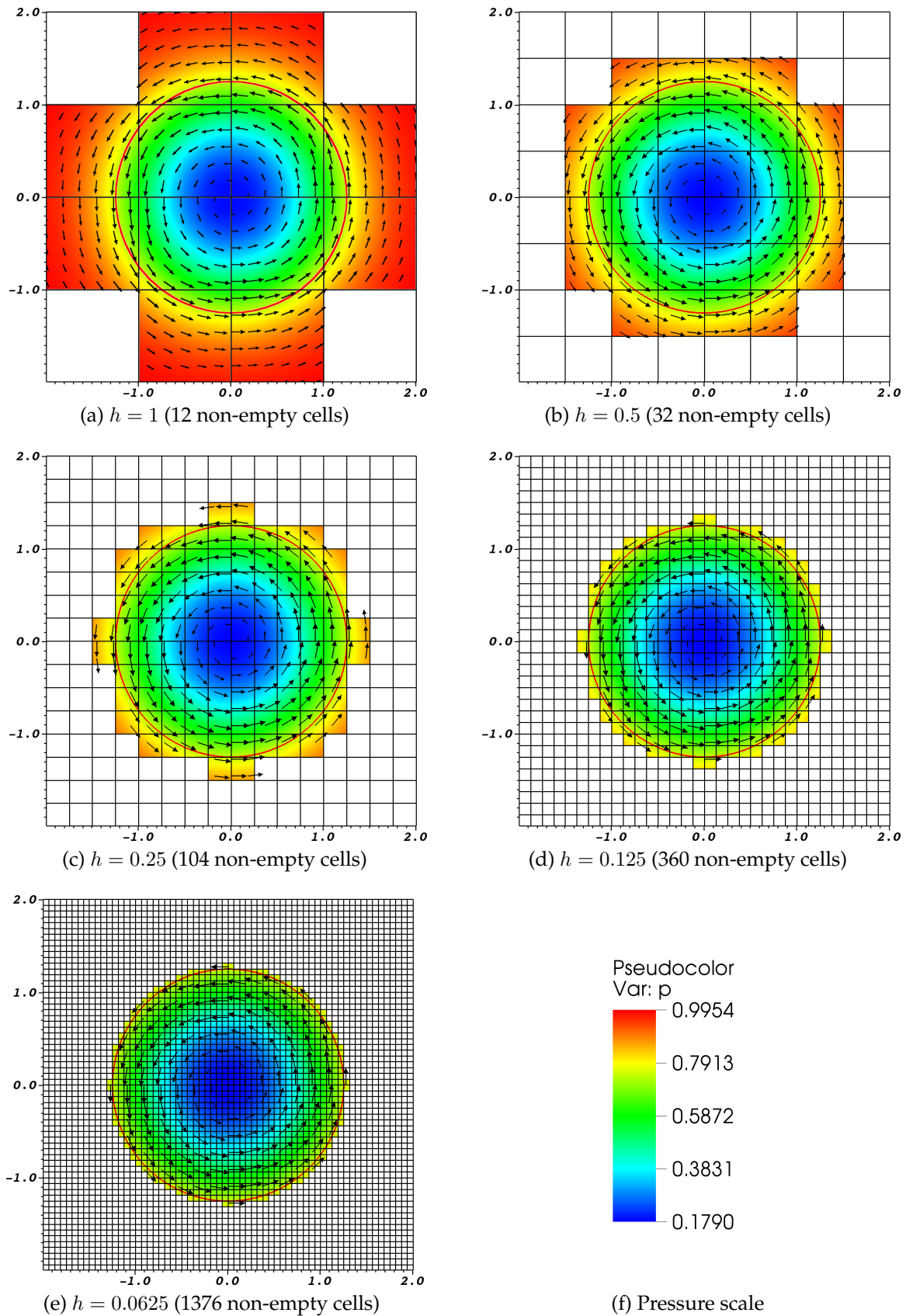
Figure 6.1: Initial pressure distribution and velocity vectors on the series of grids used in the $h$-convergence study for an isentropic vortex in an ideal gas ($\gamma = 1.4$). The boundary of the physical domain is given by the zero iso-contour of a level set function (red circle)
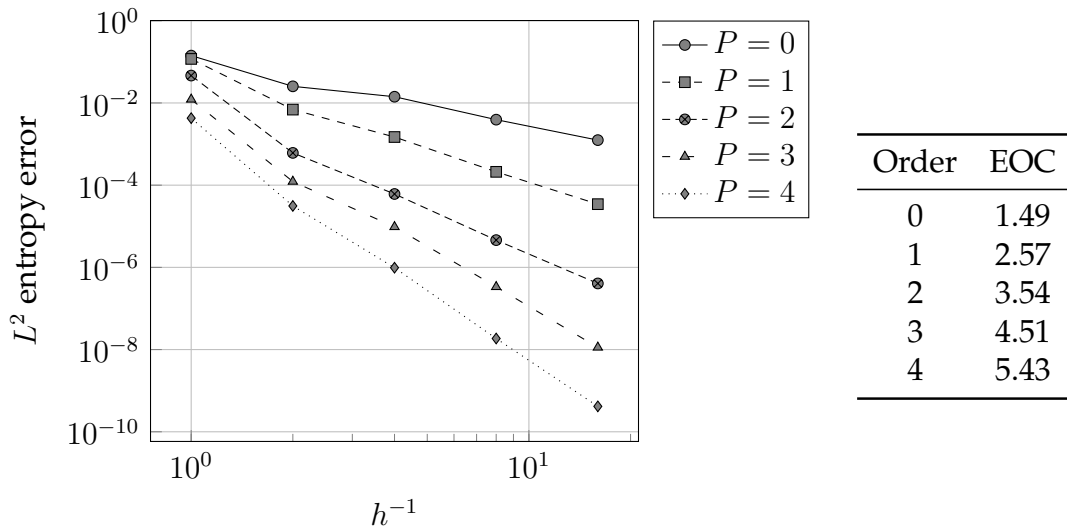
Figure 6.2: Results of the $h$-convergence study for a steady isentropic vortex in an ideal gas ($\gamma = 1.4$) using an IBM based on HMF(9)
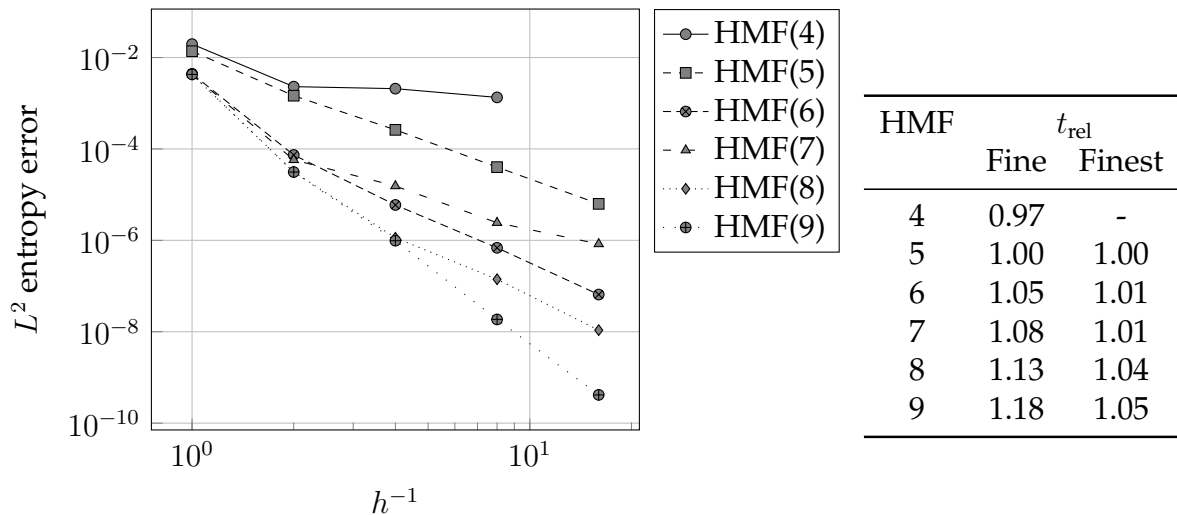


Figure 6.3: Left: Study of the influence of the order of the moment-fitting system on the $h$-convergence of a 4th order DGM for a steady isentropic vortex in an ideal gas ($\gamma = 1.4$). Right: Impact of the order of the moment-fitting system on the relative runtime with respect to HMF(5) on the two finest grids

# 7 Bibliography

ABEDIAN, A., PARVIZIAN, J., DÜSTER, A., KHADEMYZADEH, H., RANK, E. (2013): Performance of Different Integration Schemes in Facing Discontinuities in the Finite Cell Method. *International Journal of Computational Methods 10*, 03, 1350002.

ANDERSON, E., BAI, Z., BISCHOF, C., BLACKFORD, S., DEMMEL, J., DONGARRA, J., CROZ, J. D., GREENBAUM, A., HAMMARLING, S., MCKENNEY, A., SORENSEN, D. (1999): *LAPACK Users' Guide*. Society for Industrial and Applied Mathematics, Philadelphia, PA, Third edn..

ANDERSON, J. (2004): *Modern Compressible Flow: With Historical Perspective*. McGraw-Hill Education, Third edn..

ANDERSON, J. D. (2011): *Fundamentals of Aerodynamics*. Mcgraw-Hill Professional, Fifth edn..

ATKINS, H. L., SHU, C. (1996): Quadrature-Free implementation of the Discontinuous Galerkin Method for hyperbolic equations. *AIAA JOURNAL 36*, 775—782.

BABUŠKA, I., MELENK, J. M. (1997): The Partition of Unity Method. *International Journal for Numerical Methods in Engineering 40*, 4, 727–758.

BASSI, F., REBAY, S. (1997): High-order accurate discontinuous finite element solution of the 2D Euler equations. *Journal of Computational Physics 138*, 2, 251–285.

BASTIAN, P., ENGWER, C. (2009): An unfitted finite element method using discontinuous Galerkin. *International Journal for Numerical Methods in Engineering 79*, 12, 1557–1576.

BATTEN, P., CLARKE, N., LAMBERT, C., CAUSON, D. M. (1997): On the Choice of Wavespeeds for the HLLC Riemann Solver. *SIAM Journal on Scientific Computing 18*, 6, 1553–1570.

BELYTSCHKO, T., MOËS, N., USUI, S., PARIMI, C. (2001): Arbitrary discontinuities in finite elements. *International Journal for Numerical Methods in Engineering 50*, 4, 993–1013.

VAN DER BOS, F., GRAVEMEIER, V. (2009): Numerical simulation of premixed combustion using an enriched finite element method. *Journal of Computational Physics 228*, 10, 3605–3624.

BREMER, J., GIMBUTAS, Z., ROKHLIN, V. (2010): A Nonlinear Optimization Procedure for Generalized Gaussian Quadratures. *SIAM Journal on Scientific Computing 32*, 4, 1761.

BUTCHER, J. C. (1987): *The numerical analysis of ordinary differential equations: Runge-Kutta and general linear methods*. J. Wiley, Chichester ; New York.

CALLEN, H. B. (1985): *Thermodynamics and an Introduction to Thermostatistics*. Wiley, Second edn..

CHANG, C. (1952): General consideration of problems in compressible flow using the hodograph method. Technical Note NACA TN 2582, John Hopkins University, Washington.

CHEN, T., COOKE, C. H. (1994): On the Riemann problem for liquid or gas-liquid media. *International Journal for Numerical Methods in Fluids 18*, 5, 529–541.

CHENG, K. W., FRIES, T. (2010): Higher-order XFEM for curved strong and weak discontinuities. *International Journal for Numerical Methods in Engineering 82*, 5, 564–590.

CHESSA, J., BELYTSCHKO, T. (2003a): An enriched finite element method and level sets for axisymmetric two-phase flow with surface tension. *International Journal for Numerical Methods in Engineering 58*, 13, 2041–2064.

CHESSA, J., BELYTSCHKO, T. (2003b): An Extended Finite Element Method for Two-Phase Fluids. *Journal of Applied Mechanics 70*, 1, 10–17.

CHIOCCHIA, G. (1985): Exact solutions to transonic and supersonic flows. Technical Report AR-211, AGARD.

COCCHI, J., SAUREL, R. (1997): A Riemann Problem Based Method for the Resolution of Compressible Multimaterial Flows. *Journal of Computational Physics 137*, 2, 265–298.

COCKBURN, B. (2003): Discontinuous Galerkin methods. *ZAMM 83*, 11, 731–754.

COCKBURN, B., HOU, S., SHU, C. (1990): The Runge-Kutta Local Projection Discontinuous Galerkin Finite Element Method for Conservation Laws. IV: The Multidimensional Case. *Mathematics of Computation 54*, 190, 545–581.

COCKBURN, B., KARNIADAKIS, G. E., SHU, C. (2000a): The Development of Discontinuous Galerkin Methods. In: *Discontinuous Galerkin Methods: Theory, Computation and Applications*, B. Cockburn, G. E. Karniadakis, C. Shu, eds., Springer Berlin Heidelberg, no. 11 in Lecture Notes in Computational Science and Engineering, 3–50.

COCKBURN, B., KARNIADAKIS, G. E., SHU, C., eds. (2000b): *Discontinuous Galerkin Methods: Theory, Computation and Applications*. Springer, First edn..

COCKBURN, B., LIN, S., SHU, C. (1989): TVB Runge-Kutta local projection discontinuous Galerkin finite element method for conservation laws III: One-dimensional systems. *Journal of Computational Physics 84*, 1, 90–113.

COCKBURN, B., SHU, C. (1989): TVB Runge-Kutta Local Projection Discontinuous Galerkin Finite Element Method for Conservation Laws II: General Framework. *Mathematics of Computation 52*, 186, 411–435.

COCKBURN, B., SHU, C. (1991): The Runge-Kutta local projection P1-discontinuous Galerkin method for scalar conservation laws. In: *American Institute of Aeronautics and Astronautics*, vol. 25, 337–361.

COCKBURN, B., SHU, C. (1998a): The Local Discontinuous Galerkin Method for Time-Dependent Convection-Diffusion Systems. *SIAM Journal on Numerical Analysis 35*, 6, 2440–2463.

COCKBURN, B., SHU, C. (1998b): The Runge-Kutta Discontinuous Galerkin Method for Conservation Laws V: Multidimensional Systems. *Journal of Computational Physics 141*, 2, 199–224.

COCKBURN, B., SHU, C. (2001): Runge-Kutta Discontinuous Galerkin Methods for Convection-Dominated Problems. *Journal of Scientific Computing 16*, 3, 173–261.

COOLS, R. (2003): An encyclopaedia of cubature formulas. *Journal of Complexity 19*, 3, 445–453.

DAVOUDZADEH, F., MCDONALD, H., THOMPSON, B. (1995): Accuracy evaluation of unsteady CFD numerical schemes by vortex preservation. *Computers & Fluids 24*, 8, 883–895.

DI PIETRO, D. A., ERN, A. (2012): *Mathematical aspects of discontinuous galerkin methods*. Springer, Berlin; New York.

DOLEJŠÍ, V., FEISTAUER, M., SCHWAB, C. (2003): On some aspects of the discontinuous Galerkin finite element method for conservation laws. *Mathematics and Computers in Simulation 61*, 3-6, 333–346.

DRÉAU, K., CHEVAUGEON, N., MOËS, N. (2010): Studied X-FEM enrichment to handle material interfaces with higher order finite element. *Computer Methods in Applied Mechanics and Engineering 199*, 29–32, 1922–1936.

DUMBSER, M., BALSARA, D. S., TORO, E. F., MUNZ, C. (2008): A unified framework for the construction of one-step finite volume and discontinuous Galerkin schemes on unstructured meshes. *Journal of Computational Physics 227*, 18, 8209–8253.

DÜSTER, A., PARVIZIAN, J., YANG, Z., RANK, E. (2008): The finite cell method for three-dimensional problems of solid mechanics. *Computer Methods in Applied Mechanics and Engineering 197*, 45-48, 3768 – 3782.

EMANUEL, G. (2010): *Analytical Fluid Dynamics, Second Edition*. CRC Press.

ENGQUIST, B., TORNBERG, A., TSAI, R. (2004): Discretization of Dirac Delta Functions in Level Set Methods. *Journal of Computational Physics 207*, 28—51.

ENGWER, C. (2009): *An Unfitted Discontinuous Galerkin Scheme for Micro-scale Simulations and Numerical Upscaling*. Ph.D. thesis, Heidelberg.

FARHAT, C., RALLU, A., SHANKARAN, S. (2008): A higher-order generalized ghost fluid method for the poor for the three-dimensional two-phase flow computation of underwater implosions. *Journal of Computational Physics 227*, 16, 7674–7700.

FEDKIW, R. P., ASLAM, T., MERRIMAN, B., OSHER, S. (1999): A Non-oscillatory Eulerian Approach to Interfaces in Multimaterial Flows (the Ghost Fluid Method). *Journal of Computational Physics 152*, 2, 457–492.

FEISTAUER, M., FELCMAN, J., STRAŠKRABA, I. (2003): *Mathematical and computational methods for compressible flow*. Oxford University Press.

FERZIGER, J. H., PERIC, M. (2001): *Computational Methods for Fluid Dynamics*. Springer, Berlin, Third edn..

FLORES, J., HOLT, M. (1981): Glimm's method applied to underwater explosions. *Journal of Computational Physics 44*, 2, 377–387.

FRANC, J., MICHEL, J., eds. (2010): *Fundamentals of Cavitation*. Springer Netherlands, First edn..

FRIES, T. (2009): The intrinsic XFEM for two-fluid flows. *International Journal for Numerical Methods in Fluids 60*, 4, 437–471.

FRIES, T., BELYTSCHKO, T. (2010): The extended/generalized finite element method: An overview of the method and its applications. *International Journal for Numerical Methods in Engineering* , 253–304.

FRIES, T., ZILIAN, A. (2009): On time integration in the XFEM. *International Journal for Numerical Methods in Engineering 79*, 1, 69–93.

FRÖHLCKE, A., GJONAJ, E., WEILAND, T. (2012): A Boundary Conformal DG Approach for Electro-Quasistatics Problems. In: *Scientific Computing in Electrical Engineering SCEE 2010*, B. Michielsen, J. Poirier, eds., Springer Berlin Heidelberg, vol. 16 of *Mathematics in Industry*, 153–161.

GASSNER, G. J., LÖRCHER, F., MUNZ, C., HESTHAVEN, J. S. (2008): Polymorphic nodal elements and their application in discontinuous Galerkin methods. *Journal of Computational Physics 228*, 5, 1573–1590.

GEIRINGER, H. (1955): Grenzlinien der Hodographentransformation. *Mathematische Zeitschrift 63*, 1, 514–524.

GOTTLIEB, S., SHU, C. (1998): Total variation diminishing Runge-Kutta schemes. *Mathematics of Computation of the American Mathematical Society 67*, 221, 73–85.

GROSS, S., REUSKEN, A. (2011): *Numerical Methods for Two-phase Incompressible Flows*. Springer Berlin Heidelberg, First edn..

HALT, D. W., AGARWAL, R. K. (1992): Compact higher order characteristic-based Euler solver for unstructured grids. *AIAA Journal 30*, 8, 1993–1999.

HARTMANN, R. (2002): *Adaptive Finite Element Methods for the Compressible Euler Equations*. Ph.D. thesis, Ruprecht-Karls-Universität Heidelberg, Heidelberg.

HEIMANN, F., ENGWER, C., IPPISCH, O., BASTIAN, P. (2013): An unfitted interior penalty discontinuous Galerkin method for incompressible Navier-Stokes two-phase flow. *International Journal for Numerical Methods in Fluids 71*, 3, 269—293.

HESTHAVEN, J. S., WARBURTON, T. (2007): *Nodal Discontinuous Galerkin Methods: Algorithms, Analysis, and Applications*. Springer, Berlin, First edn..

HINDENLANG, F., GASSNER, G. J., ALTMANN, C., BECK, A., STAUDENMAIER, M., MUNZ, C. (2012): Explicit Discontinuous Galerkin methods for unsteady problems. *Computers & Fluids 61*, 86–93.

HU, C., SHU, C.-W. (1998): Weighted Essentially Non-Oscillatory Schemes on Triangular Meshes. *Journal of Computational Physics 150*, 97—127.

HU, F. Q. (2006): On the construction of PML absorbing boundary condition for the non-linear Euler equations. In: *AIAA paper*, Reno, vol. 798, 2006.

IVINGS, M. J., CAUSON, D. M., TORO, E. F. (1998): On Riemann solvers for compressible liquids. *International Journal for Numerical Methods in Fluids 28*, 3, 395–418.

JOHANSSON, A., LARSON, M. G. (2012): A high order discontinuous Galerkin Nitsche method for elliptic problems with fictitious boundary. *Numerische Mathematik 123*, 4, 607–628.

JOHNSON, C., PITKÄRANTA, J. (1986): An analysis of the discontinuous Galerkin method for a scalar hyperbolic equation. *Mathematics of Computation 46*, 1–26.

JOHNSTON, I. A. (2005): The Noble-Abel Equation of State: Thermodynamic Derivations for Ballistics Modelling. Technical Report DSTO-TN?0-670, Defence Science and Technology Organisation, Edinburgh, Australia.

KARLIN, S., STUDDEN, W. J. (1966): *Tchebycheff systems: with applications in analysis and statistics*. Interscience Publishers.

KLEIN, B., KUMMER, F., OBERLACK, M. (2013): A SIMPLE based discontinuous Galerkin solver for steady incompressible flows. *Journal of Computational Physics 237*, 0, 235–250.

KUMMER, F. (2011): *The Extended DG discretization of discontinuous PDE's and the BoSSS software framework*. Ph.D. thesis, TU Darmstadt, Darmstadt.

KUMMER, F., EMAMY, N., MOUSAVI BELFEH TEYMOURI, R., OBERLACK, M. (2009): Report on the development of a generic discontinuous Galerkin framework in .NET. In: *ParCFD 2009, 21st Int. Conf. on Parallel Computational Fluid Dynamics, 18-22 May, 2009, Moffett Field, California,USA*, Moffett Field, California,USA.

KUMMER, F., OBERLACK, M. (2013): An Extension of the Discontinuous Galerkin Method for the Singular Poisson Equation. *SIAM Journal on Scientific Computing 35*, 2, 603–622.

LAMB, H. (1916): *Hydrodynamics*. Dover Books on Physics, Cambridge University Press, Cambridge, UK; New York, Fourth edn..

LEGAY, A., WANG, H. W., BELYTSCHKO, T. (2005): Strong and weak arbitrary discontinuities in spectral finite elements. *International Journal for Numerical Methods in Engineering 64*, 8, 991–1008.

LEGRAIN, G., CHEVAUGEON, N., DRÉAU, K. (2012): High order X-FEM and levelsets for complex microstructures: Uncoupling geometry and approximation. *Computer Methods in Applied Mechanics and Engineering 241–244*, 0, 172–189.

LEHRENFELD, C., REUSKEN, A. (2013): Analysis of a Nitsche XFEM-DG Discretization for a Class of Two-Phase Mass Transport Problems. *SIAM Journal on Numerical Analysis 51*, 2, 958–983.

LESAINT, P., RAVIART, P. (1974): On a finite element method for solving the neutron transport equation. In: *Mathematical aspects of finite elements in partial differential equations (Proc. Sympos., Math. Res. Center, Univ. Wisconsin, Madison, Wis., 1974)*, Math. Res. Center, Univ. of Wisconsin-Madison, Academic Press, New York, 89—123.

LEVEQUE, R. J. (2010): *Numerical Methods for Conservation Laws*. Birkhäuser Verlag, Second edn..

LI, B. Q. (2006): *Discontinuous finite elements in fluid dynamics and heat transfer*. Birkhäuser.

LIEB, A. (2013): *Implementation and Validation of a Level Set based Immersed Boundary Method for an inviscid flow Solver built on the Discontinuous Galerkin Method*. Bachelor thesis, TU Darmstadt, Darmstadt.

LÖRCHER, F., GASSNER, G., MUNZ, C. (2007): A Discontinuous Galerkin Scheme Based on a Space-Time Expansion. I. Inviscid Compressible Flow in One Space Dimension. *Journal of Scientific Computing 32*, 2, 175–199.

LÖRCHER, F., GASSNER, G., MUNZ, C. (2008): An explicit discontinuous Galerkin scheme with local time-stepping for general unsteady diffusion equations. *Journal of Computational Physics 227*, 11, 5649–5670.

MELENK, J. M., BABUŠKA, I. (1996): The partition of unity finite element method: Basic theory and applications. *Computer Methods in Applied Mechanics and Engineering 139*, 1-4, 289–314.

MENIKOFF, R., PLOHR, B. (1989): The Riemann problem for fluid flow of real materials. *Reviews of Modern Physics 61*, 1, 75–130.

MIN, C., GIBOU, F. (2007): Geometric integration over irregular domains with application to level-set methods. *Journal of Computational Physics 226*, 2, 1432–1443.

MIN, C., GIBOU, F. (2008): Robust second-order accurate discretizations of the multi-dimensional Heaviside and Dirac delta functions. *Journal of Computational Physics 227*, 22, 9686–9695.

MITTAL, R., IACCARINO, G. (2005): Immersed Boundary Methods. *Annual Review of Fluid Mechanics 37*, 239–261.

MOËS, N., BÉCHET, E., TOURBIER, M. (2006): Imposing Dirichlet boundary conditions in the extended finite element method. *International Journal for Numerical Methods in Engineering 67*, 12, 1641–1669.

MOËS, N., DOLBOW, J., BELYTSCHKO, T. (1999): A finite element method for crack growth without remeshing. *International Journal for Numerical Methods in Engineering 46*, 1, 131–150.

MOUSAVI, S. E., SUKUMAR, N. (2010): Generalized Gaussian quadrature rules for discontinuities and crack singularities in the extended finite element method. *Computer Methods in Applied Mechanics and Engineering 199*, 49–52, 3237–3249.

MOUSAVI, S. E., SUKUMAR, N. (2011): Numerical integration of polynomials and discontinuous functions on irregular convex polygons and polyhedrons. *Computational Mechanics 47*, 5, 535–554.

MOUSAVI, S. E., XIAO, H., SUKUMAR, N. (2010): Generalized Gaussian quadrature rules on arbitrary polygons. *International Journal for Numerical Methods in Engineering 82*, 1, 99–113.

MÜLLER, B. (2011): *Implementation of an inviscid flow solver based on the Discontinuous Galerkin library BoSSS*. Master thesis, TU Darmstadt, Darmstadt.

MÜLLER, B., KUMMER, F., OBERLACK, M. (2013): Highly accurate surface and volume integration on implicit domains by means of moment-fitting. *International Journal for Numerical Methods in Engineering 96*, 512–528.

MÜLLER, B., KUMMER, F., OBERLACK, M., WANG, Y. (2012): Simple multidimensional integration of discontinuous functions with application to level set methods. *International Journal for Numerical Methods in Engineering 92*, 7, 637–651.

OLVER, F. W. J., LOZIER, D. W., BOISVERT, R. F., CLARK, C. W., eds. (2010): *NIST handbook of mathematical functions*. Cambridge University Press, New York.

OSHER, S. J., FEDKIW, R. P. (2002): *Level Set Methods and Dynamic Implicit Surfaces*. Springer, Berlin, First edn..

PERSSON, P., PERAIRE, J. (2006): Sub-Cell Shock Capturing for Discontinuous Galerkin Methods. In: *Proceedings of the 44th AIAA Aerospace Sciences Meeting and Exhibit*, vol. AIAA-2006-112.

PETERSON, T. (1991): A note on the convergence of the discontinuous Galerkin method for a scalar hyperbolic equation. *SIAM Journal on Numerical Analysis 28*, 133–140.

POLING, B. E., PRAUSNITZ, J. M., O'CONNELL, J. P. (2001): *The properties of gases and liquids*. McGraw-Hill, New York, Fifth edn..

PRANDTL, L. (2008): *Führer durch die Strömungslehre Grundlagen und Phänomene*. Vieweg Teubner, Wiesbaden, 12th edn..

PRESS, W. H. (2007): *Numerical recipes: the art of scientific computing*. Cambridge University Press, Cambridge, UK; New York, Third edn..

QIU, J., KHOO, B. C., SHU, C. (2006): A numerical study for the performance of the Runge-Kutta discontinuous Galerkin method based on different numerical fluxes. *Journal of Computational Physics 212*, 2, 540–565.

QIU, J., LIU, T., KHOO, B. C. (2007): Runge-Kutta discontinuous Galerkin methods for compressible two-medium flow simulations: One-dimensional case. *Journal of Computational Physics 222*, 1, 353–373.

RASTHOFER, U., HENKE, F., WALL, W., GRAVEMEIER, V. (2011): An extended residual-based variational multiscale method for two-phase flow including surface tension. *Computer Methods in Applied Mechanics and Engineering 200*, 21–22, 1866–1876.

REED, W. H., HILL, T. R. (1973): Triangular mesh methods for the neutron transport equation. Technical Report LA-UR-73–479, Los Alamos Scientific Laboratory, Los Alamos.

RINGLEB, F. (1940): Exakte Lösungen der Differentialgleichungen einer adiabatischen Gasströmung. *ZAMM - Journal of Applied Mathematics and Mechanics / Zeitschrift für Angewandte Mathematik und Mechanik 20*, 4, 185–198.

SAUERLAND, H., FRIES, T. (2011): The extended finite element method for two-phase and free-surface flows: A systematic study. *Journal of Computational Physics 230*, 9, 3369–3390.

SAUREL, R., ABGRALL, R. (1999): A Multiphase Godunov Method for Compressible Multifluid and Multiphase Flows. *Journal of Computational Physics 150*, 2, 425–467.

SMEREKA, P. (2006): The numerical approximation of a delta function with application to level set methods. *Journal of Computational Physics 211*, 77–90.

STAZI, F. L., BUDYN, E., CHESSA, J., BELYTSCHKO, T. (2003): An extended finite element method with higher-order elements for curved cracks. *Computational Mechanics 31*, 1-2, 38–48.

STRAIN, J. (1999): Tree methods for moving interfaces. *Journal of Computational Physics 151*, 2, 616–648.

STROUD, A. (1966): *Gaussian quadrature formulas*. Prentice Hall, Upper Saddle River.

STROUD, A. (1972): *Approximate Calculation of Multiple Integrals*. Prentice Hall, Upper Saddle River.

SUDHAKAR, Y., WALL, W. A. (2013): Quadrature schemes for arbitrary convex/concave volumes and integration of weak form in Enriched Partition of Unity Methods. *Computer Methods in Applied Mechanics and Engineering 258*, 39–54.

TORNBERG, A. (2002): Multi-Dimensional Quadrature of Singular and Discontinuous Functions. *BIT Numerical Mathematics 42*, 3, 644–669.

TORNBERG, A., ENGQUIST, B. (2003): Regularization Techniques for Numerical Approximation of PDEs with Singularities. *Journal of Scientific Computing 19*, 527–552.

TORNBERG, A., ENGQUIST, B. (2004): Numerical approximations of singular source terms in differential equations. *Journal of Computational Physics 200*, 2, 462–488.

TORO, E. F. (2009): *Riemann solvers and numerical methods for fluid dynamics*. Springer, Berlin/Heidelberg, Third edn..

TORO, E. F., SPRUCE, M., SPEARES, W. (1994): Restoration of the contact surface in the HLL-Riemann solver. *Shock Waves 4*, 1, 25–34.

TOWERS, J. D. (2007): Two methods for discretizing a delta function supported on a level set. *Journal of Computational Physics 220*, 2, 915–931.

VAN DER VEGT, J. J. W., VAN DER VEN, H. (1998): Discontinuous Galerkin Finite Element Method with Anisotropic Local Grid Refinement for Inviscid Compressible Flows. *Journal of Computational Physics 141*, 1, 46–77.

VAN DER VEGT, J. J. W., VAN DER VEN, H. (2002): Space-time discontinuous Galerkin finite element method with dynamic grid motion for inviscid compressible flows: I. general formulation. *Journal of Computational Physics 182*, 2, 546–585.

WANG, C. W., LIU, T. G., KHOO, B. C. (2006): A Real Ghost Fluid Method for the Simulation of Multimedium Compressible Flow. *SIAM Journal on Scientific Computing 28*, 1, 278.

WANG, Y., OBERLACK, M. (2011): A thermodynamic model of multiphase flows with moving interfaces and contact line. *Continuum Mechanics and Thermodynamics 23*, 5, 409–433.

WANG, Z., FIDKOWSKI, K., ABGRALL, R., BASSI, F., CARAENI, D., CARY, A., DECONINCK, H., HARTMANN, R., HILLEWAERT, K., HUYNH, H., KROLL, N., MAY, G., PERSSON, P., VAN LEER, B., VISBAL, M. (2013): High-order CFD methods: current status and perspective. *International Journal for Numerical Methods in Fluids* , 811–845.

WARBURTON, T., HAGSTROM, T. (2008): Taming the CFL number for Discontinuous Galerkin Methods on structured meshes. *SIAM Journal on Numerical Analysis 46*, 6, 3151–2180.

WEN, X. (2007): High order numerical methods to a type of delta function integrals. *Journal of Computational Physics 226*, 2, 1952–1967.

WEN, X. (2008): High Order Numerical Quadratures to One Dimensional Delta Function Integrals. *SIAM Journal on Scientific Computing 30*, 1825–1846.

WEN, X. (2009): High order numerical methods to two dimensional delta function integrals in level set methods. *Journal of Computational Physics 228*, 11, 4273–4290.

WEN, X. (2010): High Order Numerical Methods to Three Dimensional Delta Function Integrals in Level Set Methods. *SIAM Journal on Scientific Computing 32*, 1288–1309.

WESSELING, P. (2000): *Principles of Computational Fluid Dynamics*. Springer, First edn..

WINTERS, A. R., KOPRIVA, D. A. (2013): High-Order Local Time Stepping on Moving DG Spectral Element Meshes. *Journal of Scientific Computing* .

XIAO, H., GIMBUTAS, Z. (2010): A numerical algorithm for the construction of efficient quadrature rules in two and higher dimensions. *Computers & Mathematics with Applications 59*, 2, 663–676.

ZAHEDI, S., TORNBERG, A. (2010): Delta function approximations in level set methods by distance function extension. *Journal of Computational Physics 229*, 6, 2199–2219.

# A Reference polytopes and their sub-divisions

Below, we present the definitions of the zero-centred, equilateral reference polytopes depicted in Figure 5.2 and the corresponding elementary, affine linear transformations $\boldsymbol{E}_s(\boldsymbol{x}) = \boldsymbol{M}_s\boldsymbol{x} + \boldsymbol{b}_s$ ($s = 1, \ldots, S$) that map the vertices of the reference polytopes onto the vertices of the selected sub-polytopes (see Section 5.4.1). In particular, $\boldsymbol{M}_s \in \mathbb{R}^{D,D}$ and $\boldsymbol{b}_s \in \mathbb{R}^D$ are the transformation matrices and affine offsets, respectively. The orientation of the sub-polytopes is irrelevant for the purposes of the numerical integration, which is why we have arbitrarily chosen a convenient formulation.

## A.1 Line

The reference line consists of two vertices:

$$\boldsymbol{v}_1 = -1, \; \boldsymbol{v}_2 = 1. \tag{A.1}$$

The transformations are defined by the matrices

$$\boldsymbol{M}_1 = \boldsymbol{M}_2 = \frac{1}{2}\boldsymbol{I}_1, \tag{A.2}$$

where here and in the following, $\boldsymbol{I}_D$ denotes the $D$-dimensional identity matrix. The corresponding affine offsets are given by

$$\boldsymbol{b}_1 = \frac{1}{2}\boldsymbol{v}_1, \; \boldsymbol{b}_2 = \frac{1}{2}\boldsymbol{v}_2. \tag{A.3}$$

## A.2 Triangle

The reference triangle consists of three vertices:

$$\boldsymbol{v}_1 = \frac{1}{3}\begin{pmatrix} 0 \\ 4 \end{pmatrix}, \; \boldsymbol{v}_2 = \frac{1}{3}\begin{pmatrix} -2\sqrt{3} \\ -2 \end{pmatrix}, \; \boldsymbol{v}_3 = \frac{1}{3}\begin{pmatrix} 2\sqrt{3} \\ -2 \end{pmatrix}. \tag{A.4}$$

The transformations are defined by the matrices

$$\boldsymbol{M}_1 = \boldsymbol{M}_2 = \boldsymbol{M}_3 = \frac{1}{2}\boldsymbol{I}_2, \; \boldsymbol{M}_4 = \frac{1}{4}\begin{pmatrix} 1 & -\sqrt{3} \\ \sqrt{3} & 1 \end{pmatrix} \tag{A.5}$$

and the corresponding affine offsets

$$b_1 = \frac{1}{3}\begin{pmatrix} 0 \\ 2 \end{pmatrix}, \; b_2 = \frac{1}{3}\begin{pmatrix} -\sqrt{3} \\ -1 \end{pmatrix}, \; b_3 = \frac{1}{3}\begin{pmatrix} \sqrt{3} \\ -1 \end{pmatrix}, \; b_4 = \begin{pmatrix} 0 \\ 0 \end{pmatrix}. \tag{A.6}$$

## A.3  Square

The reference square consists of four vertices:

$$v_1 = \begin{pmatrix} -1 \\ -1 \end{pmatrix}, \; v_2 = \begin{pmatrix} 1 \\ -1 \end{pmatrix}, \; v_3 = \begin{pmatrix} 1 \\ 1 \end{pmatrix}, \; v_4 = \begin{pmatrix} -1 \\ 1 \end{pmatrix}. \tag{A.7}$$

The transformations are defined by the matrices

$$M_1 = \ldots = M_4 = \frac{1}{2}I_2 \tag{A.8}$$

and the corresponding affine offsets

$$b_1 = \frac{1}{2}v_1, \; \ldots, \; b_4 = \frac{1}{2}v_4. \tag{A.9}$$

## A.4  Cube

The reference cube consists of eight vertices:

$$v_1 = \begin{pmatrix} -1 \\ -1 \\ -1 \end{pmatrix}, \; v_2 = \begin{pmatrix} 1 \\ -1 \\ -1 \end{pmatrix}, \; v_3 = \begin{pmatrix} 1 \\ 1 \\ -1 \end{pmatrix}, \; v_4 = \begin{pmatrix} -1 \\ 1 \\ -1 \end{pmatrix}, \; v_5 = \begin{pmatrix} -1 \\ -1 \\ 1 \end{pmatrix},$$
$$v_6 = \begin{pmatrix} 1 \\ -1 \\ 1 \end{pmatrix}, \; v_7 = \begin{pmatrix} 1 \\ 1 \\ 1 \end{pmatrix}, \; v_8 = \begin{pmatrix} -1 \\ 1 \\ 1 \end{pmatrix}. \tag{A.10}$$

The transformations are defined by the matrices

$$M_1 = \ldots = M_8 = \frac{1}{2}I_3 \tag{A.11}$$

and the corresponding affine offsets

$$b_1 = \frac{1}{2}v_1, \; \ldots, \; b_8 = \frac{1}{2}v_8. \tag{A.12}$$

# B A note on alternative choices of the domain of integration

In Chapter 5, it has been mentioned that the choice of $\mathcal{A}$ as domain of integration was voluntary. More sensible choices exist for several applications which shall be sketched briefly in the following.

First of all, Equation (5.22), Equation (5.35) and Equation (5.44) can be formulated analogously for the sub-volume $\mathcal{B}$. This leads to

$$\int_{\mathcal{I}} \boldsymbol{g} \cdot \boldsymbol{n}_{\mathcal{I}} \, dA = - \int_{\mathcal{B}} \nabla \cdot \boldsymbol{g} \, dV + \int_{\partial\mathcal{B}\backslash\mathcal{I}} \boldsymbol{g} \cdot \boldsymbol{n} \, dA, \tag{B.1}$$

$$\int_{\mathcal{I}} \boldsymbol{f}_k \cdot \boldsymbol{n}_{\mathcal{I}} \, dA = \int_{\partial\mathcal{B}\backslash\mathcal{I}} \boldsymbol{f}_k \cdot \boldsymbol{n} \, dA \tag{B.2}$$

and

$$\int_{\mathcal{B}} f_i \, dV = \int_{\partial\mathcal{B}\backslash\mathcal{I}} \boldsymbol{f}_i \cdot \boldsymbol{n} \, dA - \int_{\mathcal{I}} \boldsymbol{f}_i \cdot \boldsymbol{n}_{\mathcal{I}} \, dA, \tag{B.3}$$

respectively, where the sign changes account for $\boldsymbol{n} = -\boldsymbol{n}_{\mathcal{I}}$ on $\mathcal{I}$ when integrating over $\partial\mathcal{B}$. In certain cases, using these equations instead of the original formulations may prove to be advantageous. This is the case, for example, if $\mathcal{A}$ is very small compared to $\mathcal{B}$. As a result, we always use the larger sub-volume of $\mathcal{K}$ in the context of the adaptive strategy presented in Section 5.4.

Furthermore, both sub-domains may be combined directly in case of the moment-fitting quadrature (Section 5.5). Consider a generic integrand $g : \mathcal{K} \to \mathbb{R}$ of the form

$$g = \begin{cases} g_{\mathcal{A}} & \text{in } \mathcal{A} \\ g_{\mathcal{B}} & \text{in } \mathcal{B} \end{cases} \tag{B.4}$$

with smooth functions $g_{\mathcal{A}} : \mathcal{K} \to \mathbb{R}$ and $g_{\mathcal{B}} : \mathcal{K} \to \mathbb{R}$. Making use of the sign function, $g$ can be rewritten as

$$g = \frac{g_{\mathcal{A}} + g_{\mathcal{B}}}{2} - \frac{\text{sgn}(\varphi)}{2} [\![g]\!]. \tag{B.5}$$

The first term on the right-hand side is smooth and can be integrated with traditional quadrature rules. For the integration of the second term, we can combine Equation (5.44) and Equation (B.3) in order to obtain an expression for the full volume,

$$\int_{\mathcal{K}} \mathrm{sgn}(\varphi) f_i \, dV = -\int_{\mathcal{A}} f_i \, dV + \int_{\mathcal{B}} f_i \, dV \tag{B.6}$$

$$= -\int_{\partial\mathcal{A}} \boldsymbol{f}_i \cdot \boldsymbol{n} \, dA + \int_{\partial\mathcal{B}} \boldsymbol{f}_i \cdot \boldsymbol{n} \, dA \tag{B.7}$$

$$= \int_{\partial\mathcal{K}} (2H(\varphi) - 1) \boldsymbol{f}_i \cdot \boldsymbol{n} \, dA - 2 \int_{\mathcal{J}} \boldsymbol{f}_i \cdot \boldsymbol{n}_\mathcal{J} \, dA, \tag{B.8}$$

that can be used to replace the right-hand side of (5.45). Typically, the resulting strategy will be significantly more efficient than integrating over the sub-domains separately because fewer linear systems have to be solved.

# C Construction of a divergence-free basis

Subsequently, we will describe how a divergence-free set of vector-valued basis functions $\mathcal{F}'$ that is associated with a given polynomial basis $\mathcal{F} = \{f_i\}_{i=1,\ldots,N}$ can be constructed. In a first step, we define the auxiliary set $\mathcal{G}$ with $|\mathcal{G}| = D \cdot N$ as

$$\mathcal{G} = \{f_i \boldsymbol{e}_d\}_{\substack{i=1,\ldots,N \\ d=1,\ldots,D}} = \{\boldsymbol{g}_n\}_{n=1,\ldots,D\cdot N}, \tag{C.1}$$

where $\boldsymbol{e}_d$ denotes the $d$-th coordinate vector. The divergence of the functions $\boldsymbol{g}_n$ will be non-zero in general, but we can seek divergence-free linear combinations of these functions in a second step.

To that end, let $\boldsymbol{c}_n \in \mathbb{R}^N$ denote the vector of coefficients of the polynomial $\nabla \cdot \boldsymbol{g}_n$, i.e.

$$\nabla \cdot \boldsymbol{g}_n = \sum_{i=1}^{N} (\boldsymbol{c}_n)_i \, f_i, \tag{C.2}$$

and let $\boldsymbol{H} = (\boldsymbol{c}_1, \ldots, \boldsymbol{c}_{D\cdot N}) \in \mathbb{R}^{N,D\cdot N}$. Obviously, every fixed vector $\boldsymbol{a} = (a_1, \ldots, a_{D\cdot N})^T$ that satisfies $\boldsymbol{H}\boldsymbol{a} = \boldsymbol{0}$ corresponds to a divergence-free function $\boldsymbol{f} = \sum_n a_n \boldsymbol{g}_n$ because

$$\nabla \cdot \sum_{n=1}^{D\cdot N} a_n \boldsymbol{g}_n = \sum_{n=1}^{D\cdot N} a_n (\nabla \cdot \boldsymbol{g}_n) \tag{C.3}$$

$$= \sum_{n=1}^{D\cdot N} a_n \sum_{i=1}^{N} (\boldsymbol{c}_n)_i \, f_i \tag{C.4}$$

$$= \sum_{i=1}^{N} f_i \sum_{n=1}^{D\cdot N} (\boldsymbol{c}_n)_i a_n \tag{C.5}$$

$$= \sum_{i=1}^{N} f_i \sum_{n=1}^{D\cdot N} (\boldsymbol{H})_{i,n} a_n \tag{C.6}$$

$$= 0 \tag{C.7}$$

holds. We can thus determine a basis of the *null space*

$$\text{null}(\boldsymbol{H}) = \{\boldsymbol{a} \in \mathbb{R}^{D\cdot N} : \boldsymbol{H}\boldsymbol{a} = \boldsymbol{0}\} \in \mathbb{R}^{K,D\cdot N} \tag{C.8}$$

of $\boldsymbol{H}$ (e.g., via Gaussian elimination) in order to obtain the divergence-free basis

$$\mathcal{F}' = \left\{ \sum_{n=1}^{D \cdot N} (\text{null}(\boldsymbol{H}))_{k,n} \, \boldsymbol{g}_n \right\}_{k=1,\ldots,K} . \tag{C.9}$$

Using the example of a simple monomial basis $\mathcal{F}$ of order two, the outlined algorithm generates

**Order 0:** $\boldsymbol{f}_1 = \begin{pmatrix} 1 \\ 0 \end{pmatrix}$, $\boldsymbol{f}_2 = \begin{pmatrix} 0 \\ 1 \end{pmatrix}$;

**Order 1:** $\boldsymbol{f}_3 = \begin{pmatrix} 0 \\ x \end{pmatrix}$, $\boldsymbol{f}_4 = \begin{pmatrix} x \\ -y \end{pmatrix}$, $\boldsymbol{f}_5 = \begin{pmatrix} y \\ 0 \end{pmatrix}$;

**Order 2:** $\boldsymbol{f}_6 = \begin{pmatrix} y^2 \\ 0 \end{pmatrix}$, $\boldsymbol{f}_7 = \begin{pmatrix} 2xy \\ -y^2 \end{pmatrix}$, $\boldsymbol{f}_8 = \begin{pmatrix} x^2 \\ -2xy \end{pmatrix}$, $\boldsymbol{f}_9 = \begin{pmatrix} 0 \\ x^2 \end{pmatrix}$

in the two-dimensional case and

**Order 0:** $\boldsymbol{f}_1 = \begin{pmatrix} 1 \\ 0 \\ 0 \end{pmatrix}$, $\boldsymbol{f}_2 = \begin{pmatrix} 0 \\ 1 \\ 0 \end{pmatrix}$, $\boldsymbol{f}_3 = \begin{pmatrix} 0 \\ 0 \\ 1 \end{pmatrix}$;

**Order 1:** $\boldsymbol{f}_4 = \begin{pmatrix} z \\ 0 \\ 0 \end{pmatrix}$, $\boldsymbol{f}_5 = \begin{pmatrix} 0 \\ z \\ 0 \end{pmatrix}$, $\boldsymbol{f}_6 = \begin{pmatrix} y \\ 0 \\ 0 \end{pmatrix}$, $\boldsymbol{f}_7 = \begin{pmatrix} 0 \\ y \\ -z \end{pmatrix}$, $\boldsymbol{f}_8 = \begin{pmatrix} 0 \\ 0 \\ y \end{pmatrix}$, $\boldsymbol{f}_9 = \begin{pmatrix} x \\ 0 \\ -z \end{pmatrix}$,

$\boldsymbol{f}_{10} = \begin{pmatrix} 0 \\ x \\ 0 \end{pmatrix}$, $\boldsymbol{f}_{11} = \begin{pmatrix} 0 \\ 0 \\ x \end{pmatrix}$;

**Order 2:** $\boldsymbol{f}_{12} = \begin{pmatrix} z^2 \\ 0 \\ 0 \end{pmatrix}$, $\boldsymbol{f}_{13} = \begin{pmatrix} 0 \\ z^2 \\ 0 \end{pmatrix}$, $\boldsymbol{f}_{14} = \begin{pmatrix} yz \\ 0 \\ 0 \end{pmatrix}$, $\boldsymbol{f}_{15} = \begin{pmatrix} 0 \\ 2yz \\ -z^2 \end{pmatrix}$, $\boldsymbol{f}_{16} = \begin{pmatrix} y^2 \\ 0 \\ 0 \end{pmatrix}$,

$\boldsymbol{f}_{17} = \begin{pmatrix} 0 \\ y^2 \\ -2yz \end{pmatrix}$, $\boldsymbol{f}_{18} = \begin{pmatrix} 0 \\ 0 \\ y^2 \end{pmatrix}$, $\boldsymbol{f}_{19} = \begin{pmatrix} 2xz \\ 0 \\ -z^2 \end{pmatrix}$, $\boldsymbol{f}_{20} = \begin{pmatrix} 0 \\ xz \\ 0 \end{pmatrix}$, $\boldsymbol{f}_{21} = \begin{pmatrix} xy \\ 0 \\ -yz \end{pmatrix}$,

$\boldsymbol{f}_{22} = \begin{pmatrix} 0 \\ xy \\ -xz \end{pmatrix}$, $\boldsymbol{f}_{23} = \begin{pmatrix} 0 \\ 0 \\ xy \end{pmatrix}$, $\boldsymbol{f}_{24} = \begin{pmatrix} x^2 \\ 0 \\ -2xz \end{pmatrix}$, $\boldsymbol{f}_{25} = \begin{pmatrix} 0 \\ x^2 \\ 0 \end{pmatrix}$, $\boldsymbol{f}_{26} = \begin{pmatrix} 0 \\ 0 \\ x^2 \end{pmatrix}$,

in the three-dimensional case.

It is important to note that the properties of $\mathcal{F}'$ are strongly related to the properties of the linear system (5.36). In particular, we discourage the application of the above-mentioned monomial basis in practice since it deteriorates the conditioning of the linear system to an extent that renders its numerical solution worthless in certain corner cases. As a consequence, we have applied the modified Gram-Schmidt procedure to the original monomial basis in order to avoid this problem.

# Curriculum vitae

Der Lebenslauf ist aus Datenschutzgründen in der Online-Version nicht enthalten.